DEVELOPMENT AND CHARACTERIZATION OF CATALYST MATERIALS OF ZINC-AIR BATTERIES

A THESIS SUBMITTED TO
THE GRADUATE SCHOOL OF NATURAL AND APPLIED SCIENCES
OF
MIDDLE EAST TECHNICAL UNIVERSITY

BY

BURCU ARSLAN HAMAT

IN PARTIAL FULFILLMENT OF THE REQUIREMENTS
FOR
THE DEGREE OF DOCTOR OF PHILOSOPHY
IN
METALLURGICAL AND MATERIALS ENGINEERING

FEBRUARY 2021

Approval of the thesis:

DEVELOPMENT AND CHARACTERIZATION OF CATALYST MATERIALS OF ZINC-AIR BATTERIES

submitted by **BURCU ARSLAN HAMAT** in partial fulfillment of the requirements for the degree of **Doctor of Philosophy** in **Metallurgical and Materials Engineering, Middle East Technical University** by,

Prof. Dr. Halil Kalıpçılar
Dean, Graduate School of **Natural and Applied Sciences** _____

Prof. Dr. Cemil Hakan Gür
Head of the Department, **Metallurgical and Materials Eng** _____

Assist. Prof. Dr. Mehmet Kadri Aydınol
Supervisor, **Metallurgical and Materials Eng** _____

Examining Committee Members:

Prof. Dr. Tayfur Öztürk
Metallurgical and Materials Eng, METU _____

Prof. Dr. Mehmet Kadri Aydınol
Metallurgical and Materials Eng, METU _____

Prof. Dr. Emren Nalbant Esentürk
Chemistry, METU _____

Asst. Prof. Dr. Burak Ülgüt
Chemistry, Bilkent _____

Asst. Prof. Dr. Berke Pişkin
Metallurgical and Materials Eng, Muğla Sıtkı Koçman Uni. _____

Date: 12.02.2021

I hereby declare that all information in this document has been obtained and presented in accordance with academic rules and ethical conduct. I also declare that, as required by these rules and conduct, I have fully cited and referenced all material and results that are not original to this work.

Name, Last name :Burcu, Arslan Hamat

Signature :

ABSTRACT

DEVELOPMENT AND CHARACTERIZATION OF CATALYST MATERIALS OF ZINC-AIR BATTERIES

Arslan Hamat, Burcu
Doctor of Philosophy, Metallurgical and Materials Engineering
Supervisor: Prof. Dr. Mehmet Kadri Aydınol

February 2021, 127 pages

Recently, primary and secondary zinc-air batteries have attracted considerable attention due to their high energy density, safety, availability and low cost. Zinc-air batteries generate electricity through a redox reaction between zinc and oxygen in air. Zinc-air batteries have higher theoretical energy density due to abundant supply of oxygen from the atmosphere. However, poor efficiency of the oxygen reduction (ORR) and evolution reactions (OER) taking place at the cathode limits the use of zinc-air battery in demanding applications. The aim of this study is to produce and characterize a novel unifunctional and/or bifunctional catalyst material to be used in the cathode.

The aim of this study is to investigate the electrochemical activity of Mn-based oxides, α-MnO_2, Mn_2O_3 and Mn_5O_8, Ag-based oxides, Ag_2XO_4 (where X= Cr, Mo, and W), and Cu-based delafossite oxides, $CuXO_2$ (where X= Co and Cr), to be used as a catalyst material. In this regard, precipitation, spray pyrolysis, sol-gel and hydrothermal methods were used to synthesize fine-sized powders.

Structural characterizations were performed by SEM and XRD prior to use of synthesized powders. Then, linear sweep voltammograms of catalysts loaded

rotating disk electrode and gas diffusion layer were investigated via a three-electrode cell in 0.1 M and 6 M KOH electrolyte, respectively. The most promising results for ORR were obtained from Ag_2WO_4 powders. The $CuCrO_2$ powders synthesized through hydrothermal method at 210 ^oC gave the most promising results for OER activity which has the highest surface area. However, activity loss of $CuCrO_2$ at high oxidative potentials were reported.

Keywords: Powders: Chemical Preparation; Complex Oxides; Oxygen Reduction Reaction; Oxygen Evolution Reaction; Electrocatalysts

ÖZ

ÇİNKO-HAVA BATARYALARININ KATALİZÖR MALZEMELERİNİN GELİŞTİRİLMESİ VE KARAKTERİZASYONU

Arslan Hamat, Burcu
Doktora, Metalurji ve Malzeme Mühendisliği
Tez Yöneticisi: Prof. Dr. Mehmet Kadri Aydınol

Şubat 2021, 127 sayfa

Son zamanlarda, birincil ve ikincil çinko-hava bataryaları yüksek enerji yoğunlukları, güvenilirlikleri, ulaşılabilirlikleri ve düşük maliyetleri nedenleriyle önemli ölçüde ilgi çekmektedir. Çinko-hava bataryaları çinko ve havadaki oksijen arasında oluşan redoks reaksiyonu yoluyla elektrik üretmektedir. Atmosferden sağlanan bol oksijen nedeniyle çinko-hava bataryaları yüksek teorik enerji yoğunluğuna sahiptir. Fakat katotta meydana gelen oksijen indirgenme ve açığa çıkma reaksiyonlarının düşük verimlilikleri, çinko-hava bataryalarının ihtiyaç duyulan uygulamalarda kullanımını sınırlandırmaktadır. Bu çalışmanın amacı katotta kullanılacak yeni, tek ve/veya iki işlevli katalizör malzemesinin üretilmesi ve karakterize edilmesidir.

Bu çalışmanın amacı, katalizör olarak kullanılacak Mn bazlı oksitlerin, α-MnO_2, Mn_2O_3, Mn_5O_8, Ag bazlı oksitlerin, Ag_2XO_4 (X= Cr, Mo ve W), ve Cu bazlı delafosit oksitlerin, $CuXO_2$ (X=Cr ve Co), elektrokimyasal aktivitesinin araştırılmasıdır. Bu çalışmada, küçük tane boyutlu tozların sentezi için çökelme, sprey piroliz, sol-jel ve hidrotermal yöntemleri kullanılmıştır.

Sentezlenen tozlar kullanılmadan önce taramalı elektron mikroskobu ve x-ışını kırınımı yöntemleri ile karakterize edilmiştir. Daha sonra, döner disk elektrotuna ve gaz difüzyon tabakasına yüklü katalizörlerin sırasıyla 0.1 ve 6 M KOH elektrolit içeren üç elektrotlu hücrede doğrusal tarama voltamogramları incelenmiştir. Oksijen indirgenme reaksiyonu için en umut vaat edici sonuçlar Ag_2WO_4 tozlarından elde edilmiştir. Ayrıca 210 ^oC'de hidrotermal yöntemle sentezlenen, en yüksek yüzey alanına sahip olan $CuCrO_2$ tozları, OER aktivitesi için en umut verici sonuçları vermiştir. Fakat yüksek potansiyellerde $CuCrO_2$ tozlarının aktivite kaybı bildirilmiştir.

Anahtar Kelimeler: Toz: Kimyasal Hazırlama, Kompleks Oksitler, Oksijen İndirgeme Reaksiyonu, Oksijen Açığa Çıkarma Reaksiyonu, Elektrokatalizörler

To My Family

ACKNOWLEDGMENTS

I would like to express my deepest gratitude to my advisor Prof. Dr. Mehmet Kadri Aydınol for guidance, advice, criticism and insight throughout the research. I would also like to thank Prof. Dr. Tayfur Öztürk and Prof. Dr. Emren Nalbant Esentürk for their suggestions, comments and insight throughout the research. I also wish to express my gratitude to Asst. Prof. Dr. Burak Ülgüt and Asst. Prof. Dr. Berke Pişkin for their suggestions and comments.

I would like to thank Mehmet Alican Noyan, Kadir Özgün Köse, Cansu Savaş Uygur, Arife Derya Deniz Kaynar for their friendships and help.

My special thanks go to Özgür Hamat for his encouragements, support and friendship throughout this study.

Many thanks go to my parents Selma Arslan and Hasan Arslan and my sister Işıl Arslan Çelebi for their support not only throughout this thesis but also in my whole life.

TABLE OF CONTENTS

LIST OF TABLES

TABLES

LIST OF FIGURES

FIGURES

CHAPTER 1

INTRODUCTION

1.1 Metal-Air Batteries

The need for electrical energy is increasing every day due to industrialization. Furthermore, the potential environmental hazards associated with the existing energy production methods and low energy conversion efficiency are the main problem worldwide. There is a huge demand for clean, safe, efficient, reliable, affordable, portable energy storage and conversion devices all around the world such as batteries, fuel cells, solar cells and supercapacitors [1]–[4]. The oxygen reduction and evolution reactions are some of the most essential electrochemical reactions. Indeed, oxygen reduction reaction (ORR) is essential for the development of promising technologies of energy storage and conversion such as metal-air batteries and fuel cells [5], [6]. Moreover, the oxygen evolution reaction (OER) is also again for the development of metal-air batteries, fuel cells, as well as water splitting and photo-electrochemical cells [7].

Primary and secondary metal-air batteries, especially Zn-air, has recently received a substantial degree of attention, particularly owing to their high energy density, availability, safety, and low cost [1], [8], [9]. A metal anode, a porous air electrode on the cathode side with an electroactive catalyst material, an electrolyte and a separator are the main components of the metal-air batteries. Metal-air batteries use a chemical reaction between the metal and the abundant supply of cathode reagent, oxygen, from the surrounding atmosphere to produce electricity. Oxygen diffuses through pores of the air cathode, and the reduction of oxygen to hydroxide ion occurs at the gas, liquid, solid three-phase zone when oxygen arrives at the catalyst surface.

This type of battery can be considered as being between traditional fuel cells and conventional batteries because of the similarities of the structure of positive porous electrode and negative electrode sides.

Metal-air batteries, such as Zn-air [8]–[10], Li-air [10], [11], Al-air [12], [13] and Mg-air [14], have high theoretical energy density because of the abundant supply of cathode reagent, O_2, from the surrounding atmosphere. The ORR and OER; however, also have negative consequences on the battery performance. The ORR and OER are known to be the kinetically limiting reactions that control the power output of metal-air batteries due to their high reaction energy barrier [10]. Therefore, the obstacle towards their usage must be resolved, which can be achieved by finding an appropriate bifunctional catalyst to decrease the high reaction energy barrier (overpotential). In other words, the air electrode production with an appropriate catalyst will be playing a significant role in determining the performance of the battery. Moreover, the improvement of these reactions for fuel cells, water splitting processes and photo-electrochemical cells are highly crucial [15], [16].

Zinc-air batteries have cost, safety and performance benefits over the other metal-air batteries, details can be seen in Chapter 2. The history of the first manufactured zinc-air battery goes back to 1878 [17] whereas commercial product was put on the market in 1932 [18]. Commercialized non-rechargeable zinc-air batteries have been used for many years such as hearing aids, navigation lights and railway signals [19], [20] that have high energy density with very low power. The commercialization of a secondary zinc-air battery was achieved in 2012 [19]. Moreover, recently various companies have dealt with the commercialization of these batteries such as NantEnergy (formerly Fluidic Energy), EOS Energy Storage, Rayovac, Powerone, ZincNyx, Zenipower, Renata, Electric fuel, EFB Power, Revolt and Zoxy Energy Systems [17], [19], [21]. Even though the investment of metal-air batteries was achieved on a century ago, problems associated with the anode, air electrode, electrolyte and catalysts hindered the large scale industrial development. To fulfill the potential of metal-air batteries, problems related with the anode, cathode and electrolyte should be solved.

1.2 Aim of This Work

Metal-air batteries have received broad attention due to their high energy density; however, the ORR and OER are known to be the kinetically limiting reactions that control the power output of metal-air batteries because of their high reaction energy barrier [5], [10]. In other words, the air electrode production with an appropriate catalyst will be playing a major role in determining the performance of the battery. The lack of active catalysts with a low cost and high alkaline stability is the major retardation of the commercialization of metal-air batteries.

The improvement of ORR kinetics is crucial for not only metal-air batteries but also many electrochemical energy conversion and storage technologies such as direct methanol and polymer electrolyte membrane fuel cells, photo-electrochemical cells [16], [22]. Therefore, the obstacle towards their usage must be resolved, which can be achieved by finding an appropriate catalyst to decrease the high reaction energy barrier (overpotential) for the oxygen reduction reaction.

Primary zinc-air batteries have already been commercialized [23]. However, to produce secondary metal-air batteries, OER activity is vital. The improvement of oxygen evolution reaction kinetics is not only crucial for metal-air batteries but also vital reaction for electrochemical energy conversion and storage technologies include fuel cells, photo-electrochemical cells, water splitting processes, etc. [16], [22]. For example, hydrogen production with water splitting reaction has got attention recently. The hydrogen and oxygen gases evolution occurred during the water splitting reaction. However, sluggish reaction kinetics of OER limits the water splitting reaction. The obstacle towards usage of these energy conversion and storage technologies must be resolved, which can be achieved by finding an appropriate catalyst to decrease the high reaction energy barrier (overpotential) for evolution reaction. Thus, this research was focused on catalyst development for the ORR and OER.

The state of the art catalyst, Pt for ORR in alkaline and acid medium is known for many years [24]. However, widespread applications of these are not common due to its high cost and scarcity. Therefore, there have been many studies in the literature focusing on the development of catalyst materials to change the sluggish kinetics of this reaction [6], [25], [26]. Catalysts such as noble metals and alloys include Pt, Ru, Ag and non-noble powders such as metal oxides in the form of perovskites (La-based perovskite oxides), pyrochlores, spinels (Co_3O_4), MnO_2, trimetallic metal-organic framework composites (W/Co/Fe MOFs-derived carbon nanoflakes, Co/Fe/Ni-MOFs-derived carbon-based nanoflower) and core-shell composites have been investigated to enhance the performance of batteries [25]–[34]. Especially, transition metal oxides (containing Co, Mn, Ni) which consist of oxidized redox couples are the foremost promising bifunctional electrocatalysts in alkaline electrolytes [35].

The state of the art catalysts for OER in the alkaline medium are ruthenium oxide (RuO_2) and iridium oxide (IrO_2) [36]. Similarly, their high cost limits their usage. Therefore, there have been many studies in the literature focusing on the development of efficient and readily available catalyst materials to change the sluggish kinetics of this reaction [9], [37]–[40].

Many strategies have been followed such as doping of a known catalyst, alloying, combining more than one catalyst (hybrid bifunctional catalyst) and designing a new catalyst consisting of active elements [25], [38], [41]–[44]. In this study, Mn-based oxides, MnO_2, Mn_2O_3 and Mn_5O_8, were investigated because Mn_xO_y oxides are one of the most widely researched electrocatalysts for oxygen reactions [25], [45]. Indeed, number of crystal structure of Mn_xO_y is higher than 30. Besides, Mn can exist in different oxidation states in these oxides such as: Mn^{+2}, Mn^{+3}, Mn^{+4}, Mn^{+6} and Mn^{+7}. Crystalline phases and structures, morphologies, porosity levels and electrical conductivities and valence states (especially Mn^{+3} and mixed Mn^{+3}/Mn^{+4}) of Mn_xO_y powder are correlated with the catalytic activity [46]. For example, the electrocatalytic behavior of MnO_2 powders was strictly linked to the crystal structure. The ORR activity decreases in the following order: α- > β- > γ-MnO_2. The Mn-based oxide is also found in the enzymes that catalyze the OER, which consist

of Mn, Ca and 4 O ions [47]. In this study, MnO_2 (Mn^{+4}), Mn_2O_3 (Mn^{+3}) and Mn_5O_8 ($Mn^{+2}2\ Mn^{+4}3$) were selected to be investigated in ORR and OER ranges. The aim is to investigate the activity of these oxides and synthesize a benchmark catalyst to compare through the thesis study.

In this study, Ag-based oxides were also investigated because the high catalytic activity of silver and silver particle decorated oxides have already been investigated and the results were very promising [30], [48]–[50]. Indeed, Ag is one of the most promising candidates to be an ORR catalyst because of its stability and activity in alkaline electrolytes [49], [50]. Even though the catalytic activities of Ag and Ag compounds are well known [41], [48], Ag-containing compounds, silver chromate, silver molybdate and silver tungstate, with the same formula as Ag_2XO_4 (X= Cr, Mo, and W) have not been investigated for both the ORR and OER. However, in the literature, there is a lot of research focused on these compounds to be used as photoluminescent materials, cathodes of lithium batteries and photocatalysts [51].

Another type of oxides investigated in this study is copper delafossite oxides. To mimic nature, several enzymes and proteins, which showed catalyst activity to bind O_2, were investigated [52]. For example, laccases enzyme, which containing multicopper oxidase, enhance the oxygen reduction reaction. According to the investigation, proteins and enzymes consist of copper sites with an interatomic copper distance of 0.36 nm catalyze the oxygen reactions. The interatomic distance of copper delafossite oxides, $CuXO_2$, is between the value of 0.285 – 0.383 nm by changing X site ion. Moreover, according to recent researches, copper-based oxides such as Cu-Cu_2O-CuO [35], $CuCo_2O_4$ [53] catalyze the water oxidation and ORR and OER, respectively. This might manifest for the copper delafossite to be a candidate for oxygen evolution reaction.

A remarkable effort has been devoted to investigating copper delafossite oxides because of their electrocatalytic [54], [55], optical [56] and photoelectrochemical properties [57]. Besides, copper delafossites can be synthesized through numerous production methods with low cost such as solid-state reaction [57], sol-gel [56],

hydrothermal [58]. Moreover, multiple oxidation states of ions in these oxides are good descriptor for activity [52].

The electrocatalytic activities of powders can be changed even by altering the synthesis technique because strong variations as a function of size are observed not only in their physical and electrical properties but also in their chemical behaviors. For example, when particle size decreases, the fractions of atoms at the surface increases. Therefore, the average binding energy per atom is higher [59]. Moreover, defect states might have an important effect on charge transfer [59]. In other words, the preparation method of catalyst might play a prominent role in chemical activity. Numerous methods have been used to obtain these oxides such as reverse micelle [51] and precipitation [60]. However, each production method results in different particle sizes, morphologies and surface areas. The effect of each difference of these brings about different specific and mass activities [45].

Insufficient information about the ORR and OER activities of these oxides in alkaline solution led us to complement the literature. In this study, the oxygen reaction activity of Mn-based oxide, MnO_2, Mn_2O_3 and Mn_5O_8, Ag-based oxides, Ag_2XO_4 (where X= Cr, Mo, and W) and copper delafossite oxides, $CuCoO_2$, $CuCrO_2$ was investigated in detail. Structural characterizations were performed by scanning electron microscope (SEM) and X-ray diffraction (XRD) and BET before the use of synthesized powders for electrochemical tests. After structural characterization, electrochemical tests were conducted in an alkaline medium. Figures of merit to be an ORR catalyst were compared with the synthesized α-MnO_2 and commercial Pt/C catalysts. Figures of merit to be an OER catalyst were compared with the synthesized $CuCoO_2$ and commercial 67 wt% Pt/C and Ru-Pt catalysts at rotating and non-rotating conditions.

CHAPTER 2

LITERATURE REVIEW

2.1 Operation Principles of Metal-Air Batteries

The structure of metal-air batteries can be seen in Figure 2.1. These batteries use a chemical reaction between the metal and the gaseous oxygen in the air to produce electricity. The O_2(g) diffuses through pores of the air cathode, and the reduction of O_2 to OH^- ion occurs at the gas, liquid, solid three-phase zone when oxygen arrives at the catalyst surface, while the oxidation occurs at the negative electrode, the metal side, during discharging. The reactions of oxygen reduction reaction (ORR) occurred at porous electrode and oxidation of anode metal M during discharging can be written as follows:

$$O_2 + 2H_2O + 4e^- = 4OH^- \quad E^o = +0.401 \text{ V vs NHE} \tag{2.1}$$

$$M = M^{n+} + ne^- \tag{2.2}$$

Depending on the metal, the equilibrium potential of the battery is changed. In the reverse case (during charging), the O_2 and M metal are regenerated. The generalized total discharge reaction may be written as follow:

$$4M + nO_2 + 2nH_2O = 4M(OH)_n \tag{2.3}$$

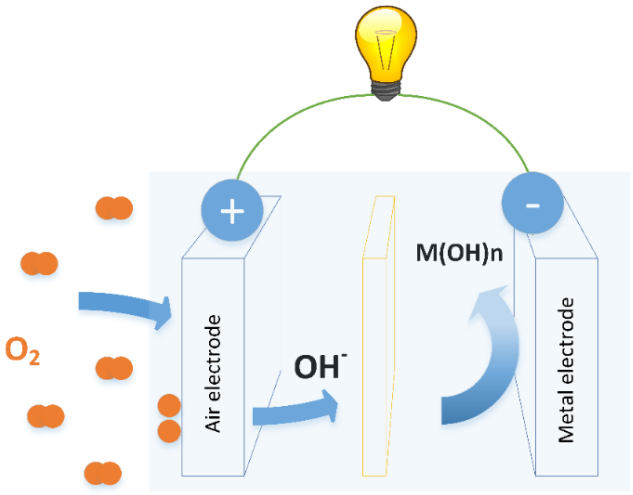

Figure 2.1 Schematic representation of a metal-air battery.

The advantages of these batteries include available high energy density, a flat discharge curve, great shelf life (sealed), safety, ecological and financial benefits [61]. On the other hand, the performance of these batteries depends on environmental conditions. Once these batteries open to air, drying or flooding affects the service life of batteries. The water amount is changed depending on partial pressures of the potassium hydroxide electrolyte and environment. The typical electrolyte is composed of 30 % concentration of potassium hydroxide aqueous solution. The water amount decreases in the typical electrolyte when the humidity was kept lower than sixty percent and temperature at 25 ^{o}C. Vice versa is true when the humidity exceeds that threshold. Moreover, carbonation of the electrolyte, limited operating temperature range, limited power output and side reaction (H_2 evolution due to anode corrosion) are the major disadvantages. The advantages and problems of zinc-air batteries will be explained in detail.

2.2 Types of Metal-Air Batteries

The reactive metal anode is electrochemically coupled with a porous air electrode to give very high specific energy. One of the active material (oxygen) is abundant. The

greater part of the cell's volume composes of anode material. Hence, metal-air batteries possess a high volumetric energy density when compared to the other primary and secondary batteries as seen in Figure 2.2.

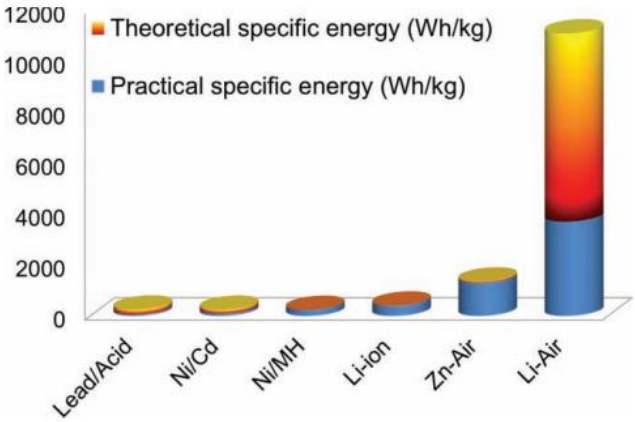

Figure 2.2 Theoretical and practical energy densities of different types of batteries [62].

The reactive anode determines the capacity of metal-air batteries due to the abundant oxygen is supplied from the atmosphere. The list of metals used in metal-air batteries can be seen in Table 2.1. Compared with the other metal anodes, the capacity of zinc is less than the others [61]. However, zinc-air batteries have also drawn considerable scientific and technological interests due to their relative stability in alkaline aqueous electrolytes, good environmental compatibility, reversibility and abundance.

Table 2.1 Properties of metal-air batteries [61].

Metal anode	Electrochemical equivalent of metal, Ah/g	Theoretical cell voltage, V	Valence change	Theoretical specific energy, kWh/kg	Practical operating voltage, V
Li	3.86	3.4	1	13.0	2.4
Ca	1.34	3.4	2	4.6	2.0
Mg	2.20	3.1	2	6.8	1.2-1.4
Al	2.98	2.7	3	8.1	1.1-1.4
Zn	0.82	1.6	2	1.3	1.0-1.2
Fe	0.96	1.3	2	1.2	1.0

Lithium is used in various types of batteries because of having the highest theoretical voltage and electrochemical equivalence. Lithium-air batteries have drawn attention due to the huge difference in the specific energy. Theoretical and practical energy densities of various types of batteries can be seen in Figure 2.2 and Table 2.1. Not only lithium but also aluminum, magnesium and calcium-air batteries have high energy density among all metal-air batteries. However, problems such as instability, safety, polarization, corrosion and cost have limited progress of commercialization of lithium, calcium and magnesium air batteries. The development of aluminum and magnesium batteries has concentrated on reserve and mechanically rechargeable designs because water is preferentially electrolyzed in aqueous systems. Moreover, aluminum-air [12] and magnesium-air [63] batteries based on ionic liquid electrolyte has been developed. Specific capacity and voltage of different metal-air batteries in aqueous electrolytes can be seen in Figure 2.3. The specific capacity of iron, cadmium and lead-air batteries are relatively lower than zinc-air batteries as seen in Figure 2.3. Besides, zinc-air batteries have performance and safety advantages over other metal-air batteries.

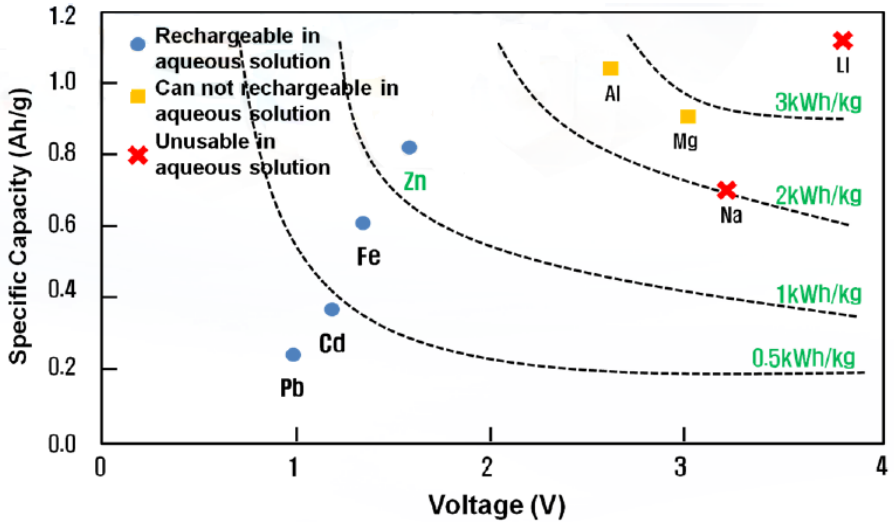

Figure 2.3 Metal-air batteries in aqueous solution [64].

2.3 Operation Principles of Zinc-Air Batteries

Primary, secondary (two electrodes) and mechanically rechargeable zinc-air batteries generally consist of zinc anode, porous air cathode, alkali aqueous electrolyte and separator. The porous air cathode may be divided into a catalyst loaded layer and gas diffusion layer (GDL). Polytetrafluoroethylene (PTFE) film and nickel mesh current collector may be used to prevent water transfer and increase current collection efficiency for some applications, respectively.

When the seal on the air electrode is opened, O_2 diffuses through the porous layer and reduction of O_2 to OH^- ion occurs while Zn is oxidized at the metal side. Indeed, the oxidized Zn causes soluble zincate ions ($Zn(OH)_4^{2-}$) formation. After the saturation point of zincate ions ($Zn(OH)_4^{2-}$), ZnO precipitates starts to form. Schematic drawing of zinc-air batteries and discharge reactions can be seen in Figure 2.4.

In reverse situation (during charging), O_2 evolution and zinc regeneration occur at positive and negative electrodes, respectively. During discharge and charge, the reactions can be written as [20]

During discharge:

Metal electrode: $Zn + 4OH^- \rightarrow Zn(OH)_4^{2-} + 2e^-$ (E^o = 1.25 V vs. NHE) (2.4)

$Zn(OH)_4^{2-} \rightarrow ZnO + H_2O + 2OH^-$ (2.5)

Air electrode: $O_2 + 4e^- + 2H_2O \rightarrow 4OH^-$ (E^o = 0.40 V vs. NHE) (2.6)

Total reaction: $2Zn + O_2 \rightarrow 2ZnO$ (E^o = 1.65 V vs. NHE) (2.7)

Parasitic reaction: $Zn + 2H_2O \rightarrow Zn(OH)_2 + H_2$ (2.8)

During charge:

Metal electrode: $ZnO + H_2O + 2OH^- \rightarrow Zn(OH)_4^{2-}$ (2.9)

$Zn(OH)_4^{2-} + 2e^- \rightarrow Zn + 4OH^-$ (2.10)

Air electrode: $2OH^- \rightarrow 1/2O_2 + 2e^- + H_2O$ (2.11)

Total reaction: $2ZnO \rightarrow 2Zn + O_2$ (2.12)

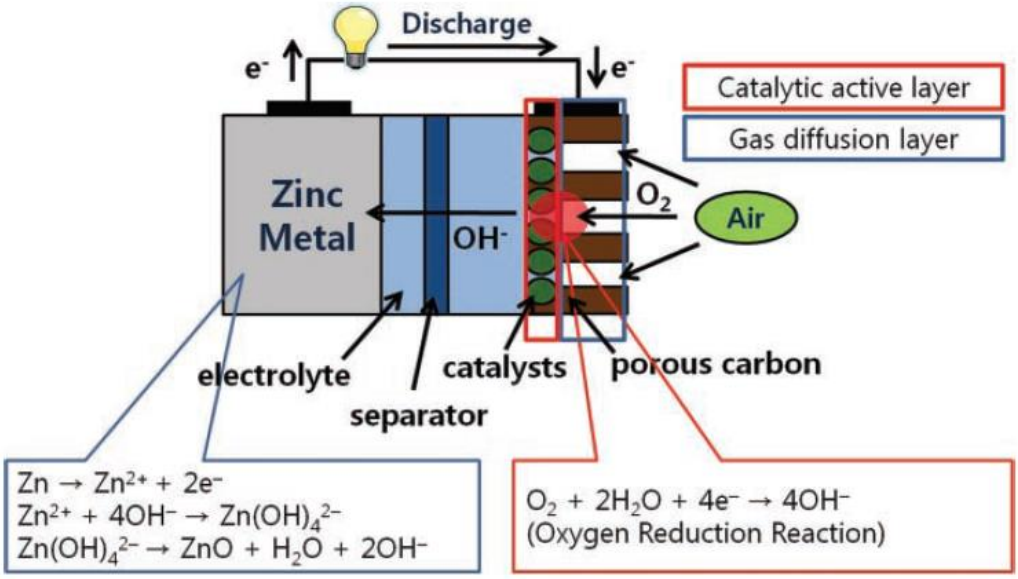

Figure 2.4 Schematic drawing and electrode reactions of zinc-air batteries during discharge [62].

2.3.1 Zinc Electrode

The oxidation of Zn occurs during the charging step that creates Zn^{+2} ion and releases electron. Zinc (II) and hydroxide ion combine to form $Zn(OH)_4^{2-}$ until the saturation point in the alkaline medium is reached. After the saturation point, ZnO formation is observed that acts as an insulator. This decomposition causes approximately 27 % volume expansion [64]. Therefore, an appropriate amount of empty place must be designed for the zinc-air battery assembly.

The improvement of the performance of zinc-air batteries has been studied by increasing the surface area of the zinc particles because zinc participates in the redox reactions. Fine-sized zinc structures can react more efficiently. Especially, large surface area is preferred to increase discharge performance at high drain rates. Increasing the surface is also an advantage for utilizing the zinc because of decreasing the effects of an insulating layer (zinc oxide) formation.

Conventional zinc anode, consists of zinc powder and polymer binder, revealed that utilization of theoretical discharge capacity of zinc anode was less than 60 % because zincate ions dehydrate to insulating ZnO layer between zinc surfaces. That interrupts the electronic conductivity. Besides, rechargeability of the battery is limited due to this problem [65]. Therefore, the various morphologies of porous zinc electrodes have been fabricated by using powder, dendrite, granule or filament to solve this issue [20].

Long, et al. [65] produced zinc sponge with a porous monolithic, three dimensional structure. The utilization of zinc metal approached to the 90 % in a primary zinc battery. In conventional zinc anode, some of the zinc particles were covered with a resistive ZnO layer. During charging, some of them are dissolved; however, insulating ZnO leads to zones of high local current densities which promotes the dendritic growth of zinc. When the dendritic form makes a hole in the separator, a short circuit occurs. These problems were prevented and the capacity of the battery was enhanced by using sponge-like zinc anode [65].

High surface area is needed for a high power system; however, the corrosion rate of zinc increases because of being more exposed to the alkaline electrolyte. The undesired side reaction between water and zinc gives rise to H_2(g) evolution. Besides, this side reaction gives rise to corrosion of Zn side that results in capacity loss and eventually reducing the lifespan of the battery. Normally, the rate of zinc corrosion is not fast with respect to other metals used as anode in metal-air batteries. However, during the anodic discharge of the battery, as it is seen from the parasitic reaction, H_2(g) evolution is problematic. Many strategies have been made to restrain the self-corrosion of Zn electrode. One is the alloying of zinc with other metals which have high hydrogen evolution overvoltage. The reduction potential of zinc is more negative than hydrogen, which spontaneously leads to hydrogen gas evolution on the surface of zinc particles [66]. It was reported that alloying of Zn with Ni and In is effective in shifting the hydrogen evolution potentials to the more negative values [62]. Another method is the coating of the Zn anode with other materials (e.g. Al_2O_3) [66]. Lee et al. [66] reported that Al_2O_3, having high hydrogen evolution

overpotential, is uniformly coated on the zinc surfaces with chemical solution process. The coating layer is believed to prevent the zinc surface from directly facing the alkaline electrolyte, which helps the zinc to escape side reactions in the cell. Introducing additives (e.g. zinc oxide, silicon dioxide and surfactants) is also a solution to overcome hydrogen evolution [67].

Another limitation of zinc anode is that dendritic morphology forms during the charging step, as stated before. Dendrite formation is more problematic at a high charging current that is needed for short charging times. Several methods have been searched to solve zinc regeneration problems. One is already explained as designing a porous electrode to inhibit the growth of zinc dendrites. Furthermore, the orientation of the battery affects the deposited zinc morphology. Horizontal orientation gives better deposit quality in terms of compactness and uniformity [68]. Flowing electrolytes is also beneficial to obtain a more uniform zinc deposit [68]. The controlling of growth of dendrites at high charging currents have also been studied by pulse and pulse reverse modes. To show the distinct results in morphology, direct current and pulsating current were compared. Current interruption time (t_{off}) allows ions to diffuse; therefore, high current densities can be applied without drastically changed morphology [68].

The other way to improve the performance of the zinc-air battery is that the addition of alcohols and acetates into the electrolyte prevents the transformation of zincate into ZnO. When these were added, modified zincate ions were formed which slows down the transformation into ZnO. The reverse reaction is very slow once ZnO is formed, since ZnO is a weak conductor and has very low electrolyte solubility. The reversibility of the zinc-air battery can also be increased by adding alcohol and acetate into the electrolyte [69].

2.3.2 Electrolyte

As a medium of ionic migration during discharge and charging, the electrolyte plays an important role. The electrolyte's conductivity, therefore, affects the ohmic resistance of the battery. There are different types of electrolytes, such as alkaline aqueous solution, electrolyte gel and ionic liquids [20].

The oxygen reduction mechanism has quite a difference in alkaline, acid and aprotic electrolytes. Pt remains the acid-based fuel cell catalyst of choice; non-Pt catalysts can, however, be used in alkaline electrolytes [70]. Compared to the alkaline medium, higher overpotential is necessary in the acid medium. Besides, in the aprotic electrolyte, oxygen electrocatalysis is significantly different from that in an aqueous electrolyte. Due to the dendrite-free zinc formation during the charging phase, the cycleability of zinc-air batteries was improved by the use of aprotic electrolytes. These electrolytes have also solved several issues such as corrosion of zinc, dehydration and carbonation of the electrolyte. However, until today, no aprotic electrolyte has approached the efficiency of zinc-air batteries using alkaline electrolytes because the lower ion conductivity of ionic liquids is a challenge up to now [20]. Therefore, aqueous alkaline electrolytes, potassium hydroxide (KOH) or sodium hydroxide (NaOH) are generally used. Solutions of KOH are usually preferable rather than NaOH solutions due to their higher ionic conductivity and oxygen diffusion coefficients, and lower viscosity. The electrolyte concentration is selected to minimize zinc corrosion and obtain good ionic conductivity, increase the solubility of ZnO. Generally, concentrated KOH solutions have been used to prevent the passivation of zinc by the formation of ZnO. When the pH of the electrolyte is below the 13 value, as can be seen in Figure 2.5, the fraction of ZnO increased, which is inconvenient for battery performance [71]. Due to the strong ionic conductivity, optimum solubility of ZnO and limited Zn corrosion, 6 M KOH is commonly used.

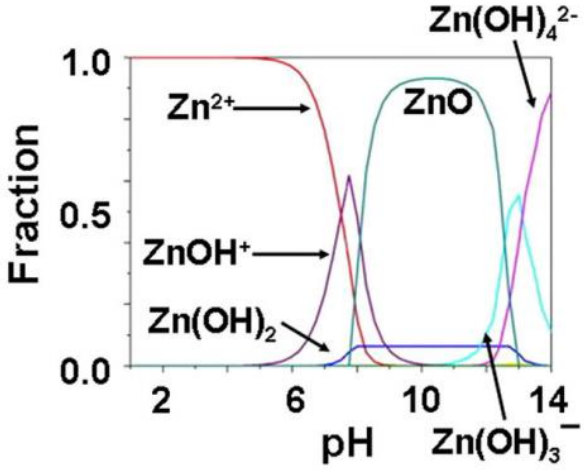

Figure 2.5 Fraction of various Zn^{+2} species versus pH graph for the zinc-water system [71].

Carbonation, arising from the capturing of carbon dioxide, from the ambient air, is one of the key problems with these highly concentrated aqueous alkaline electrolytes. Around 0.04 percent of the concentration of this in the ambient air reacts to the alkaline medium to obtain an alkaline metal carbonate and bicarbonate. [61]. There are two important consequences of this situation. The precipitation of carbonates within the pores of gas diffusion electrode shortens the lifespan of the battery. Drillet et al. [72] stated that the bifunctional air electrode can provide an acceptable cycle life output with the use of a CO_2 filter. Besides, the vapor pressure of the electrolyte is increased. Thus, water vapor loss is very problematic, especially in low-humidity conditions. In other words, potassium carbonate formation reduces the current-voltage curves and has a negative effect on the capacity of batteries. In addition, as the percentage of conversion from KOH to K_2CO_3 increases, the electrolyte resistance increases.

Water loss from the liquid electrolytes because of the open-cell structure of the air cathode is the other problem that should be considered. The water amount in the typical electrolyte changes if the humidity at room temperature is different than 60 %. A gel electrolyte can increase the performance of battery and lifespan, and

minimize water loss. According to Othman et al. [73], hydroponics gel is a good candidate to be an electrolyte gelling agent for zinc-air batteries. In literature, the KOH-based gel electrolytes have been investigated to make the solid type electrolyte. Different polymers, used as gelling agents, were investigated such as polyvinyl alcohol, polyethylene glycol, polyvinylpyrrolidone, etc. [74]. The gelatin was used as a gelling agent in KOH-based electrolytes which includes abundant supply of OH^- ions [74]. Flexible, cable type zinc-air batteries have been done by using this gel-type electrolyte.

2.3.3 Separator

The separator in batteries is used to keep apart the cathode and anode to prevent short circuit formation. On the other side, to retain the desired ionic conductivity, the separator is permeable to the electrolyte. Zinc-air battery separators have to have low ionic resistance and high electrical resistance. Besides, separators must resist to the dendritic growth of zinc at the charging step that is one of the important problems. They must provide transportation of the hydroxyl ion (OH^-) from the cathode to the zinc electrode. Electrolyte should have been adsorbed by these separators; however, they should resist to the corrosive medium and oxidation. The pore size and porosity must be considered to select the appropriate separator. Polyethylene, polypropylene, polyvinyl alcohol and polyamide are commonly used materials. Nonwoven separators such as Celgard 4560 and Celgard 5550 are generally used in commercial Zn-air batteries [20]. The structure of a typical separator (Celgard 5550), which has been used in commercial zinc-air batteries, can be seen in Figure 2.6. The porosity in the separator causes migration of not only OH^- ions but also zinc ions. Zinc ions migrate from anode to cathode during the discharging step that decreases the cyclability and capacity of the battery. To prevent this, anion-exchange membranes were developed. The discharge capacity of the battery was increased by six times when the anion-exchange membrane was used instead of Celgard separators. However, the long-term stability of these separators at high alkaline solutions is a

problem to be solved. The amount of loss of their performance after 1000 h holding in the alkaline electrolyte is 10 % [18].

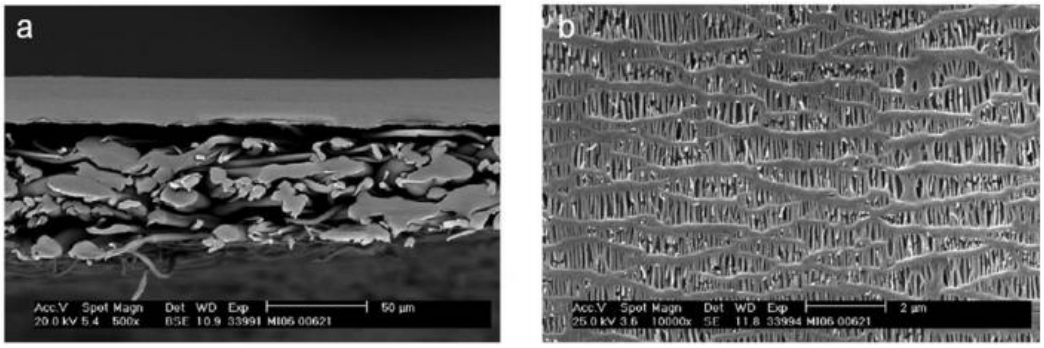

Figure 2.6 (a) Cross-section and (b) microstructure of Celgard 5550 membrane [18].

2.3.4 Air Electrode

The overall reaction of zinc-air battery is the conversion of Zn to ZnO. Zinc metal and oxygen are the only consumed materials. Zn-air batteries require effective air electrodes in order to operate successfully. Theoretically, air electrodes can be used several times until degradation occurs due to the abundant supply of O_2 from the ambient air.

The air electrode performs the oxygen reduction to complete the redox reaction of the battery. Therefore, oxygen firstly must pass through the air cathode to take part in the reaction. In other words, a highly porous cathode structure is needed. Zinc is oxidized while oxygen is reduced to OH^- ion during the discharging step. Formed OH^- ions migrate to the negative electrode and zincate ions form.

The kinetics of ORR is very slow. A catalyst layer is required to accelerate the sluggish ORR. When catalyst materials are only used for ORR, it is called unifunctional catalyst. During discharge and charging steps, bifunctional air

electrodes participate in not only ORR but also OER. Therefore, bifunctional catalyst must be selected for rechargeable batteries.

The cross-section of the porous air electrode can be seen in Figure 2.7. Oxygen diffuses through the highly porous structure, which also functions as a substrate for the catalyst. Porosity also provides a high surface area which means the promotion of reactions. Electrochemical cathode reactions primarily occur in the air electrode at the liquid-gas-solid interface (three-phase zone). Therefore, a suitable air electrode must consist of gas diffusion and catalyst layers. Indeed, the air electrodes have generally several polytetrafluoroethylene (PTFE)-bonded carbon layers with different wettability. Laminated layers of air electrode can be seen in Figure 2.8. The catalyst layer in contact with the electrolyte has to be hydrophilic to the electrolyte while the air side must be hydrophobic to prevent water loss. Moreover, metal current collectors may be applied to improve the electronic conductivity.

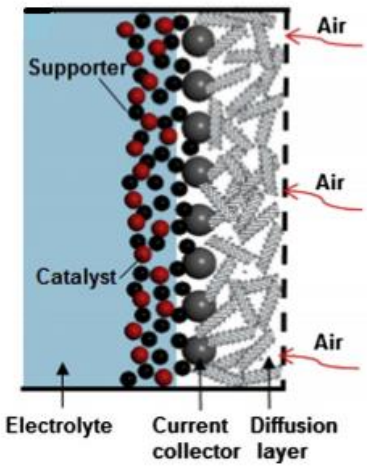

Figure 2.7 Cross-sectional view of the air electrode [20].

Literature survey about air electrode for primary zinc-air cells reveals that it generally consists of [75]:

1. *Teflon film on the air side of the electrode*. High air permeability (2000-4000 s, Gurley method) is necessary to supply required oxygen [75]. It also prevents water loss from the electrolyte that is already mentioned.

2. *Gas diffusion layer (GDL).* Hydrophobicity of one side of the GDL is produced to prevent electrolyte penetration. The hydrophilic counterparts are made of microchannels to get proper wetting on the electrolyte side. Properties can be varied by changing the carbon support, the ratio of carbon to binder and production methods. Even though the production of homemade gas diffusion layers can be found in the literature [75], there are successful examples of commercial gas diffusion carbon paper such as Toray, Sigracet, AvCarb, etc. Carbon fibers and graphitized carbons are generally bounded by PTFE binder in these papers. In this study, Sigracet gas diffusion layers have been used.

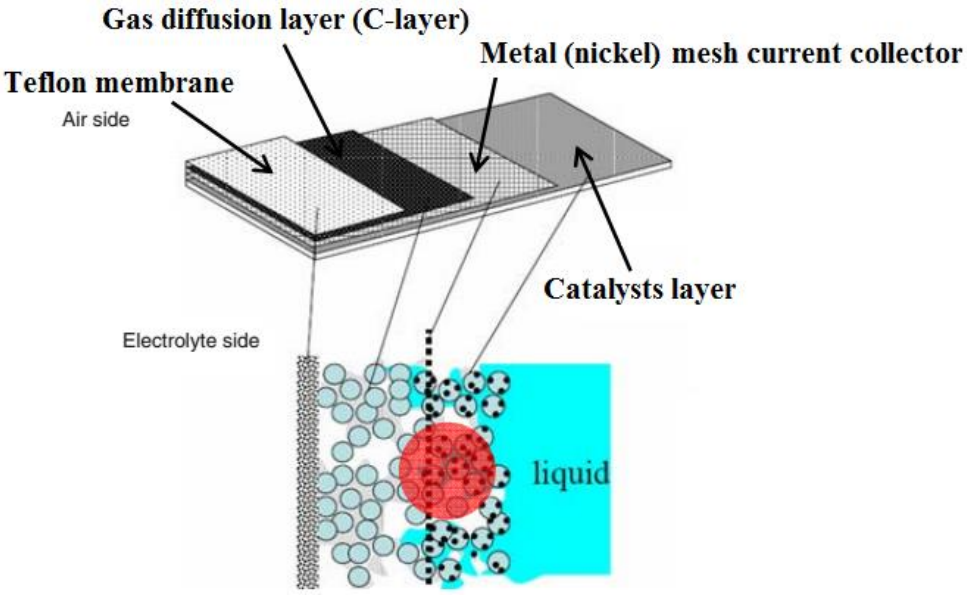

Figure 2.8 Laminated air electrode for zinc-air battery [61], [64].

3. *Current collector.* Metal mesh (generally nickel) or metal foam is used as a current collector. The usage of high surface area nickel foams enhances the efficiency of

porous air cathode [75]. It was reported that the direct growth of catalyst material onto the current collector significantly reduces internal resistance. Co_3O_4 nanowires were synthesized directly onto a stainless steel mesh current collector [76]. By this method, a binder-free, catalyst layer was obtained. Moreover, carbon is not used in the catalyst layer, which may prevent air electrode degradation during the charging step. Extended cycling was achieved and results were attributed to direct synthesizing of Co_3O_4 NW on the stainless steel mesh.

4. *Catalyst layer.* Catalyst layer generally produced by bonding catalyst, carbon black with high BET surface area and PTFE binder. High surface area carbons improve the hydrophilicity. Therefore, these carbons are used to produce the catalyst layer, while low surface area carbon blacks are used to produce the gas diffusion layer, which also promotes the oxygen evolution reaction. The use of acetylene blacks improves the hydrophobic properties of the gas diffusion layer. Besides, PTFE concentrations are generally changed within 10 to 30 % in the active layer to get an optimal balance for hydrophilic properties [75].

2.3.4.1 Limitations of air electrodes

Well balanced performance and service life in the air electrode is required. To increase service life, generally, air excess holes in the battery will be decreased to prevent water loss and flooding. However, the less the access of air to the battery, the lower is the power output. Therefore, air excess is maximized for high power applications, which decreases the service life. The amount of air access to the cell and catalytic activity of the air electrode determines the voltage-current relationship in the battery [61]. Therefore, depending on the type of application, power and service life should be balanced.

Another issue is that degradation of air electrodes generally occurs in the charging process [64]. The reaction occurs at the interface and carbon structure subjects to mechanical pressure, which may cause a mechanical breakdown of the air electrode

(See Figure 2.9). It was reported that the use of low surface area carbon black enhances the oxygen evolution reaction [75].

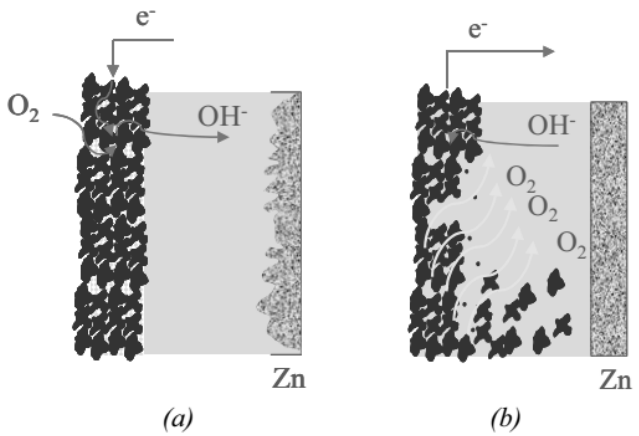

Figure 2.9 Zinc-air cell at (a) charging, and (b) discharging steps [77].

The most important problem of the air electrode is the overpotential. The equilibrium potential of the zinc-air battery is 1.65 V vs NHE because of the explained redox reactions. However, the working voltage is lower than the equilibrium value, typically 1.2 V. For electrically rechargeable batteries, a large charging potential such as 2.0 V or higher is needed to counterbalance the overpotential for oxygen evolution. The variations of charging and discharging voltages from equilibrium are mainly owing to the high overpotentials of ORR and OER. To decrease the overpotentials, unifunctional and bifunctional catalysts are used for primary and secondary batteries, respectively.

The schematic polarization curve of the zinc-air battery can be seen in Figure 2.10. Open circuit potential (equilibrium potential), which can be seen from the black lines in Figure 2.10, is 1.65 V. When current is started to drain from the battery, practical voltage is lower than equilibrium value because of activation, ohmic and concentration loss. As seen from the red line, the overpotential at the zinc electrode is less than that at the air electrode because of the high activation overpotential of

oxygen reduction reaction (green arrow). Moreover, the required voltage in charge is above the equilibrium value that can be seen in Figure 2.10 (blue line). Again, activation overpotential for oxygen evolution reaction is greater than that for zinc regeneration [62].

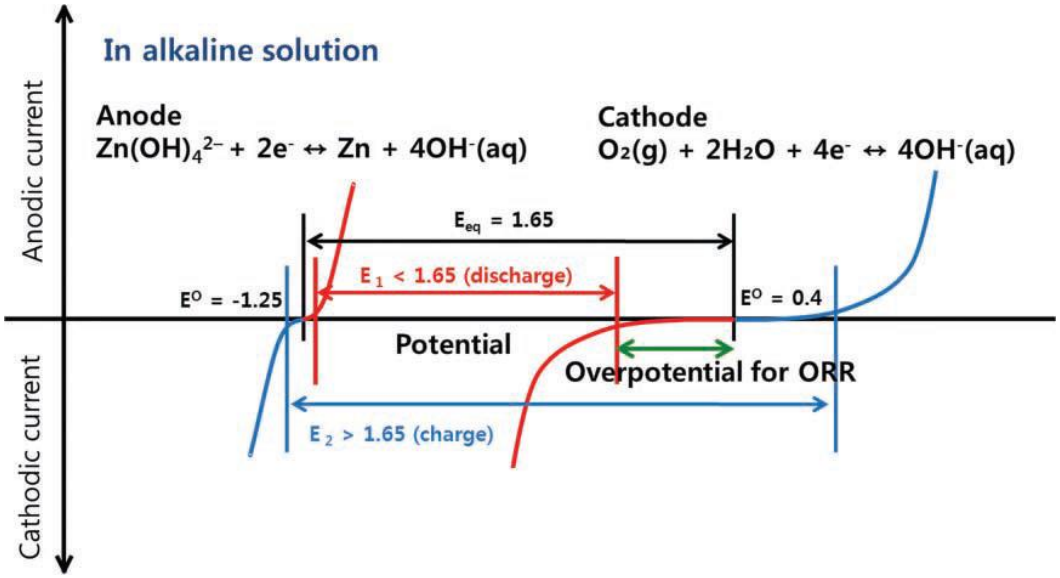

Figure 2.10 Schematic polarization curves of zinc-air battery in aqueous solution. Black lines show the equilibrium potential. Red lines show the potential of zinc-air battery in discharge. Blue lines show the potential of zinc-air battery in charge [62].

The using of ORR and OER have positive and negative effects. High energy density is achieved because of the abundant supply of active material from air, which is already discussed. However, significant voltage loss due to the high activation potential of ORR and OER causes a decrease in power output. These are the main challenges in the commercialization of rechargeable zinc-air battery. Therefore, developing a new catalyst and designing the air electrode must be researched in order to suppress the large overpotential in the redox reaction.

2.4 Catalysts for ORR and OER reactions

Catalyst, which does not influence the thermodynamics, can change the kinetics of a chemical reaction due to the change in the reaction mechanism as it is well known. Progress of a chemical reaction can be seen in Figure 2.11. They are not consumed in the reaction whereas the other reagents participate in the reaction. As seen in Figure 2.11, catalysts can change the reaction speed if a catalyzed chemical reaction has lower free energy of activation than the uncatalyzed reaction. Indeed, catalysts have their selectivity; a specific chemical reaction can be catalyzed by a catalyst.

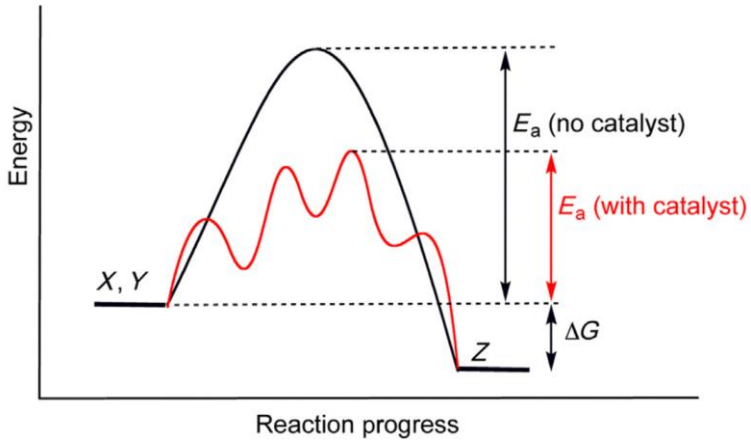

Figure 2.11 Progress of a chemical reaction [78].

Different types of electrocatalysts have been investigated to decrease the voltage loss. Generally, Pt and Pt-Ru alloys have been used as a catalyst; however, they are expensive. Therefore, this is an obstacle to the commercialization of zinc-air batteries. Finding a catalyst for zinc-air batteries can be beneficial for all types of metal-air batteries and fuel cells. Generally, non-noble metal oxide catalysts have been researched in different forms such as spinels, perovskites and pyrochlores, etc. Due to the cost of the used material, these are preferred rather than noble metals to form the porous air electrode [24].

The ORR and OER are series of complex electrochemical reactions, adsorption/desorption, which consists of several intermediate steps and oxygen-containing species such as O, OH, O_2^- , H_2O_2 and HO_2^- [46]. Even though numerous research has been conducted on oxygen catalysis, the mechanistic aspect of oxygen reduction reaction has not been verified [38].

The ORR in the alkaline environment is more favorable than that in the acidic medium due to the better kinetics and lower overpotentials [46]. Binding strengths of adsorbates decrease when the pH of the electrolyte is increased. For example, adsorption of SO_4^{2-} on Pt in acidic media partially occurs; however, it cannot be adsorbed on Pt in a high alkaline solution [38]. Decreasing the adsorption of spectator ions in alkaline media causes a more facile electrochemical reaction. Moreover, various catalysts have been investigated and gave promising results which are similar to the results of the Pt benchmark due to the surface nonspecificity in alkaline medium. On the other hand, catalysts other than Pt have been researched in the acidic medium but does not give the desired results [38], [46]. ORR in the alkaline medium can be written as:

$$O_2 + 2H_2O + 4e^- \rightarrow 4OH^- \ (E^o = 0.401 \text{ V vs SHE}) \quad (2.13)$$

$$O_2 + H_2O + 2e^- \rightarrow HO_2^- + OH^- \ (E^o = -0.076 \text{ V vs SHE}) \quad (2.14)$$

$$HO_2^- + H_2O + 2e^- \rightarrow 3OH^- \ (E^o = 0.87 \text{ V vs SHE}) \quad (2.15)$$

$$2HO_2^- \rightarrow 2OH^- + O_2 \quad (2.16)$$

Oxygen reduction reaction may follow a direct $4e^-$ or $2e^-$ pathway on the surface of the metal catalyst, the pathway of which depends on the catalytic material applied. Furthermore, oxygen reduction reaction can be different even for the same catalyst because of differences in the crystal structure, binding energy and size [46]. The desired pathway for oxygen reduction is the direct reduction (four electrons) as seen from Equation (2.13). Hydrogen peroxide (-1) is produced in a two-electron process

(See Equation (2.14)), which is a very reactive specie that can corrode the components of the battery such as carbon support [79]. Equation (2.14) may be followed by (2.15) or (2.16) equations. Equation (2.15) reveals the further two-electron reduction of peroxide; on the other hand, Equation (2.16) shows the chemical disproportionation of peroxide, these pathways are called as series 2e x $2e^-$ pathways [46].

Schematic drawing of the double-layer structure in front of the air electrode during discharging can be seen in Figure 2.12, in which the inner and outer sphere electron transfer processes were shown. Inner and outer Helmholtz planes (IHP, OHP) and species founded in these areas can be seen in Figure 2.12. Adsorbed OH species, solvent water dipoles and adsorbed O_2 can be seen in the IHP region. The metal ions such as Na^+ and K^+ formed $O_2 .(H_2O)_n$ in the electrolyte and located in the outer Helmholtz layer. The inner sphere electron transfer process can be seen in both acidic and alkaline electrolytes, wherein all the intermediates are adsorbed on the active sites until products are removed from the surface. For example, the pathway of ORR in alkaline and acid electrolytes are founded as similar on Pt-based catalysts [80]. The inner-sphere e^- transfer mechanism includes strong adsorption of molecular O_2 on Pt active sites followed by 4 e^- transfer. However, the outer sphere electron transfer mechanism can only be seen in alkaline electrolyte. The adsorbed hydroxyl species can react with the cluster of $O_2 .(H_2O)_n$ with a hydrogen bond. This weakly absorbed $O_2 .(H_2O)_n$ clusters enhance the $2e^-$ reaction route to HO_2^- [80]. However, surface nonspecificity in alkaline electrolyte due to other sphere e^- transfer process allows usage of various nonprecious and precious metal catalysts rather than noble metals [38].

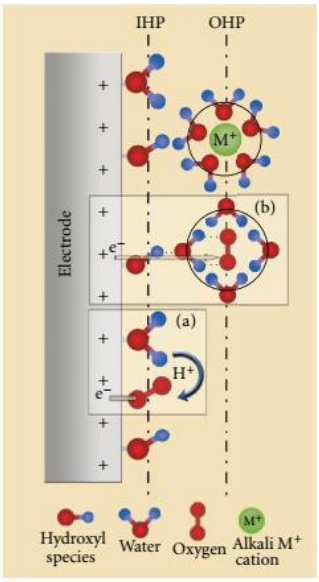

Figure 2.12 Schematic drawing of the double layer at air electrode and electrolyte interface. (a) and (b) shows the inner and outer-sphere e^- transfer processes [80].

Reactions occurred not only depend on the IHP and OHP conditions but also O_2 adsorption configurations on metal and metal oxide surfaces. Differences in the catalytic activities of metal and metal oxides catalysts have also been explained by the effects of the oxygen adsorption configuration and oxygen surface interaction [46]. Various configurations of O_2 adsorption can be seen in Figure 2.13.

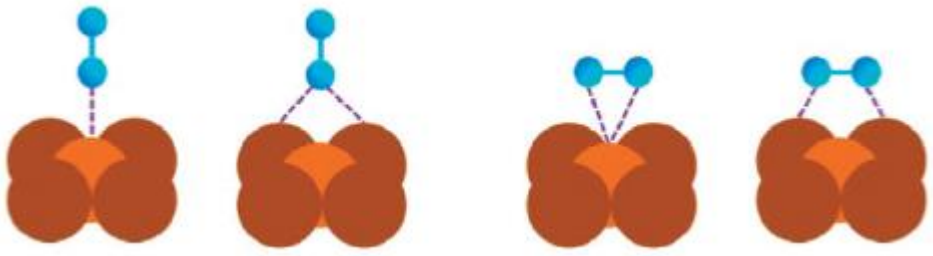

Figure 2.13 Various O_2 adsorption configurations on the surfaces of a catalyst: on top end-on, bridge end-on, bridge side-on one site, and bridge side-on two sites, from left to right [46].

For the end-on manner, just a single oxygen atom is adsorbed perpendicular to the catalytic surface (by a single atom) that leads to a two-electron pathway with peroxide formation. M is used as an abbreviation of metal. Simplified electrochemical catalysis process in the case of end-on adsorption can be written as [46]:

$$M + O_2 \rightarrow M\text{-}(O_2)_{ads} \quad (2.17)$$

$$M\text{-}(O_2)_{ads} + e^- + H_2O \rightarrow M\text{-}(HO_2)_{ads} + OH^- \quad (2.18)$$

$$M\text{-}(HO_2)_{ads} + e^- \rightarrow M\text{-}(HO_2^-)_{ads} \quad (2.19)$$

The above reaction may be completed by either Equation (2.15) or (2.16). The two-electron pathway for oxygen electrochemical reduction reaction by outer-sphere electron transfer process was also reported by Ramaswamy et al. [80]. The interaction of $[O_2 \cdot (H_2O)_n]$ clusters with adsorbed hydroxyl species assists a two-electron route to HO_2^- anion as a reaction product which desorbs from the surface. The steps of the reaction can be written as follows [80], each of them also consists of several intermediate steps.

$$M\text{-}(OH)_{ads} + [O_2 \cdot (H_2O)_n]_{aq} + e^- \rightarrow M\text{-}OH + (HO_2\bullet)_{ads} + OH^- + (H_2O)_{n-1} \quad (2.20)$$

$$(HO_2\bullet)_{ads} + e^- \rightarrow (HO_2^-)_{ads} \quad (2.21)$$

$$(HO_2^-)_{ads} \rightarrow (HO_2^-)_{aq} \quad (2.22)$$

The effect of O_2 adsorption parallel to the catalytic surface plane is the direct reduction of O_2 to OH^- without HO_2^- production, that necessitates the existence of active sites side by side. Simplified electrochemical catalysis process in the case of direct four-electron pathway can be written as [46]:

$$M + O_2 \rightarrow M\text{-}(O_2)_{ads} \quad (2.23)$$

$$M\text{-}(O_2)_{ads} + 2e^- + 2H_2O \rightarrow M\text{-}(2OH)_{ads} + 2OH^- \quad (2.24)$$

$$M\text{-}(2OH)_{ads} + 2e^- \rightarrow M\text{-}(2OH^-)_{ads} \quad (2.25)$$

The charge distribution of a metal oxide surface is different than charge distribution of a metal surface [38], [46]. There is not full coordination between surface cations of stoichiometric oxides and oxygen. Therefore, full coordination of anion is achieved by the oxygen of H_2O in the medium. Therefore, the hydrogen atoms of H_2O disturb on the surface. Reduction of surface cation M occurs simultaneously to compensate charge because of the protonation of surface oxygen ligand, and OH^- is created. Then, M-OH^- species react with the adsorbed oxygen molecules that have end-on or side-on configurations. The proposed ORR pathways on the transition-metal oxide surfaces consist of the following reactions [38], [46]. One of the most commonly researched oxides for ORR is perovskites, the formula of it is ABO_3. Activities of them were ascribed to B site ion. Proposed pathways on the perovskite-type oxides can also be seen in Figure 2.14.

$$M^{m+}\text{–}O^{2-} + H_2O + e^- \rightarrow M^{(m-1)+}\text{–}OH^- + OH^- \quad (2.26)$$

$$O_2 + e^- \rightarrow (O_2^-)_{ads} \quad (2.27)$$

$$M^{(m-1)+}\text{–}OH^- + (O_2^-)_{ads} \rightarrow M^{m+}\text{–}O\text{–}O^{2-} + OH^- \quad (2.28)$$

$$M^{m+}\text{–}O\text{–}O^{2-} + H_2O + e^- \rightarrow M^{(m-1)+}\text{–}O\text{–}OH^- + OH^- \quad (2.29)$$

$$M^{(m-1)+}\text{–}O\text{–}OH^- + e^- \rightarrow M^{m+}\text{–}O^{2-} + OH^- \quad (2.30)$$

$$M^{m+}\text{–}O\text{–}O^{2-} + H_2O + e^- \rightarrow M^{(m-1)+}\text{–}OH^- + HO_2^- \quad (2.31)$$

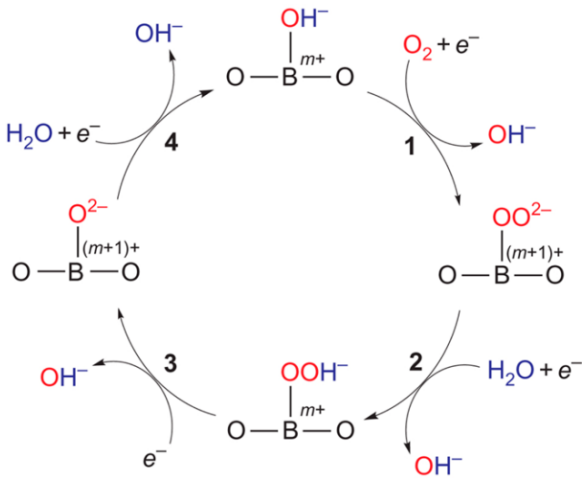

Figure 2.14 The ORR pathway on ABO_3 type oxides [38], [81].

The oxygen reduction reaction in the porous air electrode of the zinc-air battery consists of various steps as explained before such as; O_2(g) diffusion through the air electrode to the catalyst surface, oxygen adsorption and dissociation at the surface and electron transfer to the oxygen molecules, weakening and breaking of the oxygen bonds and desorption of hydroxyl ion. The reason for sluggish reaction kinetics is attributed to the strong O=O bond energy (498 kJ mol^{-1}), which is very difficult to break electrochemically. Therefore, using a catalyst is necessary to activate and cleave the bonds [38]. The oxygen reduction mechanism has not been understood clearly due to the difficulty in resolving surface reaction and rate-limiting steps in experiments.

Bifunctional catalyst is required for not only ORR but also OER at discharging and charging steps, respectively. The complex pathways are also involved in the OER. The OER in alkaline media can be written as:

$$4OH^- \rightarrow O_2 + 2H_2O + 4e^- \qquad (2.32)$$

The OER is rate limiting reaction because of sluggish kinetics which is ascribed to the breaking of O-H bonds and formation O=O bonds [82]. The complexity of oxygen evolution reaction intermediate steps (consisting of MO, MOH, MOOH, etc. intermediates) and lack of proper explanations to kinetics of each step prevented our knowledge of the OER steps as in ORR. The intermediate steps of OER may consist of water adsorption, hydroxide adsorption, O_2 evolution, catalyst degradation and dissolution of cation due to the lattice oxygen release [82]. One of the most prospective catalysts are oxides including surface reactions. The OER mechanism varies according to the participation of metal and/or lattice oxygen.

The OER generally takes place on the oxide phase rather than the metal surfaces. However, the mechanism depends on the materials and site geometry of the metal cation. Besides, the OER activity depends on the changeable valance state of metal ions. RuO_2 and IrO_2 are two important, typical oxygen evolution catalysts. Furthermore, nickel is also used as an OER catalyst in alkaline medium but lower conductivity phases involving Ni^{4+} are formed at high potentials that cause decreasing the battery performance. The transition metal oxide has been investigated for OER catalyst such as spinel $NiCo_2O_4$ [83].

Oxygen electrocatalysis is a hot topic in the industry due to the increasing demands for renewable energy technologies such as metal-air batteries, fuel cells, electrocatalytic and photocatalytic water splitting, etc as explained before. The ORR and OER activity of catalysts are important which drastically affect the battery performance. Precious metals are expensive and rare; thus, large-scale developments for industrial applications are limited. Finding an appropriate porous air electrode which accelerates ORR and OER reactions is essential. That can be achieved by formulating a suitable catalyst for ORR and/or OER. High catalytic activity, high electrical conductivity, high electrochemical stability, high chemical stability in alkaline electrolyte, high specific surface area, high porosity, favorite structure, favorite morphology, optimum composition and high catalytic stability are some requirements for a suitable catalyst. Researched catalysts for ORR and OER

reactions can be divided into subgroups depending on the type of the used material such as noble metals and alloys, carbonaceous materials and transition metal oxides.

2.4.1 Noble metals and alloys

The most effective catalyst for ORR is platinum in acidic and alkaline environments owing to its catalytic activity and stability. Therefore, platinum is generally selected as a benchmark material to compare the electrochemical activities. Platinum nanoparticles mixed with high surface area carbon. Commercially Pt (20 wt %)/Vulcan XC-72 carbon black powders are used as the catalyst material for ORR. The best ORR catalyst, Pt, is not; however, convenient to be used as OER catalyst. Indeed, surfaces of Pt particles were covered with an oxide layer at high electrode potentials. The experimental studies and modeling reveal that both direct and series four-electron pathways are observed on Pt nanoparticles during ORR. The direct four-electron pathway is generally observed at high potential intervals whereas the series 2 x 2 electron pathway is dominating at low potentials, intermediate of which is peroxide [46].

The high cost and scarceness of Pt shadow the further of the Pt/C catalyst. To overcome the problem and increase the usage of this type of catalyst, different strategies have been used. Tuning the size and morphology of particles to obtain fine-sized, textured particles have been reported as a good roadmap for improving electrocatalytic activity. Another strategy is to reduce the cost is obtaining core-shell structures. Generally, the core was composed of a less costly metal while the shell of it consisted of Pt [38]. Another strategy is to increase the activity with reducing cost is that alloying and/or modifying the Pt with suitable metals [46].

Experimental and computational studies reveal that there is a volcano relationship between the different catalysts. The adsorption energies of O and OH are good descriptors for ORR activity. The volcano plot of a series of different catalysts can be seen in Figure 2.15. This figure indicates that there should be a balance of oxygen

binding energy. Dissociative adsorption is rate-limiting when oxygen binding energy is low. On the other hand, desorption is rate-limiting when oxygen binding energy is so high. Moreover, researches were reported that not only oxygen binding energy but also adsorption energies of reactive intermediates and blocked species play an important role for activity. For example, there should be a balance of hydroxide binding energies to the surface for ORR because that is a product which should be released from the surface [84].

The alloying of Pt with appropriate noble metals is an applicable technique to enhance the electrochemical activity of catalysts and decrease the cost. Volcano plot is taken into account when appropriate noble metals are selected for designing suitable alloy. For example, A is selected from one side and B is selected from the other side of the volcano plot in order to design alloy AB.

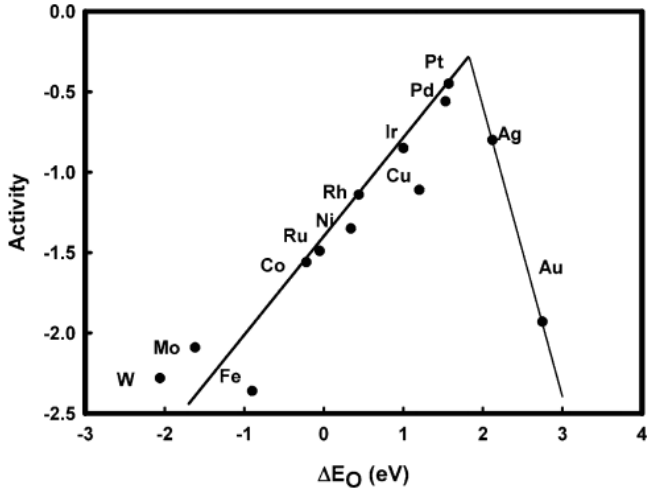

Figure 2.15 Graph of oxygen reduction activity versus oxygen binding energy [84].

Other metals used as a catalyst may be written as gold, palladium and silver. Whereas gold in bulk form is inert, however, nanostructured gold exhibits good electrocatalytic activity [38], [59]. Graphene supported gold particles show good catalytic activity for ORR. It was reported that ORR could occur on the gold surface

with 2 x 2 e pathway or a direct 4 e pathway. Alloying gold with less costly metals is an approach. Indeed, the effect of alloying of Ag and Au was investigated by volcano plot. The best activity was observed at 36 at % Au composition for 3-5 nm particles in size.

Palladium is one of the active materials in alkaline electrolyte. RDE test was conducted and results highlight the high electrocatalytic activity of Pd in alkaline electrolyte [38]. A core-shell structure of Ag or Au/Pd with carbon support was also reported as a promising catalyst.

Finding a cost-effective catalyst rather than Pt, Au and Pd metals have gained interest recently. Ag can be considered as a promising catalyst due to a similar reaction mechanism and ORR kinetics compared to Pt benchmark [38]. ORR reaction pathway on surfaces of Ag single crystals and nanoparticles was reported as pseudo 4 electrons. While ORR occurred by the 2 x 2 electron pathway on small Ag particles, 4 electron pathway was observed on large Ag nanoparticles (174 nm). Silver is also a promising catalyst due to good HO_2^- elimination. The 2 electron pathway on the silver was attributed to the highly defective structure because of the stronger adsorption of OH^- ions. There should be a balance between two opposite effects: OH- adsorption and activation energy, which was achieved for (110) surface of Ag; therefore, kinetics at Ag(110) surface is faster than the other facets. The best combination and loading amount of Ag on carbon support are still under debate. Ag was reported to exceed the catalytic activity performance of Pt catalysts in high alkaline concentration; however, onset potential and half-wave potential of Ag/carbons are commonly 50-100 mV lower than the commercial Pt/C catalyst [38].

2.4.2 Carbonaceous materials

High surface area carbon-based nanoparticles have been investigated due to their stability, low price, abundance, good wetting and electrical characteristics [46]. Especially the treatment of carbon surface such as doping with heteroatoms has been

extensively investigated because of enhancing their ORR activity. Heteroatoms (such as S, P and N) increases the structural disorder of carbon. The ORR activity of N-doped carbon powders consisting of carbon black, graphene, nanofibers and nanotubes were reported. Doping of N enhances the amount of defectiveness and edge plane sites [46]. Besides, materials consisted of M, N and C (metal, nitrogen and carbon) have been investigated and their activity was ascribed to the metal cation coordination by nitrogen [18].

2.4.3 Transition metal oxides

Numerous types of oxides in different forms of spinel, delafossite, perovskite, etc. have been searched [46]. Manganese oxide (MnO_x) is a promising catalyst candidate among them and they are investigated deeply because of the variety of oxidation states, chemical compositions and crystal structures. Indeed, MnO_2 is the most commonly used ORR catalyst in commercial Zn-air batteries. Depending on the crystallography of this oxide activity in ORR range changes drastically. The activities of oxides can be written in the following order of γ- < β- < α-MnO_2 [46]. The size of the tunnel structure between the [MnO_6] octahedrons, electrical conductivity and morphology are some significant parameters that determine the activity in ORR rage. Even though α-MnO_2 particles were reported as good catalysts, different activities were observed depending on the size of the synthesized particles. For example, α-MnO_2 nanoparticles showed better performance than micro-sized counterparts. Moreover, combining the α-MnO_2 with another catalytic material (such as Ag), and doping seems to be a beneficial method to improve the ORR activity according to the researchers.

Co_3O_4 is also a well-known catalyst [42] especially for its OER activity while it displays low activity in ORR range. The activity of Co_3O_4 faces were reported as (111) > (100) > (110) [38]. The difference in the activity was attributed to the surface Co^{2+} density of the facets. Moreover, formation of Co_3O_4 directly on the current collector (mesh) increased the performance of the zinc-air battery [76]. Different

binary and ternary spinel oxides including Co have also been researched such as $NiCo_2O_4$, $Cu_xCo_{3-x}O_4$ and $Co_xMn_{3-x}O_4$ [38].

The other most researched type of oxides is called as perovskite oxide. They have been getting attention especially for ORR activity in alkaline electrolytes. The basic formula of perovskites is given by ABO_3. High oxygen coverage on the surfaces of perovskite oxide is an important characteristic of these oxides. Thus, adsorption and desorption of oxygen in a reversible way were reported. The B-site cations were most widely changed to activity tunning while the effect of change of A-site cation has a minor role [81].

The ORR activity of La-based perovskites can be improved by changing the B-site cation as can be seen in Figure 2.16 that depend on the ability of these cations to obtain redox couples in the ORR range. As can be seen in Figure 2.16, activity trends increases in the following order: Cr < Fe < Ni < Mn < Co [85].

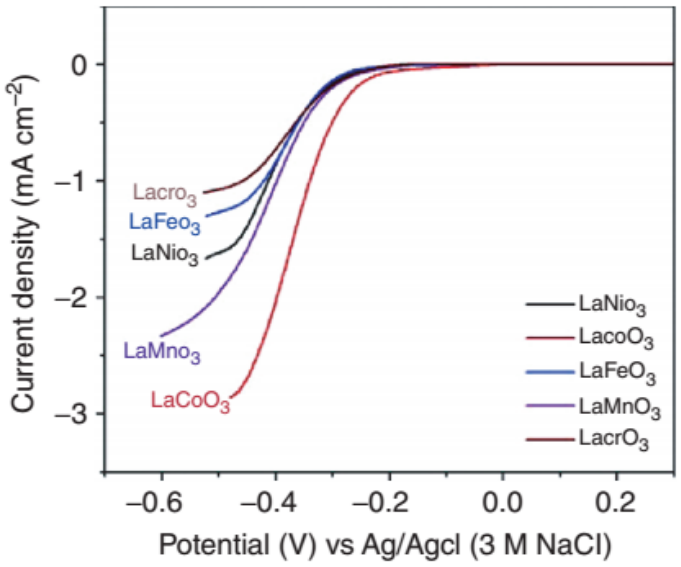

Figure 2.16 RDE test for $LaMO_3$ peroxides (M= Ni, Co, Fe, Mn, Cr) performed at 1600 rpm with a scan rate of 20 mV/s [85].

CHAPTER 3

EXPERIMENTAL PROCEDURE

3.1 Materials

All chemicals used in this work were of analytical reagent grade and were used as received. In this study, catalytic activities of produced Ag-based oxides were compared with commercial Pt/C and Pt-Ru catalysts (Taken from TEKSIS, Inc.; Turkey). The following chemicals were used in this thesis: manganese(II) sulfate monohydrate ($MnSO_4.H_2O$, Merck), potassium persulfate ($K_2S_2O_8$, Sigma Aldrich), sulfuric Acid (H_2SO_4, Merck, 98 weight %), silver nitrate ($AgNO_3$, Merck), chromium(III) nitrate nonahydrate ($Cr(NO_3)_3.\ 9H_2O$, Sigma Aldrich), cetyltrimethylammonium bromide (CTAB, Sigma Aldrich), sodium dodecyl sulfate (SDS, Sigma Aldrich), ammonium chromate ($(NH_4)_2CrO_4$, Sigma Aldrich), ammonia solution (NH_4OH solution, Merck, 25 weight %), ammonium molybdate ($(NH_4)_6Mo_7O_{24}.4H_2O$, Merck), sodium hydroxide (NaOH, Merck), ammonium metatungstate ($(NH_4)_6W_{12}O_{39}$, Alfa Aesar), 5 wt% Nafion solution (LIQUionTM), carbon black (Printex L6, Degussa), copper(II) nitrate hemi(pentahydrate) ($Cu(NO_3)_2.\ 2.5H_2O$, Sigma Aldrich), manganese (II) nitrate tetrahydrate and hydrogen peroxide ($Mn(NO_3)_2.4H_2O$, Merck), hydrogen peroxide (H_2O_2, Merck, 30 weight %), cobalt(II) nitrate hexahydrate ($Co(NO_3)_2.\ 6H_2O$, Sigma-Aldrich), ammonium chromate ($(NH_4)_2CrO_4$, Sigma Aldrich), citric acid ($HOC(COOH)(CH_2COOH)_2$, Sigma Aldrich) and ethylene glycol ($HOCH_2CH_2OH$, Alfa Aesar, 99 weight %).

3.2 Synthesis of Materials

3.2.1 Synthesis of Mn-Based Oxides, α-MnO_2, Mn_2O_3 and Mn_5O_8

3.2.1.1 Synthesis of α-MnO_2

The various production methods for α-MnO_2 synthesis can be found elsewhere [86]. In this study, the precipitation and hydrothermal methods were used. An aqueous solution, composed of $MnSO_4.H_2O$, $K_2S_2O_8$ and H_2SO_4, was put into a beaker. The synthesis was conducted at 80 ^oC for 20 hours. The concentrations of $MnSO_4.H_2O$ and $K_2S_2O_8$ were the same (0.05 M). The pH of the solution was adjusted to 1 by using a diluted solution of H_2SO_4. Same ingredients were used at hydrothermal method. The 1400 ml of solution mixture was hold at 120 ^oC for 12 hours.

3.2.2 Synthesis of Mn_2O_3 and Mn_5O_8

The Mn_2O_3 and Mn_5O_8 powders were synthesized through spray pyrolysis. The cathode materials were synthesized by using aqueous solutions of $Mn(NO_3)_2.4H_2O$ and H_2O_2. The different amounts of manganese source (Spray-1 and 2: 0.05 mole) and hydrogen peroxide (Spray-1: 0, Spray-2: 12.5 ml) were added in to the water (total volume is 100 ml). Production system were combined of a droplet generator, reactor and electrostatic precipitator for powder collection. Ultrasonic nebulizator was used as droplet generator. Then, these were carried through the 7 cm diameter quartz tube by oxygen gas. The temperature of the reactor and the flow rate were kept at 500 ^oC and 4 l/min, respectively.

3.2.3 Synthesis of Ag-Based Oxides, Ag_2XO_4 (X=Cr, Mo, W)

3.2.3.1 Synthesis of Ag_2CrO_4

For the synthesis of Ag_2CrO_4, 1.68 g of $AgNO_3$ was dissolved in 100 ml of deionized, distilled water with shaking. 0.08 g of cetyltrimethylammonium bromide (CTAB) and 0.048 g of sodium dodecyl sulfate (SDS) were dissolved in 100 and 60 ml of deionized water separately. Then these solutions were mixed dropwise to the above mixture. The solution of chromium was prepared by dissolving 0.76 g of $(NH_4)_2CrO_4$ in 180 ml of deionized water. 0.15 ml of 25 % NH_3 solution was added to the 20 ml of deionized water. The silver solution was added slowly to the chromium solution and the final pH of the solution was measured as 6.33. Reddish precipitates were filtered after repeated deionized water and ethanol rinse. Then collected products were annealed in a furnace at 80 ^oC for 10 h.

3.2.3.2 Synthesis of Ag_2MoO_4

For the synthesis of Ag_2MoO_4, 1.68 g of $AgNO_3$ was dissolved in 300 ml of deionized water. The solution of molybdenum was prepared by dissolving 1.00 g of $(NH_4)_6Mo_7O_{24}.4H_2O$ in 100 ml of deionized water. The molybdenum solution was added slowly to the silver solution and deionized water addition was made until the volume was completed to 1400 ml. The pH of the solution was adjusted to 7 by 1 M NaOH solution. The mixture was put into a 2000 ml PTFE lined stainless steel autoclave and held at 140 ^oC for 12 h. Then filtered particles were annealed in the furnace at 80 ^oC for 10 h.

3.2.3.3 Synthesis of Ag_2WO_4

For the synthesis of Ag_2WO_4, 1.68 g of $AgNO_3$ was dissolved in 300 ml of deionized water. The solution of tungsten was prepared by dissolving 1.47 g of $(NH_4)_6W_{12}O_{39}$

in 300 ml of deionized water. The tungsten solution was added slowly to the silver solution and deionized water addition was made until the volume was completed to 1400 ml. The pH of the solution was adjusted to 9 by 1 M NaOH solution. The mixture was then put into a 2000 ml PTFE lined stainless steel autoclave and held at 140 ^{o}C for 12 h. Then filtered particles were annealed in the furnace at 80 ^{o}C for 10 h.

3.2.4 Synthesis of Cu-based Delafossites, $CuCrO_2$ and $CuCoO_2$

3.2.4.1 Synthesis of $CuCoO_2$

Low-temperature production by the hydrothermal method was taken as an example for this study [87], where concentrations of ingredients were changed. For the synthesis of $CuCoO_2$, 6.984 g of $Cu(NO_3)_2$. $2.5H_2O$ was dissolved in 500 ml of distilled water with shaking. 8.7309 g of $Co(NO_3)_2$. $6H_2O$ and 90 g of NaOH were dissolved in 500 ml of deionized water separately. The cobalt solution was added dropwise to the copper solution. NaOH was used as a mineralizer. Then the NaOH solution was mixed slowly with the above mixture. Then, the final pH of the solution was measured as 13.3. The mixture was put into a 2000 ml PTFE lined stainless steel autoclave and held at 100 ^{o}C for 24 h. Then collected products were annealed in a furnace at 80 ^{o}C for 10 h.

3.2.4.2 Synthesis of $CuCrO_2$

For the synthesis of $CuCrO_2$, hydrothermal and sol-gel methods were used. To synthesize $CuCrO_2$ powders by hydrothermal method, 6.98 g of $Cu(NO_3)_2$. $2.5H_2O$ was dissolved in 500 ml of distilled water with shaking. 12 g of $Cr(NO_3)_3$. $9H_2O$ and 120 g of NaOH were dissolved in 500 ml of deionized water separately. The chrome solution was added dropwise to the copper solution. NaOH was used as a mineralizer. Then the NaOH solution was mixed slowly with the above mixture.

Then, the final pH of the solution was measured as 13.4. The mixture was put into a 2000 ml PTFE lined stainless steel autoclave and held at 210 ^{o}C for 60 h. Moreover, hydrothermally produced $CuCrO_2$ powders were also provided from H. Akyıldız. Preparation of $CuCrO_2$ powders was conducted at 230 ^{o}C for 60 h. Details of the experimental procedure can be found in the literature [88]. The powders obtained at 210 and 230 ^{o}C are called $CuCrO_2$-H210 and $CuCrO_2$-H230, respectively to describe these experiments hereinafter.

To synthesize $CuCrO_2$ powders with the sol-gel method, $Cu(NO_3)_3$. $2.5H_2O$ and $(NH_4)_2CrO_4$ were used as copper and chrome source. Firstly, 0.015 mol ascorbic acid and 0.015 mol $(NH_4)_2CrO_4$ were dissolved in 30 and 10 ml hot deionized water, respectively. The latter one was slowly added to the ascorbic acid solution and a dark green mixture was obtained. Then, 0.015 mol citric acid was added to the above mixture. The copper solution was obtained by dissolving 0.015 mol $Cu(NO_3)_3$. $2.5H_2O$ and 0.015 mol citric acid. Then the copper solution and chrome solution were mixed. Extra addition of 0,03 mol citric acid and 2.5 ml ethylene glycol was finally added to the whole mixture. The concentration of citric acid was two times higher than that of metal sources. The mixture was put into a glass beaker and held at 100 ^{o}C until the water was removed and gelation was formed. Then powder was calcined in air at 400 ^{o}C for 2 h. Then, the temperature of the powder was increased to 1000 ^{o}C at a heating rate of 5 ^{o}C min-1 and hold for 10 h. This experiment is called as $CuCrO_2$ sol-gel hereinafter.

3.3 Characterization Methods

3.3.1 Structural Characterization

Microstructural analyses of produced powders were performed by scanning electron microscope, FEI Nova NanoSEM 430. Bruker D8 Advance X-ray Diffractometer was used to perform X-ray diffraction analyses. The radiation of Cu Kα (wavelength of 0.154183 nm) was used as the X-ray source. To investigate surface analysis, BET

analysis was performed by Autosorb 6B instrument with nitrogen adsorption-desorption isotherms. The outgassing of $CuCoO_2$ was performed at 200 °C for 2 h, the others were hold at 80 °C for 12 h before the BET analysis.

3.3.2 Electrochemical Tests

Rotating Disk Electrode Voltammetry (RDE): The RDE was performed to evaluate the ORR and OER activity of synthesized powders. RDE technique consists of working, counter and reference electrodes in three-electrode configuration. The schematic figure of working electrode used in RDE experiments can be seen in Figure 3.1(a). Catalysts were loaded on glassy carbon side and disk electrode was rotated while the current is recorded. A typical ORR polarization curve can also be seen in Figure 3.1(b). The onset potential (E_{onset}), half-wave potential ($E_{1/2}$), overpotential at specific current density ($\eta_{i,}$ j_{ORR} = -3 mA cm^{-2} and j_{OER} = +10 mA cm^{-2}) and diffusion-limited current density (i_L) which can be seen in Figure 3.1(b) were used as figure of merits. These indicators for each catalyst will be investigated and compared with the others especially the Pt/C benchmark. A similar graph can be obtained three-electrode cell without rotation. However, additional information is obtained from RDE experiments because the hydrodynamic and electrochemical properties of RDE is associated with the Koutecky-Levich (K-L) equation and electron transfer number can be found after recording the voltammograms at different rotation rates.

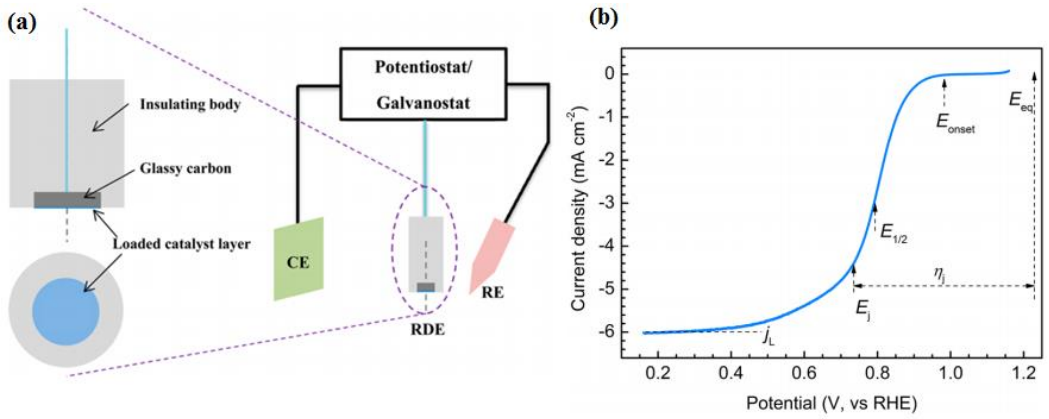

Figure 3.1 (a) Schematic figure of RDE setup in half-cell test, (b) a typical linear sweep voltammogram recorded in ORR rage form RDE experiments [38].

After structural characterization, these materials were tested in a three-electrode half-cell. A catalyst ink coated glassy carbon electrode (5mm diameter ,0.196 cm^2) and a graphite rod was used as working and counter electrodes, respectively. The surface area of counter electrode, graphite, was much greater than that of glass carbon working electrode. The setup of the RDE experiments can be seen in Figure 3.2.

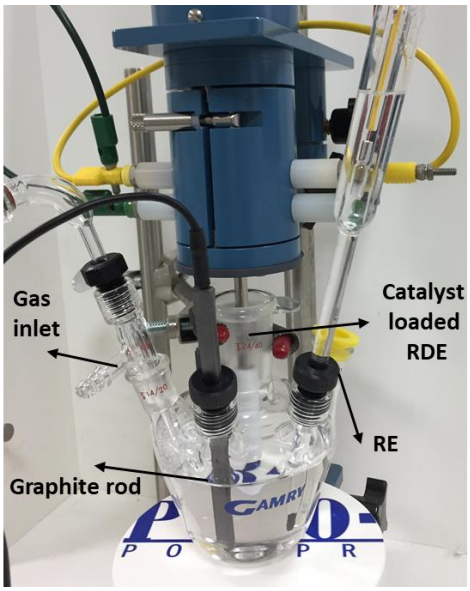

Figure 3.2 Setup of RDE experiments.

Catalyst Ink Preparation: To prepare catalyst ink, 50 mg of synthesized powders, 10 mg of carbon black (Printex L6, Degussa) carbon support and 200 µl of 5 wt% Nafion solution (LIQUionTM) were mixed in the mixture of 2 ml isopropanol alcohol and 8 ml deionized water. The aim of the mixing of synthesized powders with carbon support at a 5:1 mass ratio is to increase the electronic conductivity in the working electrode to decrease the negative effect of low conductivity of oxides. Effect of Printex L6 addition on OER activity was recorded in the literature, which revealed that there was no remarkable change in the OER kinetics [89]. Moreover, voltammograms were recorded with carbon black and combination of both oxides and carbon black to see the effect on ORR behavior. The final concentration of ingredient in ink was 5 mg_{active} /ml_{ink}, 1 mg_{carbon} /ml_{ink}, 1 mg_{nafion} /ml_{ink}. The catalyst ink was sonicated in an ice bath placed in the ultrasonicator for 30 minutes to homogenize the solution before the ink was applied to the glassy carbon. Then, 10 µl of the ink was dropped on the glassy carbon electrode, then it was spin-coated at 700 rpm with the help of an inverted rotation disk electrode setup. The amount of catalyst loading was adjusted to obtain a homogenous ink layer, which was most widely used catalyst loading amount to compare activity of catalyst in RDE experiments [90]. Moreover, ratio of nafion to catalyst (N/C) was selected according to the literature. Li et al. [91] were investigated the effect of this ratio for OER activity. They reported that uniform dispersion of nafion on the surface of catalyst was observed until the N/C=1/2. The N/C ratio was selected as 1/5 for our study according to literature research and uniformity of catalyst layer.

After catalyst ink was dried naturally and the electrodes were immersed in 0.1 M KOH aqueous electrolyte which was purged with N_2 to record the background current. Then, the electrolyte is purged with O_2 gas before the experiment (about 30 minutes) for conditioning and activity measurements, respectively. A constant flow of oxygen gas flow was maintained during the experiment. The conditioning of the working electrode surfaces before ORR measurements was done by cyclic voltammograms, which were recorded between 0.1 to – 1.2 V vs. Hg/HgO reference electrode with a scan rate of 500 mV s^{-1} for 40 cycles. The conditioning of the

working electrode surfaces before OER measurements was done by cyclic voltammograms, which were recorded between 0.3 to 0.6 V vs. Hg/HgO reference electrode with a scan rate of 500 mV s^{-1} for 40 cycles.

To evaluate the oxygen reduction reaction activities of different produced powders, rotating disc electrode experiments (RDE- Pine Instruments) were performed in the O_2 saturated 0.1 M KOH aqueous electrolyte. The potential difference between the working electrode and the reference electrode was swept from 1 to -1 V (Hg/HgO/1 M KOH) at a scan of 5 mV/s. To compare oxides, rotation speed and mass loading of catalysts were held constant at 1600 rpm and 0.25 mg_{oxide} cm^{-2}, respectively. The working electrode speed was generally adjusted to 1600 rpm in the literature, which facilitates reactant transport and product removal [92]. Moreover, RDE voltammograms were recorded at different rotation rates (100, 400, 900, 1600 rpm) for the same material. Slopes of 1/j versus $\omega^{-1/2}$ graphs at different potentials were calculated to find an electron transfer number by the Koutecky-Levich equation. Slopes of 1/j versus $\omega^{-1/2}$ graphs at different voltages were calculated to find an electron transfer number by the Koutecky-Levich equation that can be written as [27]:

$$\frac{1}{j} = \frac{1}{jk} + \frac{1}{jL} \tag{3.1}$$

$$\frac{1}{jL} = \frac{1}{B\omega^{0.5}} \tag{3.2}$$

$$B = 0.62\, n\, F\, Co\, Do^{2/3}\, v^{-1/6} \tag{3.3}$$

Where j is the measured current density, jL and jk are the diffusion- and kinetic-limiting current densities, ω is the rpm angular frequency of rotation in units of rad s^{-1}, F is the Faraday constant (96 485 C/mol), n is transferred electron number, Co is the bulk concentration of O_2 in 0.1 M KOH electrolyte (1.2 x 10^{-6} mol cm^{-3}), ν is the kinematic viscosity of 0.1 M KOH electrolyte (0.01cm^2 s^{-1}) and Do is the diffusion

coefficient of O_2 in 0.1 M KOH (1.9×10^{-5} cm^2 s^{-1}). n values were obtained from the slope of j^{-1} versus $\omega^{-1/2}$ graph. Details of K-L and Tafel plots can be found elsewhere [27].

All RDE voltammograms were recorded with respect to a reference electrode (Hg/HgO/1 M KOH; Hach-Lange Ltd. XR400) at room temperature. The Hg/HgO reference electrodes with different concentrations of NaOH and KOH filling solutions are preferred to the other reference electrodes in alkaline electrolytes [93]. The recorded potentials with respect to the reference electrode were converted to the reversible hydrogen electrode potential (RHE) was done by Equation (3.4) [94]. The potentials were generally reported with respect to RHE in the literature. As can be seen in Figure 3.3, the equilibrium potential of oxygen evolution reaction in alkaline medium is 1.23 V vs. RHE. The overpotentials (η) of ORR and OER are calculated by Equation (3.6) and (3.7), respectively. The ORR/OER potential with respect to RHE does not change with the pH of the electrolyte. However, its potential with respect to other reference electrode types depends on the pH of the medium. In this study, all potential values given have been converted into RHE.

$$E_{RHE} = E_{Hg/HgO} + E^{o}_{Hg/HgO} + (0.059 \times pH), \quad (3.4)$$

Where $E^{o}_{Hg/HgO/1M\ KOH} = 0.098$ V

$$O_2 + 2H_2O + 4e^- \rightarrow 4OH^- \ (E^o = 1.229 \text{ V vs RHE}) \quad (3.5)$$

$$\eta = 1.23 - E_{RHE} \text{ V} \quad (3.6)$$

$$\eta = E_{RHE} - 1.23 \text{ V} \quad (3.7)$$

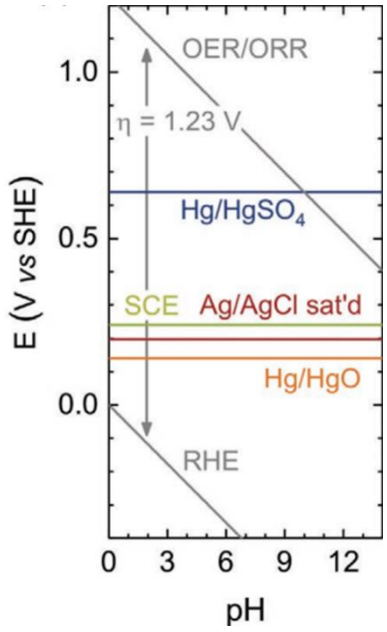

Figure 3.3 The Pourbaix diagram of water with showing potentials of commonly used reference electrodes [93].

To evaluate the oxygen evolution reaction activities of different produced powders, rotating disc electrode experiments (RDE- Pine Instruments) were performed in the O_2 saturated 0.1 M KOH aqueous electrolyte. The potential difference between the working electrode and the reference electrode was swept from 0 to 1.2 V (vs. Hg/HgO/0.1 M) at a scan of 5 mV/s. The rotation speed and mass loading of catalysts were held constant at 1600 rpm and 0.25 mg_{oxide} cm^2, respectively. The rotation was held at 1600 rpm to remove the product O_2(g), adsorption of this blocks the active sites.

The commercial 67wt% Pt/C catalyst ink solution containing Nafion, isopropanol alcohol and deionized water was purchased from TEKSIS, Inc. (Ankara, Turkey). The 10 µl of the ink was dropped on the glassy carbon electrode with approximately 0.23 $mg_{Pt/C}$ cm^{-2} mass loading, then it was spin-coated at 700 rpm with the help of an inverted rotation disk electrode setup. Mass and geometric area normalized current densities of this commercial catalyst was compared with the others.

Briefly, linear sweep voltammograms recorded during the RDE were made to evaluate the oxygen reaction activities of catalyst by comparing mass and geometric area normalized current densities, electron transfer numbers, Tafel slopes, onset potentials, half-wave potentials, overpotentials at a specific current density (-3 mA cm^{-2} for ORR and 10 mA cm^{-2} for OER).

Electrochemical impedance spectroscopy (EIS) studies: EIS studies were carried out using a VMP-300 potentiostat (Biologic Science Instruments) in a three-electrode configuration of catalyst coated glassy carbon disk working electrode, graphite as counter electrode and Hg/HgO as the reference electrode. Prior to impedance measurements, ORR catalyst candidate samples were preconditioned by applying 30 cycles of CV between 0.965 V and -0.135 V versus RHE under constant oxygen purging of the 0.1 M KOH electrolyte. Impedance spectra were recorded while the electrolyte was purged with oxygen and the working electrode disk was rotating at 1600 rpm. The amplitude of the AC signal was 10 mV rms and the frequency was swept from 20 kHz to 20 mHz. All data were collected in a single sine mode at the mixed diffusion controlled region at two different working electrode potential levels, E_{WE}, specifically at 0.765 V and 0.7 V versus RHE. The redox reaction was more kinetically controlled (electron transfer) at 0.765 V and more mass transport controlled at 0.7 V. All spectra were fitted to corresponding equivalent circuit models using EC-Lab software of Biologic.

Prior to impedance measurements, OER catalyst candidate samples were preconditioned by applying 30 cycles of CV between 1.165 V and 1.465 V versus RHE with a scan rate of 500 mV s^{-1} for 40 cycles under constant oxygen purging of the 0.1 M KOH electrolyte. Impedance spectra were recorded while the electrolyte was purged with oxygen and the working electrode disk was rotating at 1600 rpm. All data were collected in a single sine mode at 1.7 V RHE working electrode potential level. All spectra were fitted to corresponding equivalent circuit models using EC-Lab software of Biologic.

Stability tests: To investigate the stability of the promising ORR catalyst candidate, chronoamperometry was conducted at 0.7 V RHE for 20000 seconds. Moreover, the accelerated durability test (ADT) was conducted by cyclic between 0.6 to 1 V RHE for 2000 cycles with a scan rate of 100 mV s^{-1}. Linear sweep voltammograms were recorded before and after the ADT in O_2 saturated 0.1 M KOH.

To investigate the stability of the promising OER catalyst candidate, chronoamperometry was conducted at 1.7 V RHE. Linear sweep voltammograms were recorded before and after the chronoamperometry test in O_2 saturated 0.1 M KOH.

LSV on Air electrode: Air electrodes were also prepared to be used in the half-cell tests. Oxides were mixed with carbon black. The final concentration of ink was 10 mg_{active} /ml_{ink}, 2 mg_{carbon} /ml_{ink}, 67 μl_{nafion} /ml_{ink}. Powders were mixed in 10 ml of isopropanol alcohol, which was followed by sonication for 30 minutes in an ice bath. Then, the solution was sprayed onto the gas diffusion layer by airbrush then dried in an oven at 60 ^oC for 24 hours. The amount of the loading was adjusted by weighing of carbon paper before and after spray coating to compare results with the commercially taken Pt/C, Pt-Ru loaded gas diffusion layers (1 mg_{Pt} cm^{-2} and 1 mg_{Ru} cm^{-2}, taken from Full cell store). Catalyst ink sprayed onto a carbon paper (Sigracet gas diffusion layer-GDL 34 AA) was used as an electrode. The catalyst-loaded GDL, graphite rod and the reference electrode (Hg/HgO/ 1M KOH) were immersed in 0.1 and/or 6 M KOH aqueous electrolyte and linear sweep voltammograms were recorded in a homemade setup (See Figure 3.4).

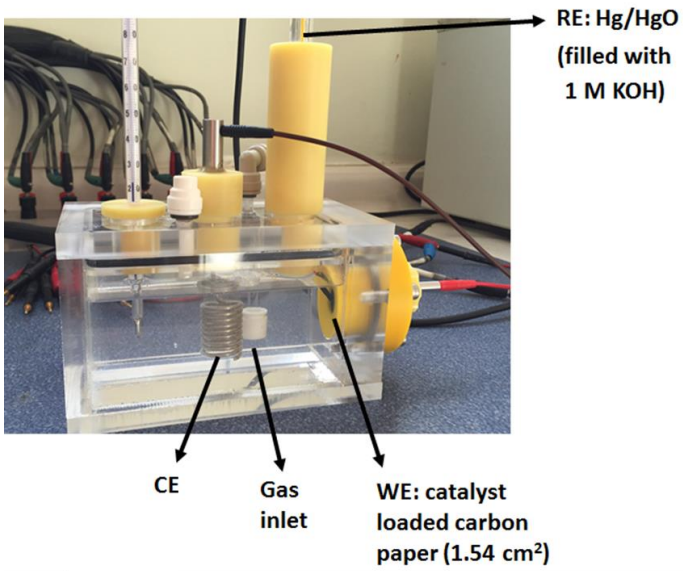

Figure 3.4 Three-electrode electrochemical cell for testing electrocatalytic activity of catalysts.

Homemade zinc-air cell test:

The catalyst ink sprayed on GDL (Sigracet, 34 BC) consisted of 50 mg active material, 10 mg carbon black and 350 µl 5 wt. % Nafion solution. These were mixed in 5 ml isopropanol alcohol, which was followed by sonication for 30 minutes in an ice bath. Then, the solution was sprayed onto the gas diffusion layer by airbrush then dried in air. The amount of the loading was adjusted to 1 mg cm^{-2} by weighing of carbon paper before and after spray coating. Catalyst loaded GDL was used as the air electrode. Moreover, a metal mesh was used as a current collector at the air sides of the battery. The designed zinc-air cell can be seen in Figure 3.5. A polished, smooth zinc plate was used as the anode. Firstly, the zinc plate was cleaned with acetone and isopropyl alcohol, respectively. Then, it was treated with 0.5 M HCl solution. Besides, a highly alkaline aqueous solution (6 M KOH) was used as the electrolyte. The synthesized powders were loaded on the air electrode and battery tests were conducted at this setup.

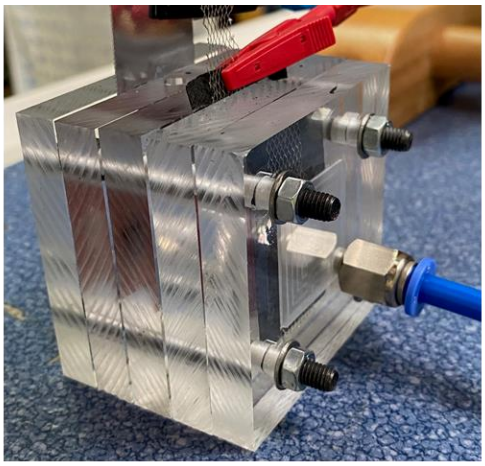

Figure 3.5 Designed Zinc-air cell.

CHAPTER 4

RESULTS AND DISCUSSION

The activities of Mn-based, Ag-based and Cu-based oxides were investigated in terms of ORR and OER activity. While all of them were investigated for both reactions, the promising catalysts candidates have been investigated in detail. Firstly, structural characterizations were performed by SEM and XRD prior to use of synthesized powders. Then, linear sweep voltammograms of catalysts loaded rotating disk electrode and gas diffusion layer were investigated via a three-electrode cell in 0.1 M and/or 6 M KOH electrolyte, respectively. The onset and half-wave potentials, electron transfer number, Tafel slope, limiting current density, overpotential at -3 mA cm^{-2} current density for ORR and overpotential at 10 mA cm^{-2} current density for OER were studied. The stability of powders was verified by chronoamperometry and accelerated durability tests.

4.1 Results of Mn-based Oxides, α-MnO_2, Mn_2O_3 and Mn_5O_8

XRD spectra of α-MnO_2 powders synthesized by precipitation and hydrothermal methods can be seen in Figure 4.1(a). The same XRD data were obtained from two methods. The desired alpha phase was obtained by hydrothermal and precipitation methods. The XRD spectra with Rietveld fitting of precipitated α-MnO_2 powder can be seen in (Figure 4.1(b)). The XRD spectra of powders showed diffraction peaks, which correspond to a pure tetragonal phase of α-MnO_2 (ICSD 73363) and no other impurities were found. Besides, SEM images of these powders can be seen in Figure 4.2. SEM images indicated that needle-like α-MnO_2 microstructures in the nanometer range were obtained by precipitation method. The urchin-like microstructure was also observed at hydrothermally produced powders; however,

size of the needles was larger. The formation of α-MnO_2 was explained by the following chemical reaction Equation (4.1), which is a redox reaction between Mn^{+2} and $S_2O_8^{2-}$ ions: The ΔG^o of the total reaction is -151000 J/mol that indicates the strong tendency for α-MnO_2 formation. However, nano-sized powders were obtained after 20 hours at 80 ^oC. The slow reaction was linked to the characteristics of reaction kinetics. The formation of urchin-like α-MnO_2 structures was explained in the literature [95].

$$Mn^{2+} + S_2O_8^{2-} + 2H_2O \rightleftharpoons MnO_2 + 4H^+ + 2SO_4^{2-} \quad (4.1)$$

Particle morphology, size and purity are important properties that affect electrochemical performance. The electrochemical activities of metal oxides can be altered with their method of preparation. In the reported researches, the highest activities were generally achieved with nanoparticles having the highest surface area [96]. Therefore, α-MnO_2 powder obtained by precipitation technique was further analyzed in this study.

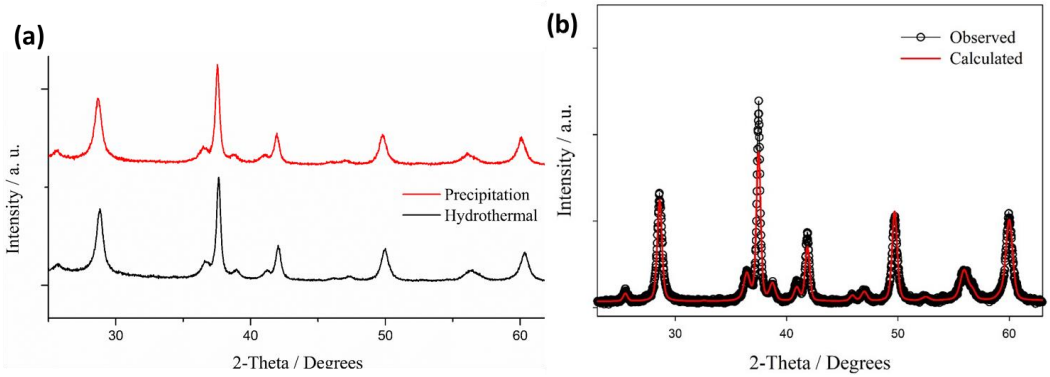

Figure 4.1(a) The XRD spectra of α-MnO_2 powders synthesized by precipitation and hydrothermal methods (b) The XRD spectra and results of Rietveld refinement of precipitated α-MnO_2 powders (ICSD 73363).

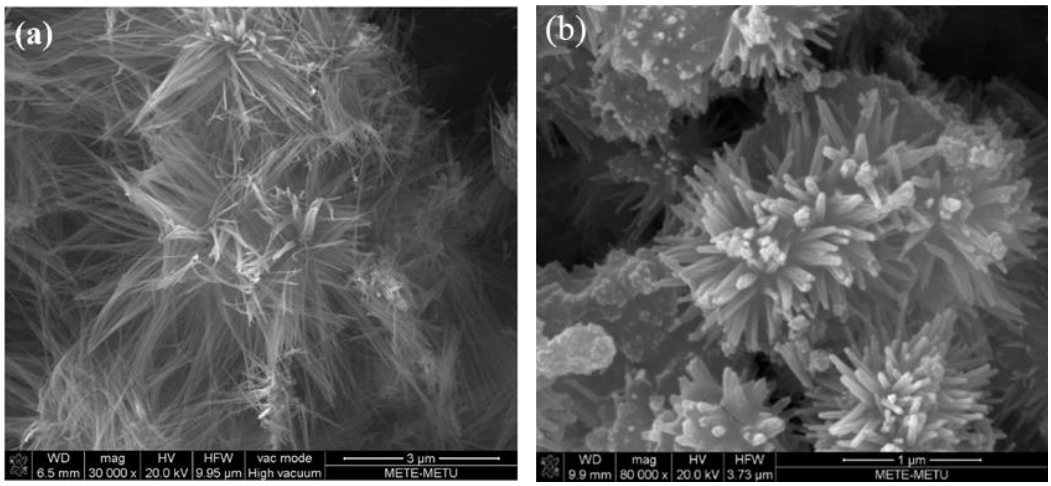

Figure 4.2 SEM images of α-MnO_2 powders synthesized through (a) precipitation and (b) hydrothermal methods.

XRD spectra and results of Rietveld refinement of Mn_5O_8 and Mn_2O_3 powders can be seen in Figure 4.3(a, b). Peak positions of the powder obtained at first spray pyrolysis experiment coincide with the peak position of the monolithic Mn_5O_8 phase (Card number: 1514100). However, impurities, orthorhombic Mn_2O_3 (Card number: 1514103) phase was found in small amounts (approximately 7 wt. %). The percentage of R_{wp} was found as 10 by Rietveld fitting carried out with MAUD software [97]. Peak positions of the powder obtained at the second spray experiment showing a good agreement with the orthorhombic Mn_2O_3 but monolithic Mn_5O_8 phase were found in a small amount (approximately 3 wt. %) the percentage of R_{wp} of the sample was found as 11 by refinement (See Figure 4.3(b)).

Production of fine-sized Mn_5O_8 and Mn_2O_3 powders is aimed in this research. The effect of surface area, morphology and crystal structures of powders on electrocatalytic activity is enormous. Indeed, the shape and size of synthesized particles can easily be controlled by spray pyrolysis; thus, this method was chosen to synthesize spherical particles with smaller particle sizes. The microstructure of powders synthesized by spray pyrolysis can be seen in Figure 4.4. The synthesized

Mn_5O_8 and Mn_2O_3 powders were composed of spherical aggregates of submicron-sized particles. It can also be seen that some of the round aggregates were empty.

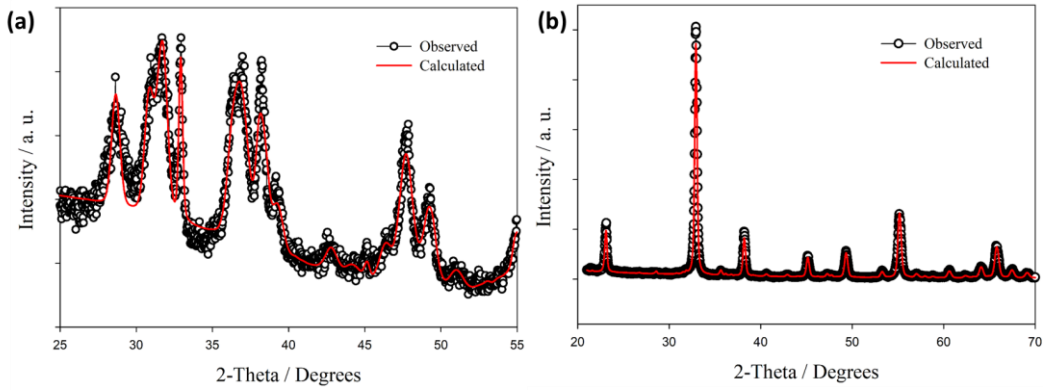

Figure 4.3 The XRD spectra and results of Rietveld refinement of (a) Mn_5O_8 powders obtained at 1st spray experiment (Card number: 1514100) and (b) Mn_2O_3 powders obtained at 2nd spray experiment (Card number: 1514103).

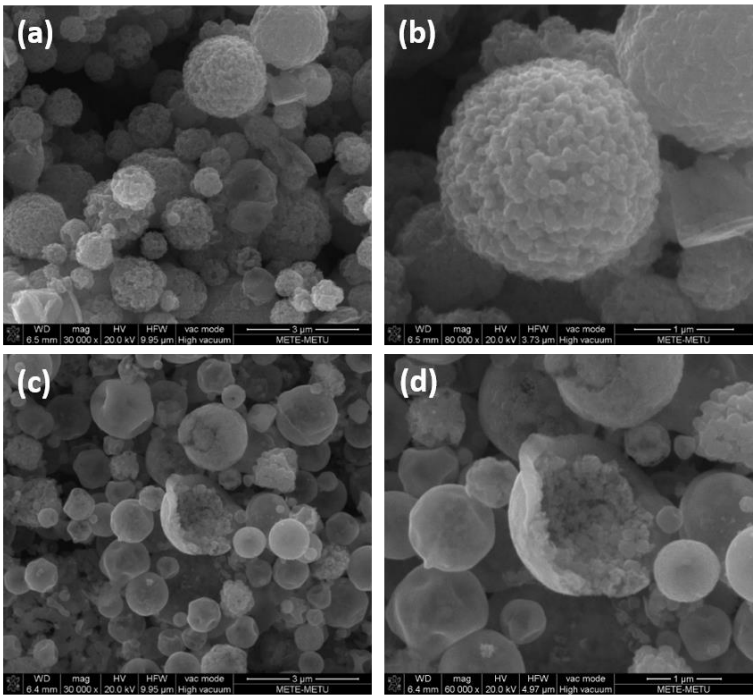

Figure 4.4 SEM images of: (a,b) Mn_5O_8, (c,d) Mn_2O_3 powders synthesized through spray pyrolysis method.

To understand the electrochemical activity of synthesized powders toward ORR and OER, polarization studies were recorded in O_2 purged 0.1 M KOH electrolyte as seen in Figure 4.5 (a,b). The onset potentials of Mn-based oxides were quite different than that of commercial 67 wt. % Pt/C catalyst. The onset potential, half-wave potential and potential at -3 mA cm^{-2} were used as figures of merit for ORR reaction. Even though the best values were obtained from the commercial catalyst, α-MnO_2 was closer to the Pt/C rather than the others. Even though the activities of Mn-based oxides were quite different in the ORR range, the activities in the OER range were close to each other.

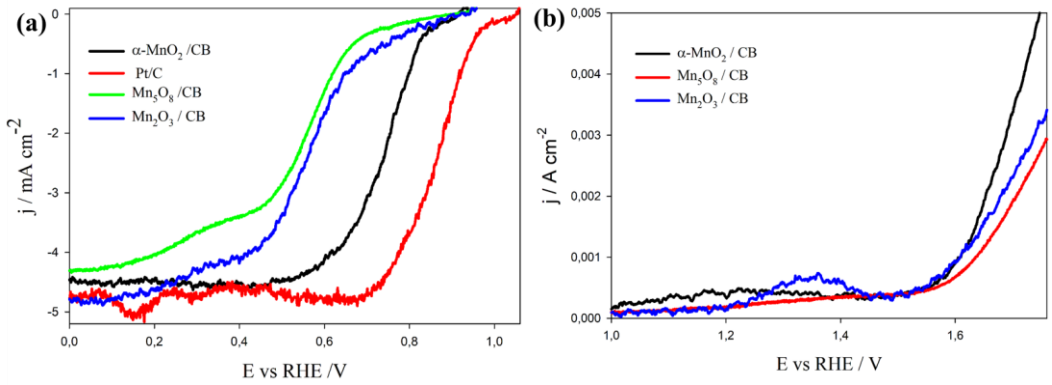

Figure 4.5 Rotating-disk voltammograms of MnO_2, Mn_5O_8, Mn_2O_3 and Pt/C loaded working electrode in O_2 purged 0.1 M KOH aqueous electrolyte with a sweep rate of 5 mV/s at 1600 rpm: (a) ORR and (b) OER range.

The potential at -3 mA cm^{-2} for α-MnO_2 was stated as 0.76 V vs. RHE on RDE (1600 rpm) in O_2 purged 0.1 M KOH solution at a scan rate of 20 mV s^{-1} [98], which was recorded as 0.70 V in this work with a similar condition (only scan rate was different, 5 mV s^{-1}). According to Meng et al. [98], onset potential and half-wave potential were 0.89 and 0.79, respectively. These values were 0.9 and 0.73 V vs. RHE, respectively in this work. Therefore, in addition to the commercial Pt/C catalyst, synthesized α-MnO_2 was used as a benchmark catalyst for ORR to compare other powders under the same conditions. Even though ORR activities were different for

each Mn oxides, OER activities were quite close to each other. Onset overpotentials of OER were approximately 340 mV, which was close to the reported OER catalysts in the literature [99].

To alter the oxygen reduction activity of α- MnO_2, changing the amount of K in the structure was investigated. Indeed, the existence of K+ ions in solution can change the thermodynamic stable phase of β-MnO_2 to α-MnO_2, the effect of the ion on structure change can be seen in Figure 4.6. When K+ ions present in the aqueous solutions that enter to the [2 x 2] tunnels of α-MnO_2. If longer times were allowed for reaction at high temperatures, formation of thermodynamically stable β-MnO_2 crystals with [1x1] tunnels are formed.

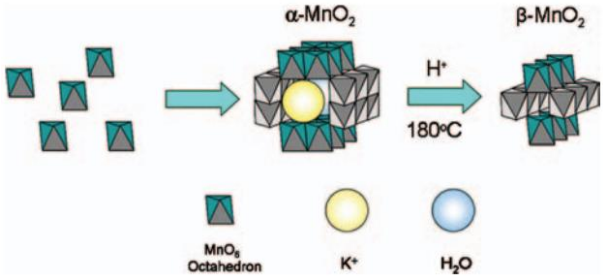

Figure 4.6 Schematic drawn of structures of α-MnO_2 and β-MnO_2 [95].

The K to Mn ratio in the structure without any treatment is approximately 0.12 at the synthesized α-MnO_2 powders according to the EDS results. The effect of HCl treatment and treatment conditions on K/Mn ratio was studied. Indeed, K doping concentration can change the oxidation states of Mn [100]. The change in the oxidation states, and/or creating mixed valence states were proven activity change in the ORR and OER range [98]. Therefore, in order to control the K doping amount, powders were soaked into 1 M HCl for different durations. After treatment of powders in 1 M HCl solution at room temperature for 1 hour decreased the ratio to 0.09. When the temperature was increased to 80 ^{o}C, K/Mn ratio was decreased to 0.08 after 6 hours. Dissolution of powders was observed when experiments were

held longer than twelve hours at high temperatures (100 ^{o}C). Dissolution of powders were observed when experiments were held longer than twelve hours at high temperatures (100 ^{o}C).

The linear sweep voltammograms were recorded in 0.1 M KOH solution at 1600 rpm, which can be seen in Figure 4.7. The standard potential of oxygen reaction was shown by a dotted line (E^{o}=1.23 V vs RHE). The removal of K from the structure had an adverse effect on the ORR and OER activity. In brief, α-MnO_2, Mn_5O_8 and Mn_2O_3 powders were produced by simple wet chemical and spray pyrolysis methods. The Mn_5O_8 and Mn_2O_3 powders synthesized through spray pyrolysis showed less electrocatalytic activity than α-MnO_2 in both ORR and OER range. Moreover, the effect of HCl treatment was investigated for α-MnO_2; however, removing of K from the structure negatively affected the activity in both ORR and OER ranges. The results of synthesized α-MnO_2 were similar to the reported activity of same structure in the literature. Thus, synthesized α-MnO_2 without any treatment was used as a benchmark catalyst for ORR to compare other powders under the same conditions.

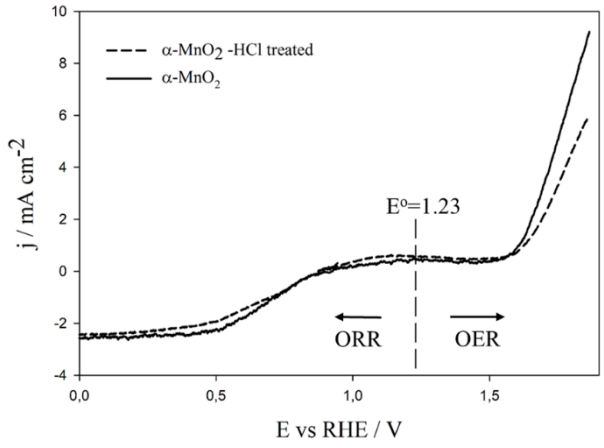

Figure 4.7 Rotating-disk voltammograms of HCl treated and nontreated α-MnO_2 loaded working electrode in O_2 purged 0.1 M KOH aqueous electrolyte with a sweep rate of 5 mV/s at 400 rpm in the ORR and OER range.

4.2 Results of Ag-based Oxides, Ag_2XO_4 (X= Cr, Mo, W)

The SEM micrographs of Ag_2CrO_4, Ag_2MoO_4 and Ag_2WO_4 experiments at different magnifications are given in Figure 4.8. SEM images of Ag_2CrO_4 and Ag_2WO_4 powders, given in Figure 4.8(a-b, e-f) reveal that powders having homogeneous microstructures with fine particle sizes were produced. On the other hand, homogeneous microstructures in the micron range were obtained for Ag_2MoO_4 powders. When the results of the experiments were investigated in the SEM, the formation of nanostructures on the surface of powders was observed when electron bombardment was localized for approximately 2 minutes, which can be seen in Figure 4.9(a,b). In other words, a new phase was formed during electron beam irradiation. Powders investigated in Figure 4.9 were pure Ag_2WO_4 obtained at polyvinylpyrrolidone (PVP) assisted hydrothermal reaction. The only difference is the addition of 1.5 g of PVP to the silver solution; however, particle sizes of powders were increased, which enable us to see the formation of a new phase during the electron bombardment for 2 minutes. Details of the experiment, XRD spectra and results of Rietveld refinement of synthesized Ag_2WO_4 powders (with PVP addition) were given in Figure 4.10. This powder was no longer investigated due to the big particle size. In the literature, similar behavior was observed and that was attributed to the low energy barrier of diffusion of silver atoms. Therefore, silver nanostructures were formed but silver vacancies were created in the structure [31], [101]. Structural disorder formation in the Ag_2WO_4 structure may increase the electrocatalytic activity. This can be the subject of future study.

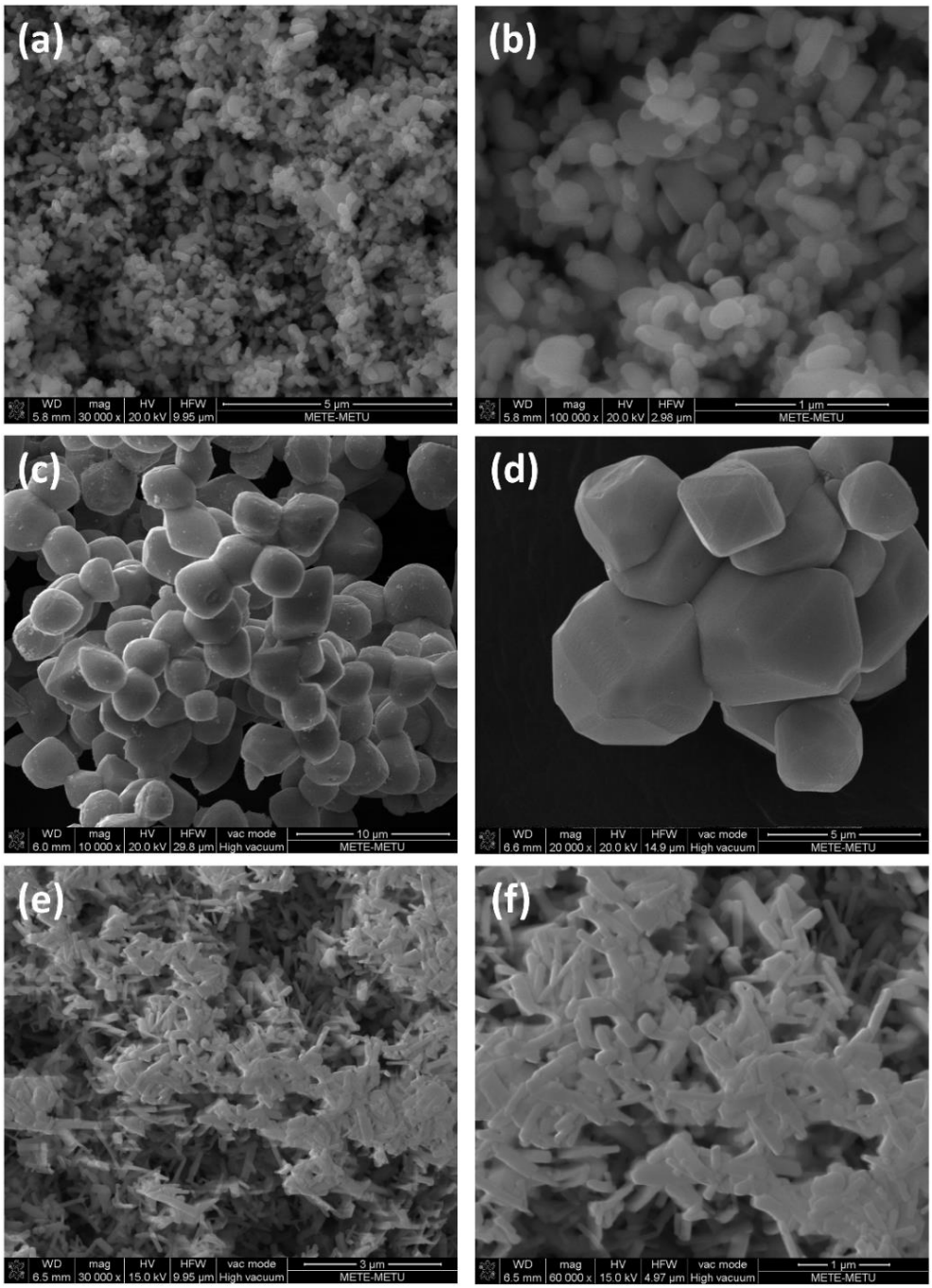

Figure 4.8 SEM images of: (a,b) Ag_2CrO_4 (c,d) Ag_2MoO_4 and (e,f) Ag_2WO_4 powders.

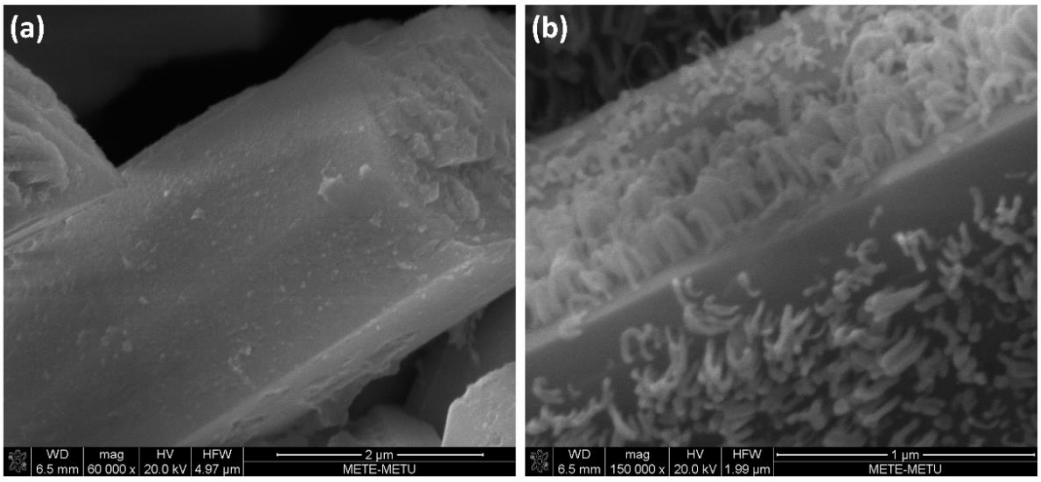

Figure 4.9 SEM images of Ag_2WO_4 powders, synthesized at PVP assisted hydrothermal synthesis, (**a**) at time zero and (**b**) after 2 minutes of the electron bombardment.

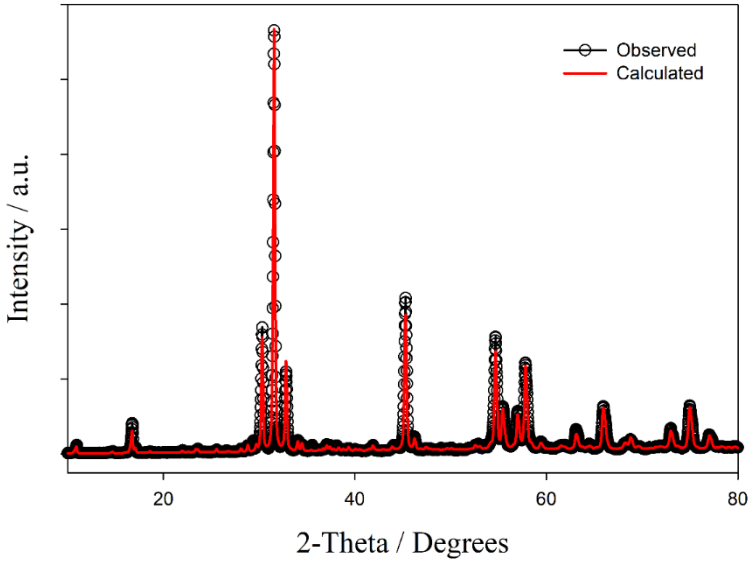

Figure 4.10 The XRD spectra and results of Rietveld refinement of synthesized Ag_2WO_4 powders (ICSD 243992). PVP-assisted hydrothermal method was investigated to decrease the particle size of Ag_2WO_4 powders. The only difference between the experiments was the addition of 1.5 g of PVP addition to the $AgNO_3$ solution. All other steps are similar.

XRD method was used to determine the crystal structures of the produced powders. The XRD spectra of powders and the peak positions of the corresponding phases can be seen in Figure 4.11. The XRD spectra of the powder showed diffraction peaks which were corresponding to the pure orthorhombic phase of Ag_2CrO_4 and no other impurities were found as seen in Figure 4.11(a). The percentage of R_{wp} was found as 9 by Rietveld fitting carried out with MAUD software [97], showing a good agreement with the 16298 ICSD card. According to the Rietveld refinement of the XRD pattern of powders obtained at the Ag-Mo experiment condition, the desired phase was obtained. Peak positions of powder coincide with the peak position of the cubic spinel β-Ag_2MoO_4 phase (ICSD Card number: 238014) and the percentage of R_{wp} of the sample was found as 13 by refinement (See Figure 4.11(b)). Refinement of powders obtained at the Ag-W experiment indicated that powders consisted of thermodynamically stable α-Ag_2WO_4 without any impurity as seen in Figure 4.11(c). The percentage of R_{wp} after refinement of the sample with respect to 243992 ICSD card was found as 10. Rietveld refinement parameters of Ag_2CrO_4, Ag_2MoO_4 and Ag_2WO_4 powders can be seen in Table 4.1. In brief, according to the results of XRD data and Rietveld refinement, Ag_2CrO_4, Ag_2MoO_4, and Ag_2WO_4 powders were synthesized without impurities.

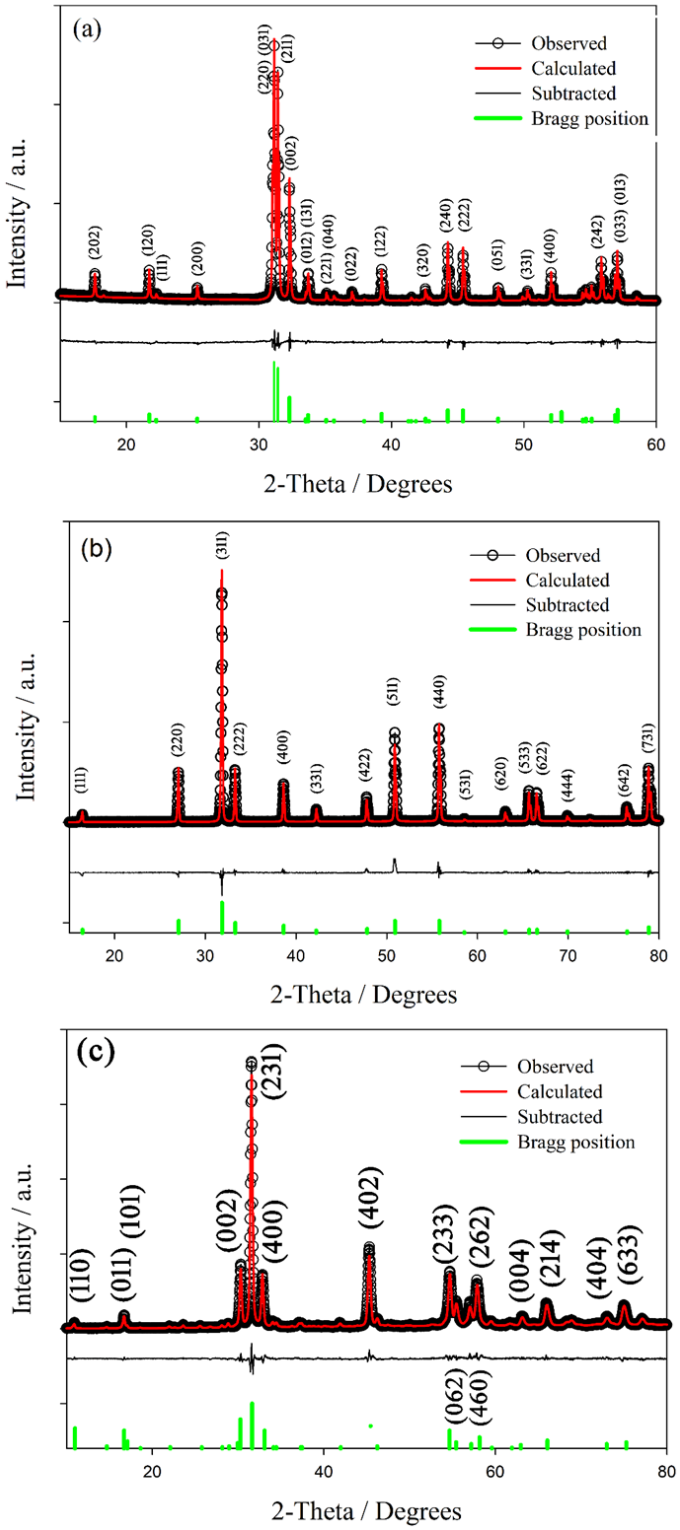

Figure 4.11 The XRD spectra and results of Rietveld refinement of (**a**) Ag_2CrO_4, (**b**) Ag_2MoO_4 and (**c**) Ag_2WO_4 powders.

Table 4.1 Rietveld refinement parameters of Ag_2CrO_4, Ag_2MoO_4 and Ag_2WO_4 powders.

Compound	Ag_2CrO_4	Ag_2MoO_4	Ag_2WO_4
Crystal system	Orthorhombic	Cubic	Orthorhombic
Space group	Pnma	Fd-3m	Pn2n
a (nm)	1.006 ± 2.05E-4	0.931 ± 8.85E-5	1.0894 ± 3.32E-4
b (nm)	0.702 ± 1.45E-4		1.2019 ± 4.25E-4
c (nm)	0.553 ± 1.07E-4		0.5889 ± 1.71E-4
Rwp / %	9	13	10

To understand the electrochemical activity of synthesized powders toward the oxygen reduction reaction (ORR), polarization studies were recorded in O_2 and N_2 purged 0.1 M KOH electrolyte as seen in Figure 4.12 (a,b). Only background current recorded in N_2 saturated electrolyte for Ag_2CrO_4 loaded working electrode were given in Figure 4.12 (a). The current density increase was not observed, which suggested no reaction occurs in N_2 purged electrolyte. On the other hand, linear sweep voltammograms of glassy carbon working electrode loaded with carbon black (CB), Ag_2CrO_4 and Ag_2CrO_4/CB powders were showed activity in O_2 saturated alkaline medium, which can be seen in Figure 4.12 (a). The effect of carbon black addition on the activity of Ag_2CrO_4 was recorded to see no remarkable change in the ORR kinetics, which can be seen in Figure 4.12 (a). Even though the current density and onset potential of carbon black (Printex L6) loaded working electrodes were better than bare glassy carbon electrode, there was a dramatic increase in the onset potential and limiting current density when Ag_2CrO_4 were loaded on glassy carbon. Onset and half-wave potentials remained approximately the same with a little shift in the limiting current density when carbon black was added to the mixture (1:1 weight ratio). The increase in the limiting current density might be expected due to the high surface area and conductivity of carbon black.

The linear sweep voltammogram of Pt/C, α-MnO_2, Ag_2CrO_4, Ag_2MoO_4 and Ag_2WO_4 powders that were carried out at 1600 rpm can be seen in Figure 4.12 (b). Voltammograms point out the increase of current density in the mixed kinetic region for all powders. The onset potential, half-wave potential, limiting current density and overpotential recorded at -3 mA/cm^{-2} ($\eta_{-3mA\ cm^{-2}}$) were accepted as being a good indicator for the oxygen reduction reaction activity of produced powders [98]. The onset potential, half-wave potential and limiting current density decreased with following of Pt/C > Ag_2WO_4 > α-MnO_2 > Ag_2MoO_4 > Ag_2CrO_4. The onset potential and half-wave potential of the oxygen reduction reaction on the Ag_2WO_4 catalyst was slightly more positive with respect to the others. The limiting current density of the Ag_2WO_4 catalyst was also higher than that of Ag_2CrO_4 and Ag_2MoO_4. Onset potential, half-wave potential, limiting current density and potential recorded at -3 mA/cm^2 for Ag_2WO_4/CB powders were 930 mV (η_0=300 mV), 710 mV, 5 $mA\ cm_{geo}^{-2}$ and 690 mV (η_3=540 mV), respectively. The onset potential of Pt/C recorded in this study was 0.86 V. The same value was recorded in the literature [98]. Even though the onset and half-wave potential of Pt/C was approximately 100 mV lower than the Ag_2WO_4 loaded working electrode, achieved limiting current densities were approximately the same. Furthermore, the ORR kinetics of the Ag_2WO_4 catalyst was quite similar to the α-MnO_2 catalyst produced by precipitation method, which is one of the most researched ORR catalysts in the literature [25], [45], [98], this might be the evidence to be a good catalyst candidate. The potential at -3 $mA\ cm^{-2}$ for α-MnO_2 was recorded as 0.70 V in this work with a similar condition. According to Meng et al. [98], onset potential and half-wave potential were 0.89 and 0.79, respectively. These values were 0.9 and 0.73 V vs. RHE, respectively in this work. On the left side of the graph (Figure 4.12 (b)), an enlarged version of the potentials in the onset potential range can be seen.

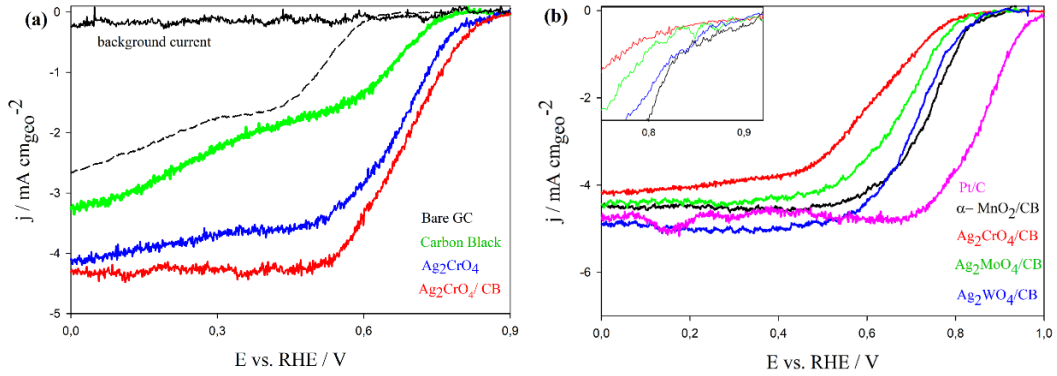

Figure 4.12 (a) Rotating-disk voltammograms of pure Ag_2CrO_4, carbon black (CB/ Printex L6) and Ag_2CrO_4/CB loaded and bare glassy carbon working electrode in O_2 purged 0.1 M KOH aqueous electrolyte with a sweep rate of 5 mV/s at 1600 rpm. Background current was recorded at N_2 saturated 0.1 M KOH aqueous electrolyte. (b) Rotating-disk voltammograms of Pt/C, α-MnO_2, Ag_2CrO_4, Ag_2MoO_4, Ag_2WO_4 and carbon black loaded and bare glassy carbon working electrode in O_2 purged 0.1 M KOH aqueous electrolyte with a sweep rate of 5 mV/s at 1600 rpm.

Nyquist plots of EIS patterns were given in Figure 4.13 (a,b) where the inserts show the equivalent circuits used in fitting. For the EIS spectrum recorded at 0.765 V which is closer to the kinetically controlled region, circuit consists of series connection of electrolyte resistance (R_{EL}) and two C/R circuits, in which the first represents the capacitance and resistance of the electrode-electrolyte interface and the second represents double-layer capacitance (C_{DL}) and charge transfer resistance (R_{CT}). The equivalent circuit used for the EIS spectrum recorded at 0.7 V, where mass transport control emerges, consists similarly of R_{EL}, C_{DL} and R_{CT} and additionally, convection type Warburg element (W_{INF}) to model diffusion in rotating disk environment. This element models impedance using an analytical approximation of convective diffusion considering the fact that concentration perturbation can also occur outside of the diffusion layer, as it is implemented in EC-Lab software. The impedance dependence of this element on frequency is given as in Equation (4.2):

$$Z(\omega) = R_D \frac{\sqrt{\gamma^2 + \tau_D i\omega}}{\gamma + \tau_D i\omega} \tag{4.2}$$

The main term here is the diffusive resistance, R_D. An inductive loop appears in the low-frequency region of the spectrum recorded at 0.7 V. This is due to the relaxation of the adsorbed reaction intermediates [102], and is represented by an inductor element (L). The fitted parameters were given in Table 4.2. The double-layer capacitance values of the samples are not very much different from each other at the region close to kinetic control. As the process goes to mass transfer control, capacitance decreases slightly except for Pt/C. Charge transfer resistance is the lowest for Pt/C sample at all working potentials, then comes Ag_2WO_4. As the working potential decreases there is a decrease in charge transfer resistance expectedly, as mass transport takes over the control. At kinetic control, the effect of resistive loads on impedance due to interface seems to play a considerable role too, as well as electron transfer process. At the lower potential, the diffusive resistance determines the impedance rather than the charge transfer resistance. Among the studied oxides, Ag_2WO_4 sample at both kinetic and mass transport regions has a lower combination of all three resistive loads and thus performs better in ORR.

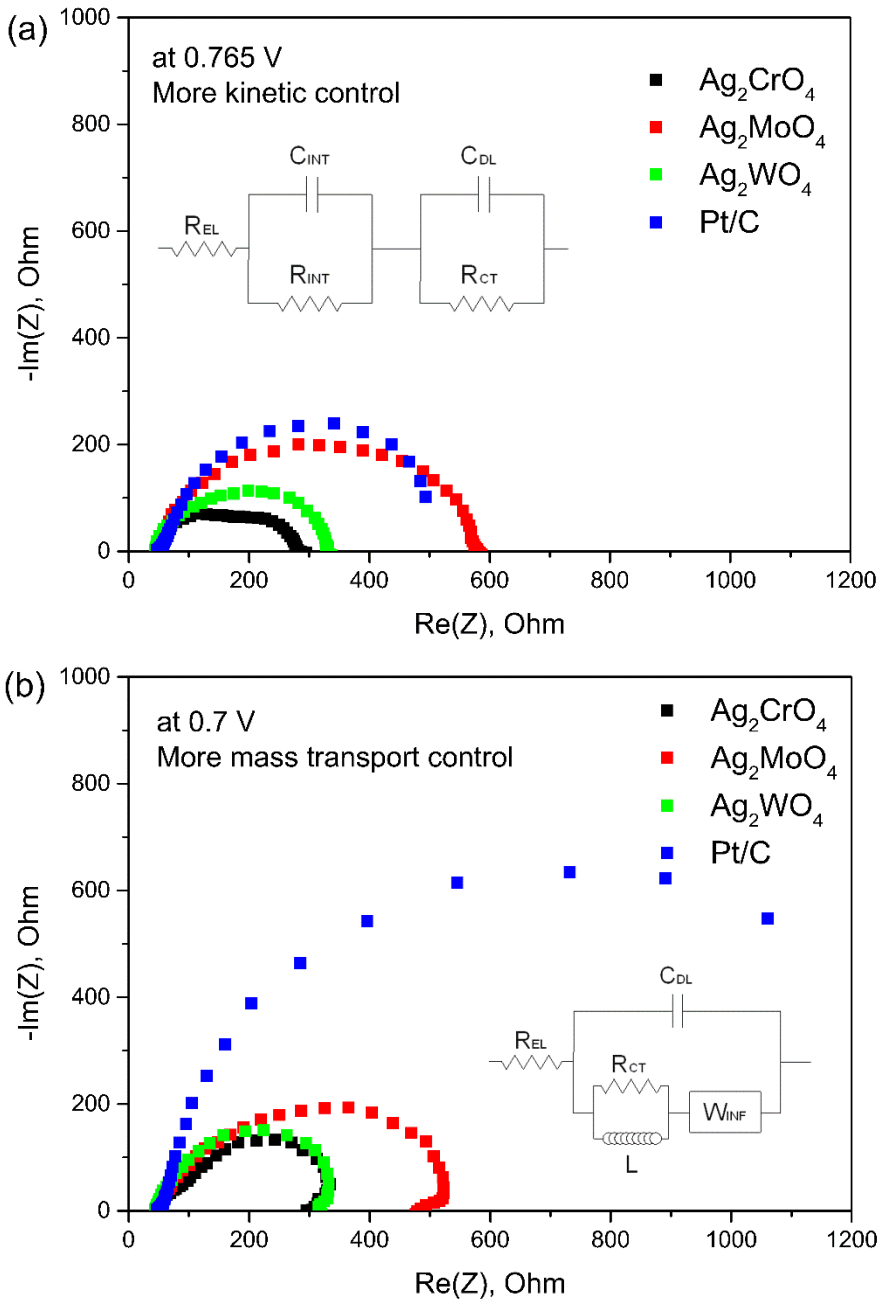

Figure 4.13 EIS spectra of samples at a working potential of (a) 0.765 V and (b) 0.7 V. Insert show the equivalent circuits used in fitting.

Table 4.2 Fitted parameters of the equivalent circuit models in EIS analyses.

	C_{DL} (F) × 10^{-3}		R_{CT} (Ohm)		R_{INT} (Ohm)	R_D (Ohm)
E_{WE} (V)	0.765	0.7	0.765	0.7	0.765	0.7
Ag_2CrO_4	1.385	0.121	114.9	24.6	116.6	274.4
Ag_2MoO_4	0.108	0.060	102.6	13.7	412	452.3
Ag_2WO_4	0.271	0.234	70.6	18.1	212.5	283.7
Pt/C	1.978	3.259	16.2	0.84	464.3	1237

To gain a deeper insight into the oxygen reduction reaction activities, ORR mass activities, Koutecky–Levich (K–L) plots, Tafel slopes, chronoamperometry, accelerated durability test and linear sweep voltammograms on gas diffusion layer were investigated, which can be seen in Figure 4.14(a-f). As seen in Figure 4.14(a), the mass activity of commercial Pt/C, synthesized α-MnO_2 and Ag_2WO_4 powders were drawn. Mass normalized activities of α-MnO_2 and Ag_2WO_4 powders were quite similar to each other. Mass normalized activities of Ag_2WO_4 and α-MnO_2 at 0.8 V (vs. RHE) were approximately 1 mA mg^{-1}, however, that of Pt/C powder was 4.8 mA mg^{-1}. Indeed, various production method results in different particle size, morphology and surface area. Effect of each difference of these brings about different specific and mass activities [45] For example, the mass activity of α-MnO_2 synthesized with various methods varied widely from 0.26 to 15 mA mg^{-1} in literature [45]

Koutecky–Levich (K–L) plots, given in Figure 4.14(b), were enabled us to calculate the average electron transfer number for the oxygen reduction reaction from the slope of 1/j versus $1/\omega^{1/2}$ graph. Koutecky-Levich plots were obtained at 0.365 V (vs. RHE) at various rotation speeds of RDE. In the literature, there is a significant effort to find oxygen electrode catalysts that follow the 4-electron transfer pathway. The electron transfer numbers (n) of Ag_2CrO_4, Ag_2MoO_4, Ag_2WO_4 and α-MnO_2 at 0.365 V were

approximately calculated as 3.8, 3.4, 3.8 and 4, respectively. The electron transfer numbers of these powders are close to 4, which means that these powders might be a candidate to favor a 4 electron oxygen reduction process. Meng et al. [98] reported that the electron transfer number of MnO_2 loaded carbon powders were close to 4.2. This information was consistent with our results.

Tafel plots of Pt/C, α-MnO_2 and Ag_2WO_4 powders obtained at the low overpotential region of ORR can be seen in Figure 4.14(c). The Tafel slope of powders followed a decreased trend in the order of α-MnO_2 > Pt/C> Ag_2WO_4 with the following values: 99, 81 and 47 mV dec^{-1}, respectively. The lower Tafel slope of Ag_2WO_4 with respect to the commercially used catalysts, α-MnO_2 and Pt/C, indicated the fast ORR kinetics of Ag_2WO_4 at the low potential region. According to the results of LSV, EIS, K-L plots, Tafel slopes, the promising ORR catalyst in the alkaline medium was Ag_2WO_4 powder. The activities of W-based oxides for the ORR and OER were reported in the literature. For example, $ZnWO_4$ nanobricks, $ZnWO_4/Fe_3O_4$ nanocomposites, $CoWO_4$ and $FeWO_4$ nanoparticles were investigated for oxygen reactions to be used in various applications [103]–[106] Summary of the results and comparison with reported other Ag and W based oxides can be seen in Table 4.3.

The stability of Ag_2WO_4 was investigated by chronoamperometry and accelerated durability tests. Chronoamperometric response of Ag_2WO_4 was obtained at 0.7 V in O_2 purged 0.1 M KOH solution. Obtained relative current versus time graph seen in Figure 4.14(d), revealed that Ag_2WO_4 retained 84 % of its initial current density after 20000 seconds at 0.7 V. Accelerated durability test was also recorded by cyclic between 0.6 to 1 V RHE. Linear sweep voltammograms were recorded before and after the test. As can be seen in Figure 4.14(e), only approximately 25 mV decrease in half-wave potential was observed after 2000 cycles. There was no noticeable change in the linear sweep voltammogram that points out the good durability of Ag_2WO_4 in the alkaline environment.

Ag_2WO_4 powders were also loaded on gas diffusion layer and voltammograms were recorded in 6M KOH (See in Figure 4.14(f) because high concentrations were used

in metal-air batteries. Even though higher current densities for ORR were achieved with a higher mass loading (0.44 mg cm^{-2}) of Ag_2WO_4 powders on GDL rather than RDE (0.25 mg cm^{-2}), onset potential and potentials obtained at -3 mA cm^{-2} current density were similar on Ag_2WO_4 loaded GDL and RDE in 0.1 and 6 M KOH electrolyte, respectively. Equilibrium potential for ORR and OER was drawn by the vertical dotted line at 1.23 V. As seen in Figure 4.14(f), OER kinetics of Ag_2WO_4 oxide were also investigated. The overpotential at 10 mA cm^{-2} current density was also used as a figure of merit. However, the overpotential of oxygen evolution at this current density was approximately 670 mV. In other words, OER kinetics revealed that Ag_2WO_4 powder was not a good candidate to be an OER catalyst. Furthermore, the voltammogram of Ag_2WO_4 showed three anodic peaks that appeared before the onset of the oxygen evolution reaction. In the literature, pre-peaks before the oxygen evolution have been recorded for many catalysts [107]. For example, Ni, Ni-Fe, NiOx and hybrid $Ni(OH)_2$ powders were investigated for OER [108]–[110]. According to these works, pre-oxidation peaks pointed out the change of oxidation states from Ni^{+2} to Ni^{+3}/Ni^{+4}, formation of oxide and hydroxides; however, the formation of redox reactions and change of structure increased the activity the of these catalysts. On the other hand, these peaks were absent for some known catalysts such as IrO_2, $CoSn(OH)_6$, Pt, Pd, CoO, etc. [110], [111]. Peaks observed in this study appeared before the onset of the oxygen evolution reaction.

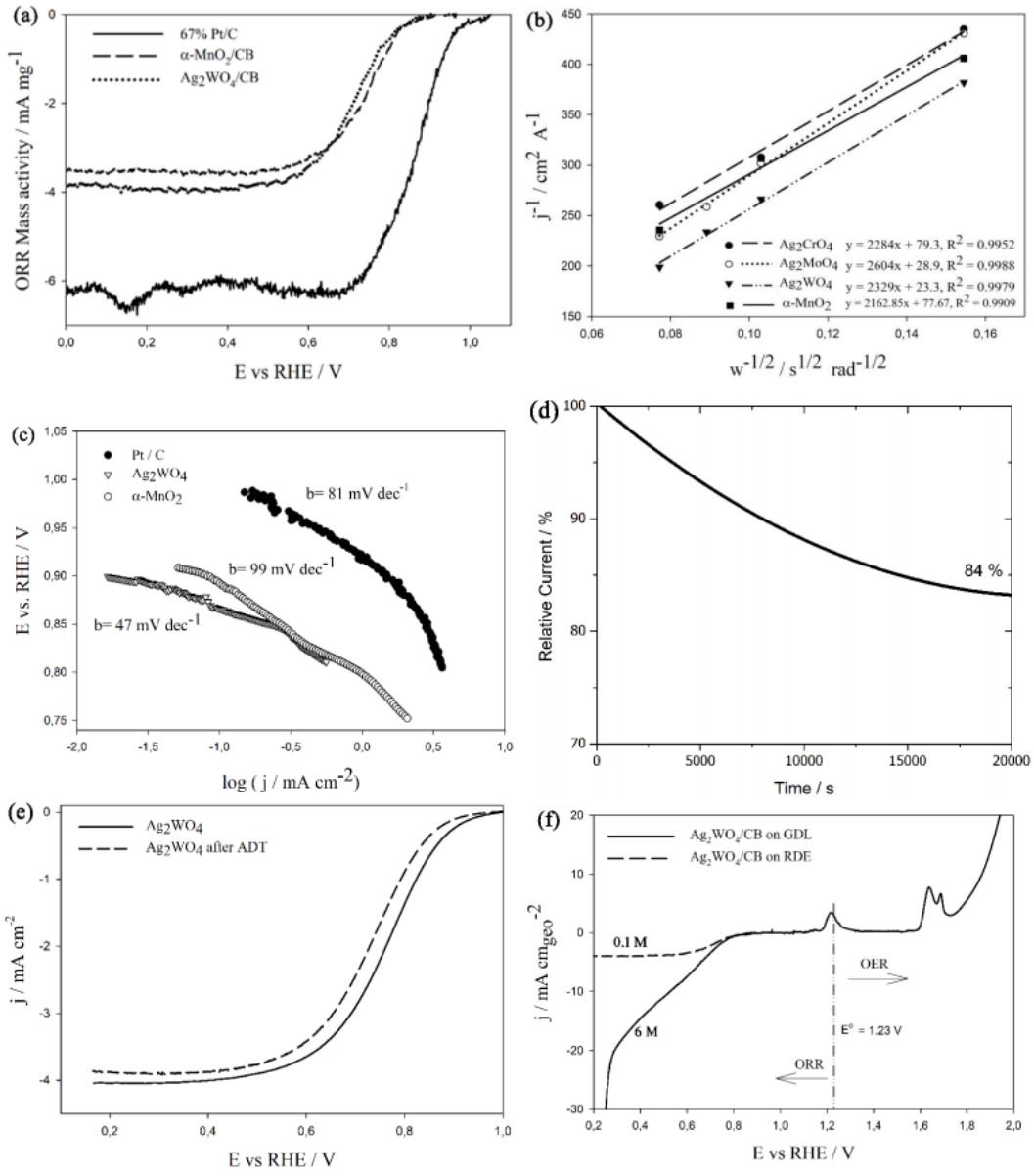

Figure 4.14 (a) Mass activities of synthesized Ag_2WO_4, α-MnO_2 with carbon black mixture and commercial 67 wt% Pt/C; (b) Koutecky-Levich plots obtained at 0.365 V (vs. RHE) for Ag_2CrO_4, Ag_2MoO_4, Ag_2WO_4 and α-MnO_2 powders; (c) Tafel plots of synthesized Ag_2WO_4, α-MnO_2 with carbon black mixture and commercial 67 wt% Pt/C; (d) Chronoamperometry curve of Ag_2WO_4 powders; (e) Linear sweep voltammograms of Ag_2WO_4 powders before and after the accelerated durability test; (f) Linear sweep voltammogram of Ag_2WO_4 powders loaded on gas diffusion layer for ORR and OER range.

Table 4.3 Summary of ORR activities of powders revealed from RDE measurements.

Samples	**Onset (mV)**	**$\eta_{-3mA\ cm^{-2}}$ (mV)**	**$E_{1/2}$ (mV)**	**Tafel Slope (mV dec^{-1})**	**$j_{limiting}$ (mA cm^{-2})**	**n (e^-)**	**Ref.**
Ag_2WO_4	930	540	710	47	5	3.8	This work
α- MnO_2	900	530	730	99	4.5	4	This work
67 wt% Pt/C	1000	390	860	81	4.7	-	This work
α- MnO_2	-130[a]	470	-220[a]	-	5[c]	4.2	[98]
α- MnO_2	-140[a]	-	-250[a]	184	3[c]	-	[25]
20 wt% Pt/C	-	-	860	-	-	-	[98]
20 wt% Pt/C	970	410	830	53	4.97	-	[39]
RGO/$ZnWO_4$/Fe_3O_4	965	430[c]	-	-	8.9	3.8	[104]
Ag-MnO_2	-60[b]	-	-	77	-	3.7	[48]
$CoWO_4$	700	-	-	62	-	3.98 - 4.03	[105]
$Co_{0.5}Mn_{0.5}WO_4$	830	490	730	-	10.3	3.6	[112]

[a] Potentials were given versus SCE reference electrode, [b] Potentials were given versus Ag/AgCl reference electrode, [c] Data were read from the graph.

To find the reactions and investigate the microstructures, Ag_2WO_4 powders loaded on the gas diffusion layer was structurally characterized after holding at oxidizing potentials. The difference in the microstructures before and after holding at oxidizing potentials can be seen well in Figure 4.15. Microstructures of sprayed Ag_2WO_4

powders, after the experiment, changed in form and different fiber-like structures were seen.

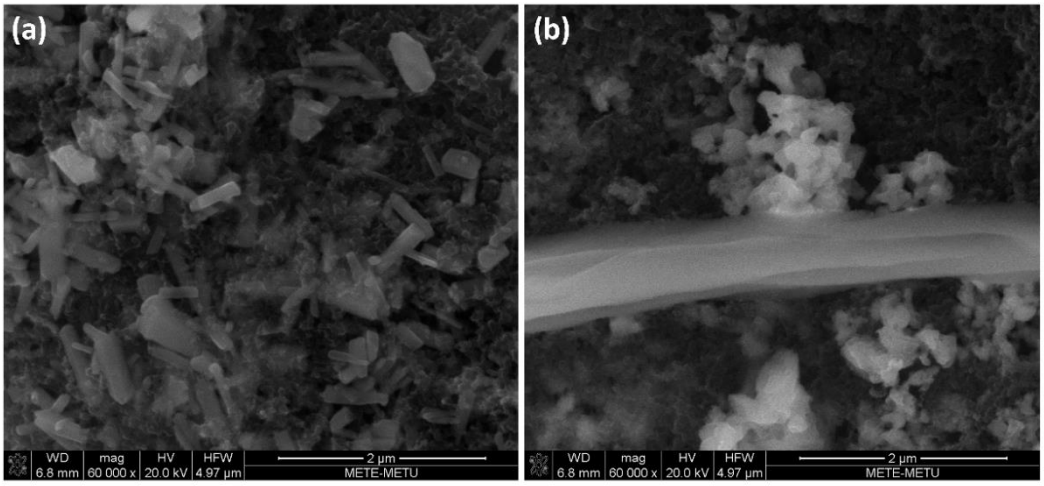

Figure 4.15 SEM micrographs of Ag_2WO_4 coated gas diffusion layer (a) before and (b) after several linear sweep voltammograms recorded in the OER range (0.865 to 2 V vs. RHE).

EDS mapping was used to see the distribution of elements on the surface of carbon paper to form an opinion about fiber-like structures. The EDS mapping images, as seen in Figure 4.16, were also in accordance with our expectations. They could be the oxides of silver. Cyclic voltammograms of silver and silver alloys were discussed in the alkaline electrolyte by various researchers [30], [113]–[117], which were similar to our voltammograms. Generally, pre-peaks on the oxidation potentials were attributed to the formation of one or more monolayers of AgOH or Ag_2O before the formation of a bulk Ag_2O layer. Then, Ag_2O and AgO were probably formed [116]. According to Guo et al. [117], there was a relation between the first peak (observed at 0.23 V vs. Hg/HgO) and the ORR activity of Ag/C powder [30]. The formation of nanostructures on the surface of the powders during electron beam irradiation (See Figure 4.9) is a good indicator of the low energy barrier of diffusion of silver atoms. This might be the reason of observation of similar peaks. During the reverse scan,

oxidation reactions were reversed and corresponding cathodic peaks showed up [114]. Furthermore, Ag_2O_3 formation was suggested to occur in the region of oxygen evolution [115].

To gain insights into the oxygen evolution reaction (OER) activity, linear sweep voltammograms of Ag_2CrO_4, Ag_2MoO_4, Ag_2WO_4 loaded RDE were recorded (See Figure 4.17). Pre-peaks before the oxygen evolution have also been recorded for Ag_2CrO_4 and Ag_2MoO_4 oxides. Similar behavior was observed with a very low shift in the potentials of the pre-oxidation peaks. The reason of these anodic peaks was further investigated by cyclic voltammetry experiments. The cyclic voltammogram of Ag_2WO_4 was recorded to find the reactions and investigate the stability of catalysts as seen in Figure 4.18. The potential difference between the working and the reference electrodes was firstly scanned from 0 to cathodic side, then it was reversed. As can be seen, anodic peaks were observed at each cycle in the OER range. Before the onset of oxygen evolution, there were three anodic oxidation peaks. Moreover, cathodic peaks were recorded when potential difference was reversed. In order to find the corresponding cathodic and anodic potentials, two cyclic voltammograms were recorded at different potential ranges. Firstly, the potential difference was scanned from +0.65 V to 1.2 V, then it was reversed until -0.2 V (vs. 1 M Hg/HgO reference electrode) was achieved, which can be seen in Figure 4.19. Both reduction peaks were observed. However, one reduction peak was observed when the potential difference was scanned until 1.515 V RHE (See Figure 4.19(a)). This might be attributed to two different oxidation reactions. The oxidation reaction occurred at approximately 1.215 V was reversed at 1.015 V RHE. Furthermore, anodic (1.615 V) and cathodic (1.315 V) peaks might be correlated with each other. Observation of second reduction peak in Figure 4.19(b) might be attributed to the occurrence of first anodic reaction even though potential difference scan was started from 1.515 V, which gave more driving force than necessary for the first oxidation reaction, which has occurred at approximately 1.215 V RHE.

To understand the reactions, another different silver oxide, AgO powders, were also compared with Ag_2WO_4 powders. The same peaks with a slight shift in the position

were recorded which points out the interaction of pre-peaks with Ag (See Figure 4.20). Details of the OER experiments revealed that Ag_2CrO_4, Ag_2MoO_4 and Ag_2WO_4 powders have no activity in the OER range.

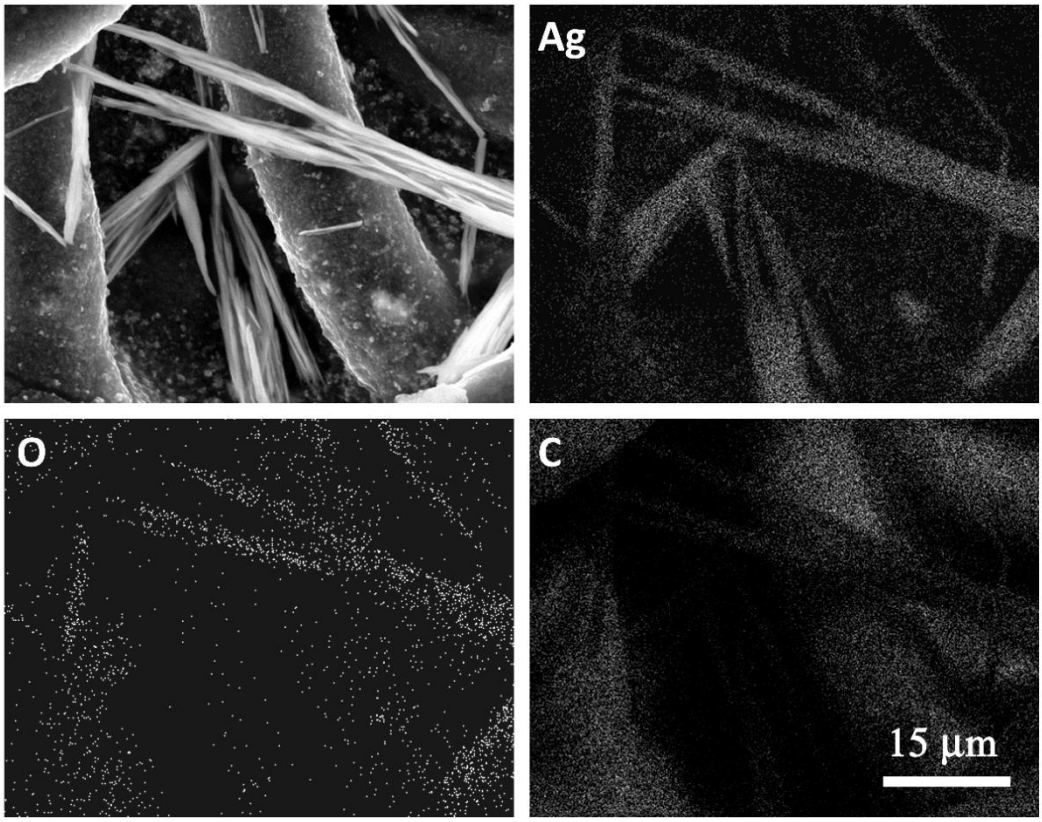

Figure 4.16 EDS mapping of Ag_2WO_4 coated gas diffusion layer after several scanning in the OER range. The scale at the right bottom applies to all.

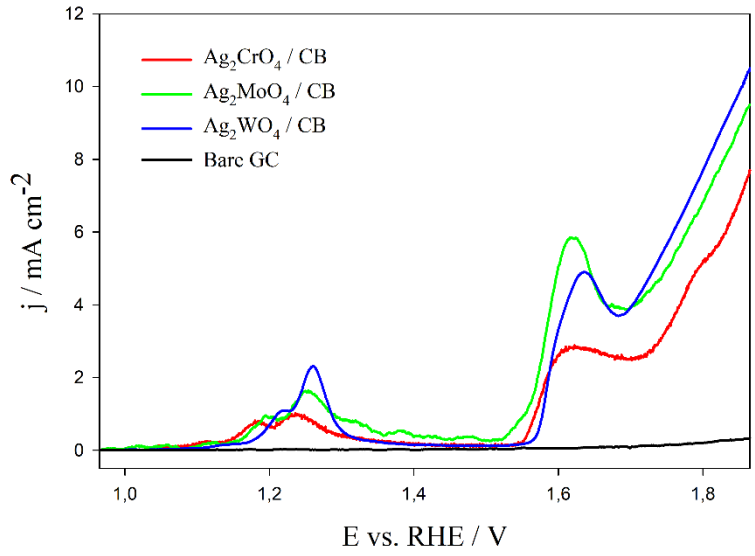

Figure 4.17 Rotating-disk voltammograms of Ag_2CrO_4, Ag_2MoO_4, Ag_2WO_4 and bare glassy carbon working electrode in O_2 purged 0.1 M KOH aqueous electrolyte with a sweep rate of 5 mV/s.

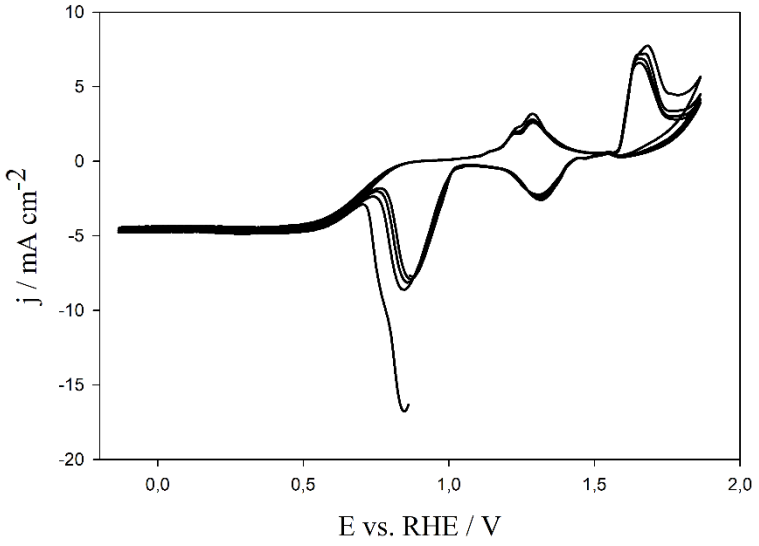

Figure 4.18 Cyclic voltammograms of Ag_2WO_4 powder in O_2 purged 0.1 M KOH aqueous electrolyte with a sweep rate of 20 mV/s.

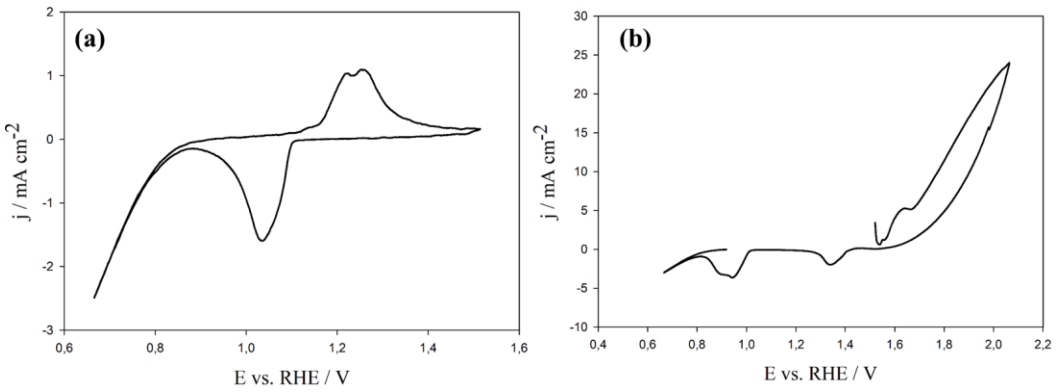

Figure 4.19 Cyclic voltammogram of Ag_2WO_4 powders recorded for investigation of anodic and cathodic peaks; (a) between 0.865 and 1.515 V RHE, and (b) 1.515 V and 2.1 V RHE.

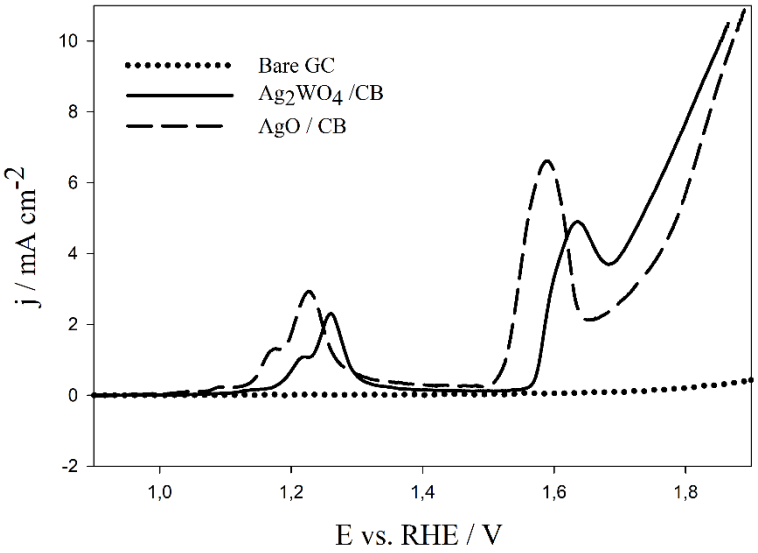

Figure 4.20 Rotating-disk voltammograms of AgO, Ag_2WO_4 loaded and bare glassy carbon working electrode in O_2 purged 0.1 M KOH electrolyte with a sweep rate of 5 mV/s at 1600 rpm.

Another important point is the coincidence of potential (approximately at 0.9 V) of oxygen reduction reactions with the reduction peaks of Ag-oxides formed at high oxidation potentials (See Figure 4.18). It should be proved that current increase after 0.9 V RHE in the cathodic side is caused by the oxygen reduction reaction. To

investigate, AgO and Ag_2WO_4 powder loaded on glassy carbon electrode were tested in N_2-saturated electrolyte. Voltammograms (except blue line in Figure 4.21) were recorded from +0.1 V to – 1 V versus Hg/HgO/1M reference electrode. Small background current was recorded for these powders. In other words, activity of Ag_2WO_4 in O_2 saturated electrolyte is correlated with the oxygen reduction reaction. The blue line in Figure 4.21 showed the voltammogram of Ag_2WO_4 loaded glassy carbon working electrode after scanning at high oxidation potentials. Indeed, two reactions occurred at the same time but the second reduction peak (blue line) was only observed after the anodic scan. Therefore, evaluation of oxygen reduction activity made up to now is valid because all voltammograms recorded only towards to the cathodic side after powder deposition on working electrode.

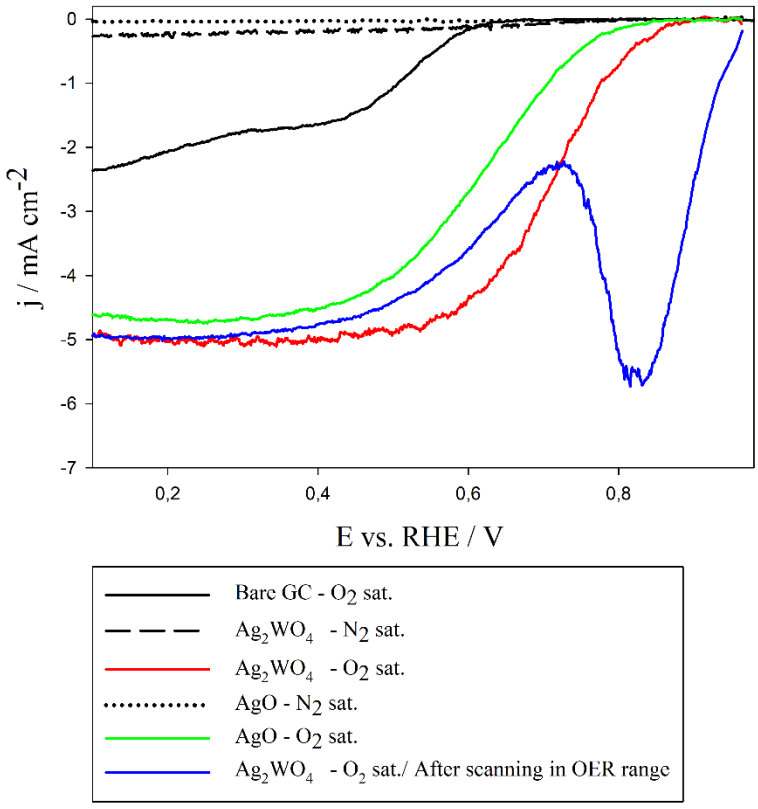

Figure 4.21 Rotating-disk voltammograms of AgO, Ag_2WO_4 loaded and bare glassy carbon working electrode in O_2 and N_2 purged 0.1 M KOH aqueous electrolyte with a sweep rate of 5 mV/s.

To investigate reactions that occurred in the OER region, XRD spectra of Ag_2WO_4 loaded carbon paper were compared before and after the linear sweep test (See Figure 4.22(a)). Four linear sweep voltammograms were recorded between 0.865 V and 2 V. While the intensity of Ag_2WO_4 peaks decreased, new peaks were observed. Peaks at 32.07°, 32.35 °, 34.22 ° and 39.46° 2Theta coincided with the peaks of monoclinic AgO powder (Card no: 96-900-8963). XRD data between the 2Theta range of 10-60° can be seen in Figure 4.23. According to XRD results, AgO formation was recorded even after four linear sweep voltammograms in the OER range. Raman spectrometry is a complementary technique for structural characterization to XRD of Ag_2WO_4. The observed Raman spectrum (See Figure 4.22(b)) is very similar to that of α- Ag_2WO_4 reported in the literature [118]. The Raman modes were recorded at 124, 180, 205, 248, 305, 339, 365, 583, 666, 780, 802, 882 cm^{-1}. The most intense peak was observed in 882 cm^{-1} which was ascribed to the symmetric starching of O-W-O bond. The bands between 500-1000 cm^{-1} were ascribed to vibrations of W-O bonds in [WO_6] clusters; while bands between 100-500 cm^{-1} were ascribed to vibrations of $[AgO_n]_{n=2,4,6,7}$ clusters [119]. The Raman spectrometry was also obtained after several linear sweep voltammograms recorded on Ag_2WO_4 loaded RDE. The most intense peak of pure Ag_2WO_4 powder disappeared. The change in the structures after LSV in the OER range can be seen in Figure 4.22 (a,b). Visual examination of samples also enabled us to detect the change in the color of the powder from gray to black after doing several LSV in the OER range (0.865 V and 2 V).

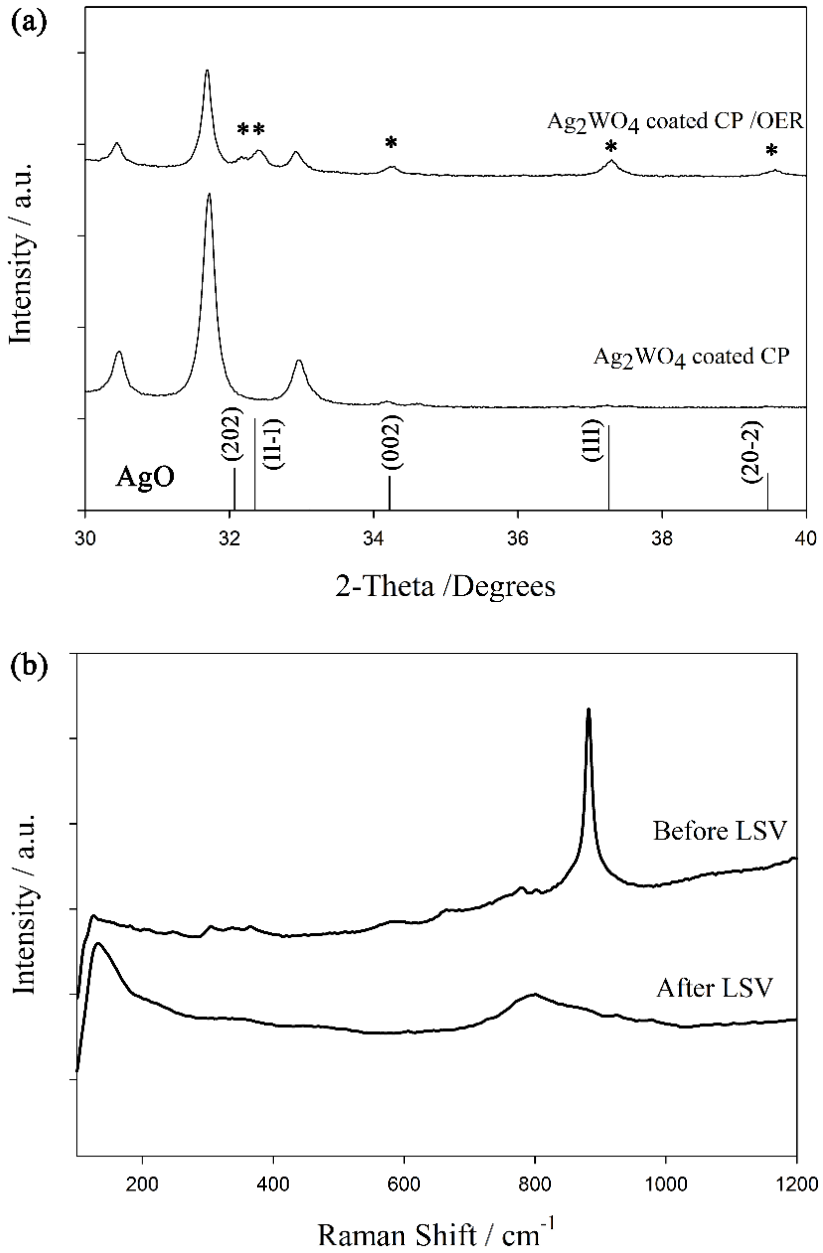

Figure 4.22 (a) The XRD spectra of Ag_2WO_4 loaded carbon paper (CP), Ag_2WO_4 loaded CP after LSV in OER range; (b) Raman spectra of α- Ag_2WO_4 powders before and after LSV.

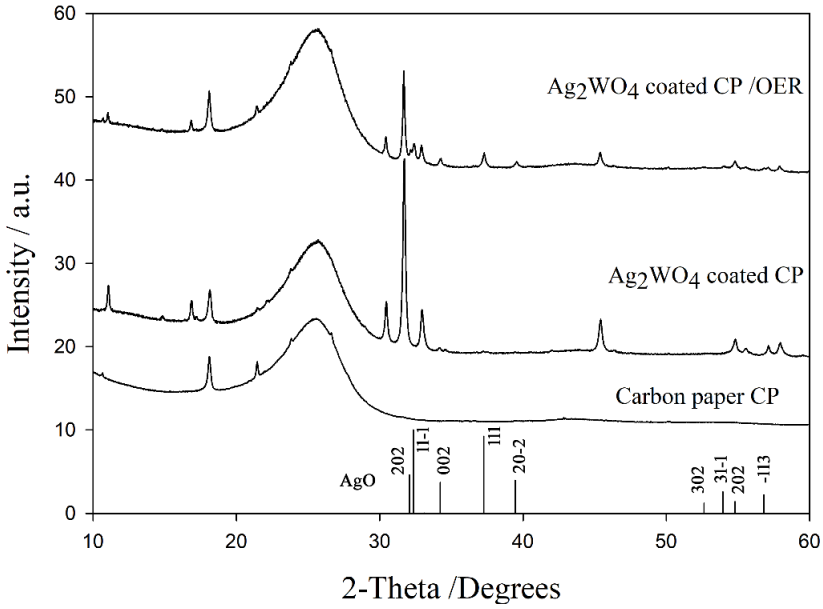

Figure 4.23 The XRD spectra of carbon paper (CP), Ag_2WO_4 loaded CP, Ag_2WO_4 loaded CP after LSV in the OER range.

In brief, the results presented herein clearly revealed that the hydrothermally synthesized Ag_2WO_4 is a possible ORR catalyst. The onset potential, half-wave potential, limiting current density and potential recorded at -3 mA/cm^2 of which were 930 mV (η_0=300 mV), 710 mV, 5 mA cm_{geo}^{-2} and 690 mV (η_3=540 mV), respectively. The ORR kinetics, especially mass normalized current density can be enhanced by increasing surface area and changing morphology of powders. For example, the electrodeposition of Ag_2CrO_4 films on a silver surface has been reported [120], which can be utilized for the direct growth of catalyst material on the current collector. Extended cycling and the results have been ascribed to the direct growth of catalyst materials on the mesh current collector in the literature [76]. Therefore, different production methods could be tried to enhance the promising ORR kinetics of these Ag-based oxides. However, observed peaks before the oxygen evolution reaction and high overpotential (670 mV) at 10 mA cm^{-2} current density in the OER range demonstrate that kinetics of Ag_2CrO_4, Ag_2MoO_4 and Ag_2WO_4 powders were not sufficient to be an OER catalyst.

4.3 Results of Cu-based Delafossites, $CuXO_2$ (X= Cr and Co)

XRD method was firstly used to determine the crystal structures of the produced delafossite powders. The XRD spectra of powders and the peak positions of the corresponding phases can be seen in Figure 4.24. Peak positions of the powder obtained at cobalt experiment coincide with the peak position of the $CuCoO_2$ phase (ICDD Card number: 21-0256) as seen in Figure 4.24(a). However, impurities, cubic Co_3O_4 (ICDD 78-1970) and monoclinic CuO (ICDD 48-1548) phases, were found in small amounts. The XRD spectra of the powders obtained at $CuCrO_2$-H210 and $CuCrO_2$-H230 conditions were corresponding to a mixture of 3R (ICSD 402290) and 2H (ICSD 402289) polymorphs of $CuCrO_2$. XRD data of these polymorphs were difficult to be distinguished due to the close peak positions and small particle size (broadening of peaks). Peak positions of powders obtained at experiment $CuCrO_2$-H230 were similar to $CuCrO_2$-H210. Similar XRD data was obtained by Kaya et al. [88], peaks of which were indexed to the 3R structure of $CuCrO_2$. Peak positions of the powder obtained at experiment $CuCrO_2$ sol-gel coincide with the peak positions of the 3R polymorph of $CuCoO_2$ phase. Small peaks of $CuCr_2O_4$ were also observed.

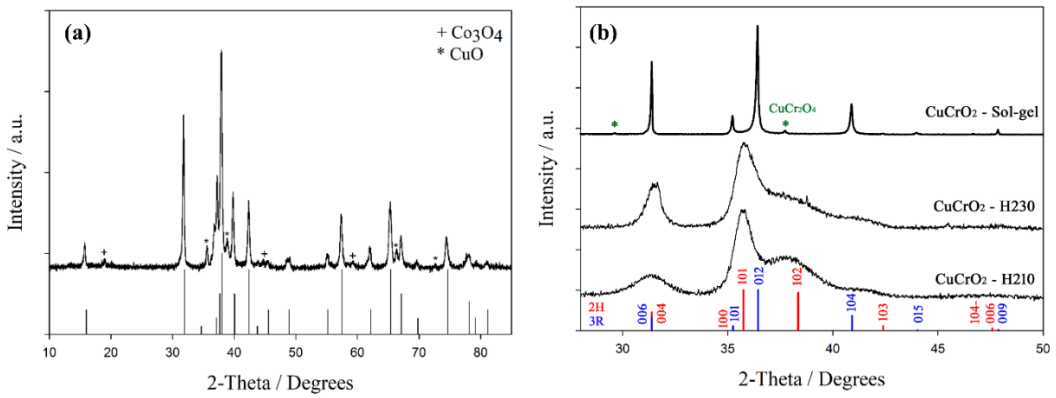

Figure 4.24 The XRD spectra of powders synthesized through (a) $CuCoO_2$, (b) $CuCrO_2$, $CuCrO_2$-H210 and $CuCrO_2$-H230 experiments.

SEM micrographs of $CuCoO_2$ and $CuCrO_2$ powders at different magnifications were given in Figure 4.25. The SEM image of hydrothermally produced $CuCoO_2$ powder is in good agreement with the literature [87], [121]. Hexagonal plates of different sizes can be seen in Figure 4.25(a). SEM micrographs of $CuCrO_2$ synthesized through sol-gel and hydrothermal methods (at different temperatures; 210 and 230 ^oC), given in Figure 4.25(b,c,d) respectively, revealed distinct differences. Especially, the particle size of the $CuCrO_2$ powders obtained via the sol-gel method is in the micron range, as seen in Figure 4.25(b). On the other hand, SEM images of $CuCrO_2$ powders prepared with the hydrothermal process at 210 and 230 ^oC temperatures revealed that powders having homogeneous and fine microstructures were produced. However, agglomerated nanoparticles can also be seen in Figure 4.25(c,d).

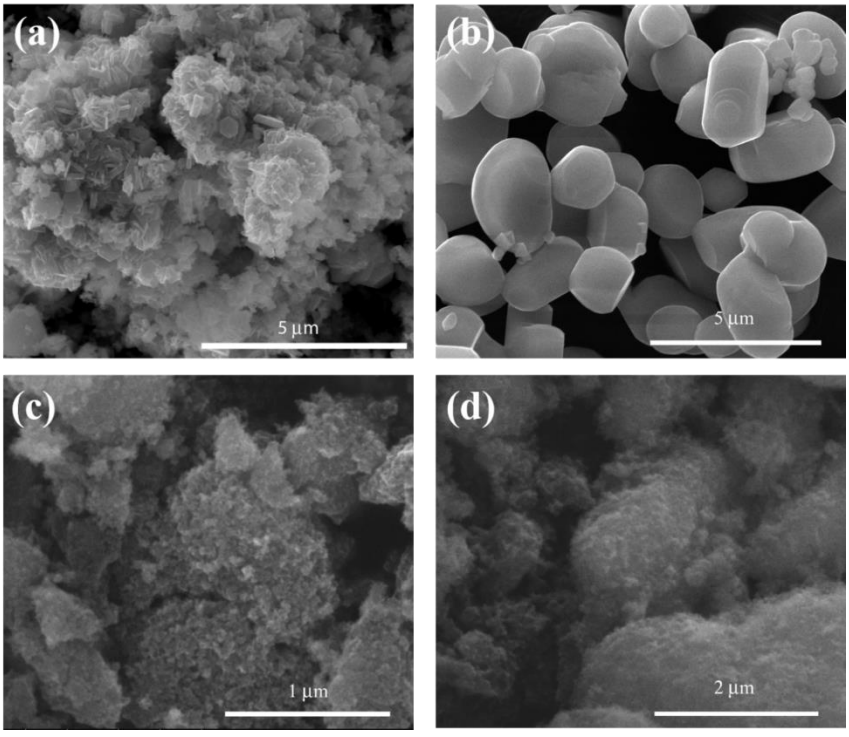

Figure 4.25 SEM images of (a) $CuCoO_2$ obtained via hydrothermal method, (b) $CuCrO_2$ obtained via sol-gel method, (c) $CuCrO_2$ obtained via hydrothermal method at 210 ^oC, (d) $CuCrO_2$ obtained via hydrothermal method at 230 ^oC.

To gain insights into the ORR activity of synthesized powders, polarization studies were recorded in O_2 purged 0.1 M KOH electrolyte at 1600 rpm. Rotating-disk voltammograms of $CuCoO_2$ and $CuCrO_2$ powders produced via sol-gel and hydrothermal methods and bare glassy carbon surface can be seen in Figure 4.26. To obtain the current density, geometric area of the glassy carbon surface (0,19635 cm^2) was used. Results point out that hydrothermally synthesized $CuCoO_2$ and $CuCrO_2$ (at 210 ^oC) have similar onset and half-wave potentials. Moreover, effect of particle morphology can be seen from the results of $CuCrO_2$ oxides, which were synthesized by sol-gel and hydrothermal methods. The higher the particle size, the lower the onset potential for ORR. Indeed, decreasing the particle size increased the number of active sites on the working electrode. However, onset potentials of delafossite oxide loaded RDE were very far away from the onset potential of 67 wt % Pt/C and synthesized α-MnO_2 oxides. The difference between the onset potentials is between the 200 and 300 mV. Results also pointed out that two plateaus were observed for copper delafossite oxides whereas a limiting current was observed for α-MnO_2 and Pt/C powders. Plateaus with different inclined angles were ascribed to the nonuniform distribution of active site on the RDE and/or formation of byproducts [122].

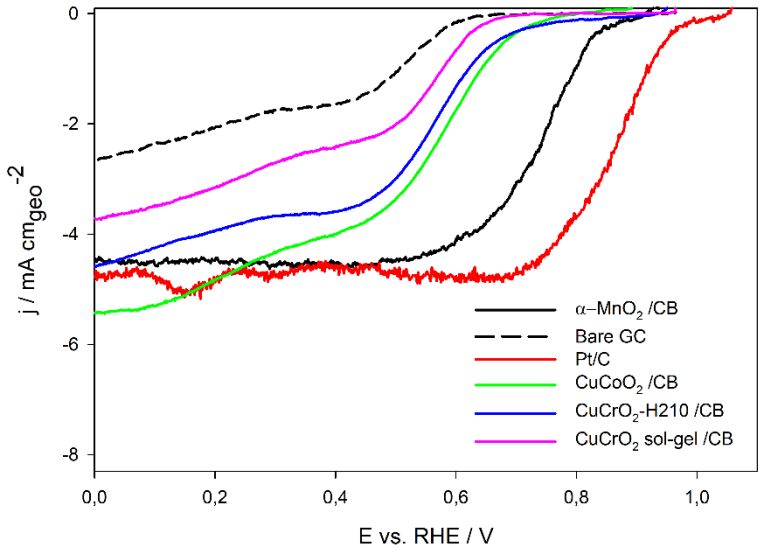

Figure 4.26 Rotating-disk voltammograms of α-MnO_2, Pt/C, $CuCoO_2$, $CuCrO_2$ (obtained at H210 experiment) and $CuCrO_2$ (synthesized at sol-gel experiment) loaded and bare glassy carbon working electrode in O_2 purged 0.1 M KOH aqueous electrolyte with a sweep rate of 5 mV/s at 1600 rpm.

Koutecky–Levich (K–L) plots, given in Figure 4.27(b,d), were enabled us to calculate the average electron transfer number for the oxygen reduction reaction from the slope of 1/j versus $1/\omega^{1/2}$ graph. Koutecky-Levich plots of hydrothermally synthesized $CuCrO_2$ and $CuCoO_2$ were obtained at 0, 0.2, 0.4, 0.5 and 0.6 (vs. RHE) at various rotation speeds of RDE. In the literature, there is a significant effort to find oxygen electrode catalysts that follow the 4-electron transfer pathway. The electron transfer numbers (n) of $CuCrO_2$ at these potentials were approximately calculated as 4.1 with the exception of 4.6 which was obtained at 0.6 V RHE. The electron transfer numbers (n) of $CuCoO_2$ at 0, 0.2, 0.4, 0.5 and 0.6 V RHE were approximately calculated as changing from 4.5, 4.3, 3.46, 3.39 and 2.5, respectively. The electron transfer numbers of these powders are close to 4, which means that these powders might be a candidate to favor a 4 e^- oxygen reduction process; however, onset potential, half-wave potentials were far away from that of commercial 67 wt% Pt/C catalyst. Furthermore, H_2O_2 yield percent should be determined by rotating ring disc electrode because reactions could occur via $4e^-$ or $2e^- + 2e^-$ pathways. Measured disc

current was the combination of reduction current of O_2 and current of byproducts. Moreover, the calculated electron transfer number of $CuCoO_2$ oxide at more negative potential is above $4e^-$, which might be ascribed to the occurrence of another reaction. As seen from the graph, current density increased at more negative potentials, which were already seen in Pt/C powders. In literature, reactions at approximately at these potentials were ascribed to the hydrogen oxidation/evolution [123], dramatic current increase after 0 V RHE was absent for other oxides rather than $CuCoO_2$ powder. Even though various catalyst can be found for hydrogen evolution reaction (HER) in acidic media, researchers try to find a candidate catalyst for HER in alkaline medium because of the advantages of using alkaline electrolytes such as obtaining pure $H_2(g)$, having better stability of materials and avoiding corrosion [124]. The HER activity results of $CuCoO_2$ in this research can be used to inform other future research.

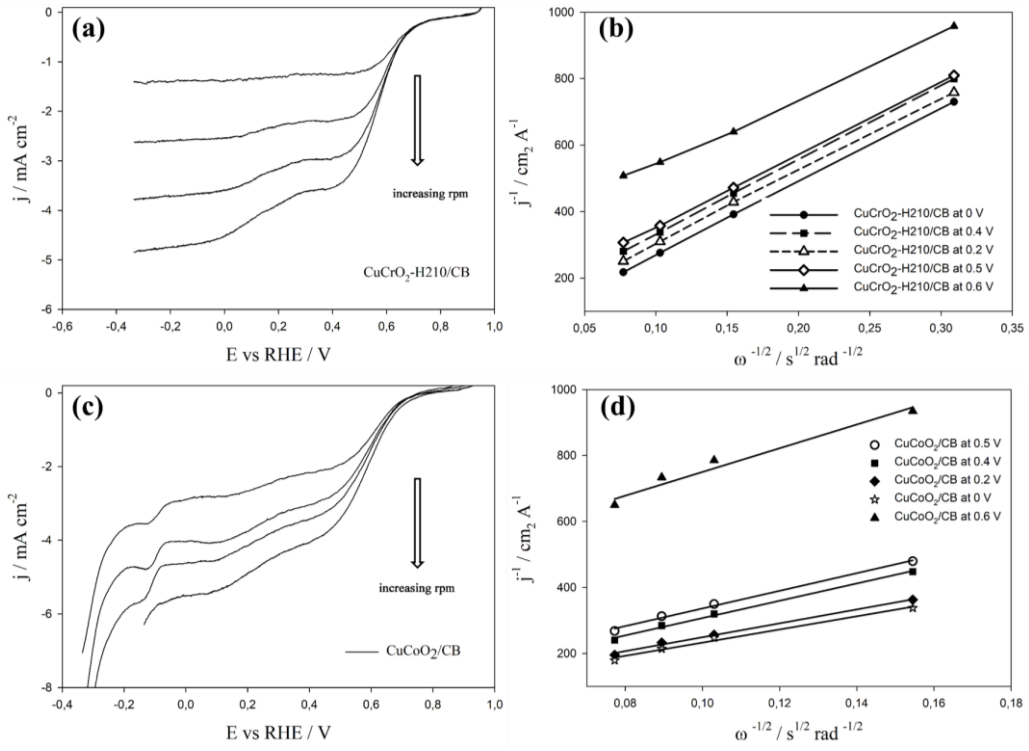

Figure 4.27 Rotating-disk voltammograms and K-L plots of (a,b) $CuCrO_2$ (synthesized through hydrothermal method at 210 ^oC) and (c,d) $CuCoO_2$ oxides. Rotating-disk voltammograms were recorded in O_2 purged 0.1 M KOH aqueous

electrolyte with a sweep rate of 5 mV/s at different rotation rates. K-L plots were drawn at 0, 0.2, 0.4, 0.5 and 0.6 V RHE.

To gain insights into the oxygen evolution reaction (OER) activity of synthesized powders, polarization studies were recorded in O_2 purged 0.1 M KOH electrolyte at 1600 rpm. Rotating-disk voltammograms of $CuCoO_2$ and $CuCrO_2$ powders produced via sol-gel and hydrothermal methods and bare glassy carbon surface can be seen in Figure 4.28. OER activities of these powders were quite different even though ORR activities of that were quite close to each other. There was a dramatic increase in the current density of the working electrode loaded with the powders after a certain potential (E_{onset}) with respect to bare glassy carbon electrode surface. The onset potential of OER reaction for $CuCoO_2$, $CuCrO_2$ sol-gel, $CuCrO_2$-H210 and $CuCrO_2$-H230 was 1.6, 1.6, 1.65 and 1.65 V (vs. RHE), respectively. In other words, onset potentials were quite similar to each other, which can be seen in Figure 4.28. Even though the onset potential of OER on the $CuCrO_2$ loaded working electrode was slightly more positive than that of WE loaded with $CuCrO_2$-H210, the current density of later increased faster after the overpotential of 340 mV. Moreover, voltages recorded at 10 mA cm^{-2} current densities were compared because of being a good indicator for the oxygen evolution reaction activity of produced powders, which is widely used in the literature [87]. The measured overpotential at 10 mA cm^{-2} current density for $CuCoO_2$, $CuCrO_2$ sol-gel, $CuCrO_2$-H210 and $CuCrO_2$-H230 was 520, 530, 580 and 600 mV, respectively, as seen in Figure 4.28. Moreover, 10 mA cm^{-2} current density cannot be achieved at 67 wt % Pt/C loaded working electrode. Passivation of carbon supported platinum in alkaline media was reported. The dissolution, coalescence/agglomeration of Pt particles was reported elsewhere [125].

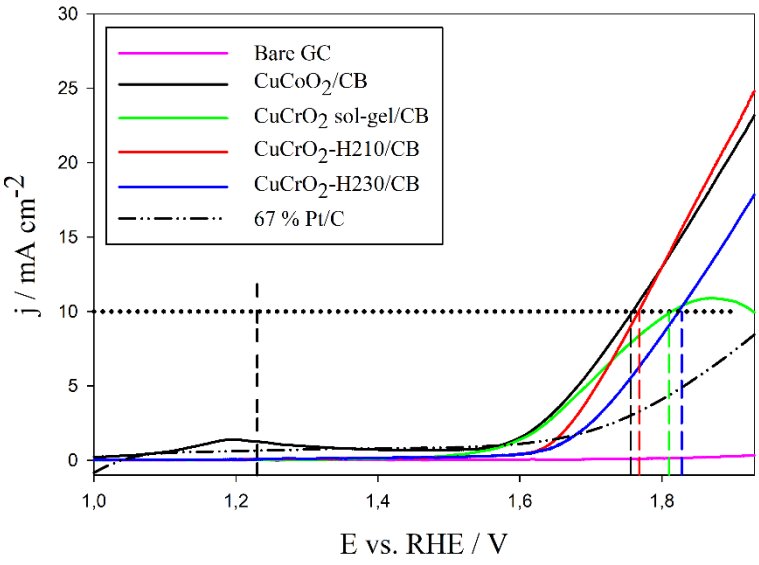

Figure 4.28 Rotating-disk voltammograms of $CuCoO_2$ and $CuCrO_2$ powders loaded and bare glassy carbon working electrode in O_2 purged 0.1 M KOH aqueous electrolyte with a sweep rate of 5 mV/s. The equilibrium potential for OER reaction (E^o =1.23 V vs. RHE) and recorded potentials of each oxide at 10 mA cm^{-2} were shown by dotted lines.

Du and coworkers were also tried to synthesize $CuCoO_2$ with low temperature hydrothermal method, where the production method was taken as an example for this study, the same overpotential (η_{10}=500 mV) was recorded with similar microstructures [87]. Moreover, according to the results of research showing the activity of hydrothermally synthesized micron sized $CuCoO_2$ for OER in alkaline media, similar overpotential (η_5=430 mV) was recorded [126]. In order words, data taken from the literature were similar to that of synthesized $CuCoO_2$ catalyst [87], [126]. Therefore, synthesized $CuCoO_2$ was used as a benchmark to compare other powders under the same conditions.

Some researchers investigated the activity of copper and silver delafossites. Even though the activities of $CuMnO_2$ and $CuCrO_2$ are low according to some studies (recorded onset potentials for $CuMnO_2$ and $CuCrO_2$ were approximately 1.85 and 1.95 V) [126], in 2019, L. Mao et. al. stated that $CuMnO_2$ is a promising catalyst for OER [127]. In 2018, $CuCoO_2$ was investigated for OER kinetics, which revealed that

440 mV overpotential was achieved at 10 mA cm^{-2} [87]. In 2019, Xiong and co-workers were tried to obtain $CuCoO_2$ nanoplates to enhance the OER activity. These nanoplates obtained by modified hydrothermal synthesis had a very low overpotential (η_{10} = 390 mV) with a low Tafel slope of 70 mV dec^{-1} [121]. Even though copper delafossites have been studied, there are very few studies about the activity of $CuCrO_2$ for OER; moreover, some of those have reported the high overpotential (η_5=710 mV) [126]. On the other hand, some of the research pointed out the opposite trend in activity [128]. However, in these researches, particle sizes of the powders were very different, which might be the main reason for low activity of $CuCrO_2$. Indeed, solid-state reactions were used and bigger particles were obtained. In this study, the OER kinetics of the $CuCrO_2$ was quite similar to the $CuRhO_2$, $CuGaO_2$ and $CuCoO_2$ oxides, which are the researched OER catalysts in the literature, this might be the evidence to be a good OER catalyst candidate. In the literature, research focused on investigating the OER activity of these compounds revealed that remarkable activity was observed for $CuRhO_2$, $CuGaO_2$ and $CuCoO_2$ oxides [55], [126], [129]. Theoretical calculations were done to find the relation between these compounds and the OER activity [126]. Onset potential of approximately 1.65 V, were recorded for both $CuRhO_2$ and $CuCoO_2$, which were very close to the state of art catalysts, Co_3O4 [126].

The surface area data obtained by BET was coherent with the morphological analysis. The surface area decreased following the order of $CuCrO_2$-H210 > $CuCrO_2$-H230 > $CuCoO_2$ > $CuCrO_2$ sol-gel with the following values: 143 > 92 > 12 > 0.9 $m^2 g^{-1}$, respectively. These data were also in good agreement with the current densities of $CuCrO_2$ catalysts obtained by rotating disc voltammograms, especially after 10 mA cm^{-2}. Even though the onset potential for the OER at $CuCrO_2$ obtained by sol-gel was same as that of $CuCoO_2$, current density dramatically decreased after this current density. Most probably, the catalyst was no longer resistant to high current densities due to the low surface area and low amount of available catalytic active sites. Furthermore, as can be seen in Figure 4.28, the current density of $CuCrO_2$-H210 caught the value of $CuCoO_2$ at 10 mA cm^{-2} and its value went above

slightly. In other words, $CuCrO_2$ catalysis which was not so emphasized can be compared with well-known catalysts when their surface area was reduced.

Hydrothermally produced $CuCrO_2$ powders having the same particle morphology were investigated further (See Figure 4.29) by specific current density. As seen from the graph, the voltammograms of two catalysts sat on top of each other. In other words, obtained current densities were equal when surface areas of the oxides were taken into account. In addition to the specific activities, as seen in Figure 4.30, mass activities (mA mg^{-1}) of catalysts including commercial Pt/C catalyst were also compared because of being an important parameter in evaluating the activity of the catalyst. The mass activity of each catalyst at 1.55 and 1.9 V (vs. RHE) were shown in a bar chart Figure 4.30(b).-Commercial Pt/C catalyst was the most active one at 1.55 V vs. RHE. The trend in the OER activity, however, was changed at higher oxidation potentials. Again, the mass activity trend was in correlation with the previously reported data. At overpotential of 670 mV, mass activity values in the following sequence: $CuCrO_2$-H210 > $CuCoO_2$ > $CuCrO_2$-H230 > Pt > $CuCrO_2$ sol-gel with the following values: 88, 81, 64, 48, 42 mA mg^{-1}, respectively. Even though hydrothermally produced powders have similar microstructures and phases, the mass activity of $CuCrO_2$-H210 was approximately 1.5 times higher than that of $CuCrO_2$-H230, which might be attributed to the difference in the surface area. The mass activity of $CuCrO_2$-H210 catalyst at 760 mV overpotential was recorded as 125 mA mg^{-1} (with mass loading of 0.25 mg cm^{-2}), which was closed to that of the RuO_2 (165 mA mg-1 with mass loading of 0.4 mg cm^{-2}) at same overpotential [89]. The mass activity of each catalyst actually should be further analyzed because of the interaction between the catalyst loading and mass activity [130]. The optimization of loading should be performed before the usage of these catalysts.

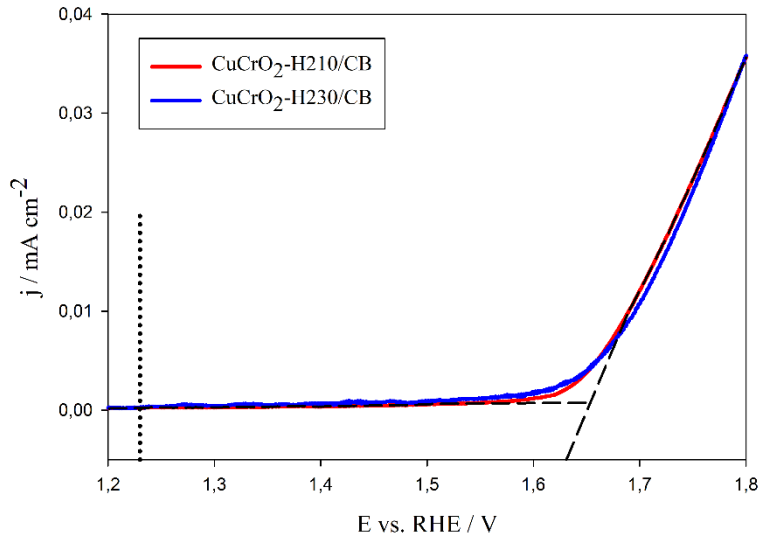

Figure 4.29 Specific activities of $CuCrO_2$ oxides synthesized through hydrothermal reaction at 210 and 230 ºC.

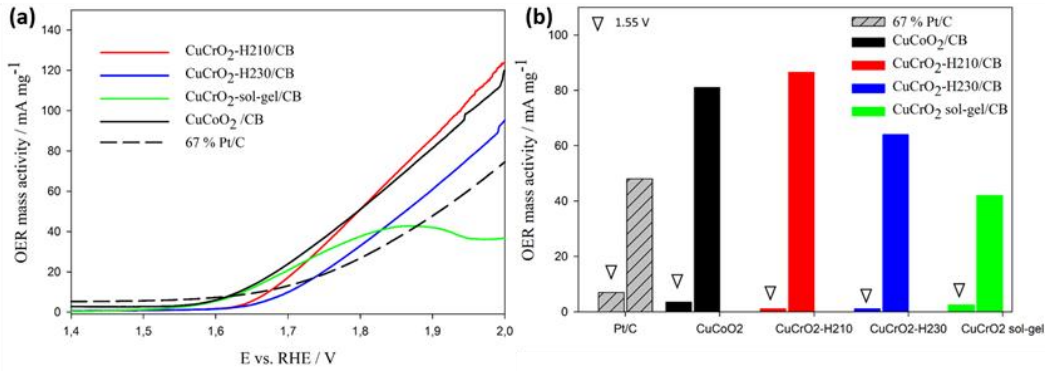

Figure 4.30 (a) Mass activities of synthesized copper delafossites with carbon black mixture and commercial 67 wt% Pt/C. (b) Bar chart of mass activities synthesized copper delafossites with carbon black mixture and commercial 67 wt% Pt/C at 1.55 and 1.9 V RHE.

To gain a deeper insight into the OER activities, Tafel slopes, chronoamperometry test, voltammograms before and after the chronoamperometry test and linear sweep voltammograms on gas diffusion layer in 6 M KOH were investigated, which can be seen in Figure 4.31 (a-d). Tafel plots of the $CuCrO_2$, $CuCoO_2$ and commercial Pt/C

powders obtained at the low overpotential region of OER can be seen in Figure 4.31(a). The results of promising $CuCrO_2$ catalyst candidates were compared with that of synthesized $CuCoO_2$ and 67 wt% Pt/C powders. The slope of the Tafel plot has enabled us to gain information about the OER kinetics. Tafel slopes of $CuCrO_2$-H210 and $CuCoO_2$ catalyst were 85 and 147 mV dec^{-1}, respectively. The lower Tafel slope of $CuCrO_2$-H210 indicated the more favorable OER kinetics with respect to $CuCoO_2$. Moreover, Tafel slope of powders obtained at $CuCrO_2$-H210 experiment is close to the well-known OER catalysts RuO_2 (90 mV dec^-1) and IrO_2 (82 mV dec^{-1}) [131], [132].

The stabilities of $CuCrO_2$ and $CuCoO_2$ catalyst candidates were investigated by chronoamperometry test. The chronoamperometric response of these oxides was obtained at 1.7 V RHE in O_2 purged 0.1 M KOH solution. Obtained relative current versus time graph seen in Figure 4.31 (b), revealed that $CuCoO_2$ retained 75 % of its initial current density after 8300 seconds at a high oxidation potential of 1.7 V. However, $CuCrO_2$ powder synthesized at 210 C only retained 50 % of its initial current density after approximately 1.5 hours. Linear sweep voltammetry was also performed before and after the chronoamperometry test. As can be seen in Figure 4.31(c), there was no noticeable change in the linear sweep voltammogram of $CuCoO_2$ that points out the good durability of $CuCoO_2$ in the alkaline environment. Even though linear sweep voltammogram of $CuCoO_2$ and $CuCrO_2$ were quite close to each other before the test, as can be seen in Figure 4.31(c), there was a drastic voltage decrease after the chronoamperometry test. In other words, a noticeable change in the linear sweep voltammogram points out the bad durability of $CuCrO_2$ in the alkaline environment.

$CuCrO_2$ powders were also loaded on gas diffusion layer and voltammograms were recorded in an in-house made setup which was filled with 6M KOH (See Figure 4.31 (d)) because high concentrations were used in metal-air batteries. The overpotential at 10 mA cm^{-2} current density was also used as a figure of merit. After spray coating of powders on carbon paper, it was cut to 1.54 cm^2 and placed. The Luggin capillary was used to decrease the ohmic drop due to the electrolyte resistance to the

minimum. LSV was recorded in O_2 purged 6 M KOH electrolyte. Commercially taken Pt-Ru loaded carbon paper was also used to compare the electrochemical activity. Geometric area normalized current densities of both catalysts can be seen in Figure 4.31 (d). The mass loading of $CuCrO_2$-H210 powders on carbon paper was 2 mg cm^{-2} to compare with the Pt-Ru loaded GDL (1+1 mg cm^{-2}). Even though mass loading of $CuCrO_2$ powders on carbon paper is higher than RDE, onset potentials were similar on $CuCrO_2$ loaded carbon paper and RDE in 0.1 and 6 M KOH electrolyte, respectively. In addition, though the onset potential of Pt-Ru catalyst was lower than the $CuCrO_2$, the increasing rate of current density after onset potential was higher for $CuCrO_2$. After the 720 mV overpotential, current density of the latter passed to the commercial Pt-Ru catalyst loaded gas diffusion layer.

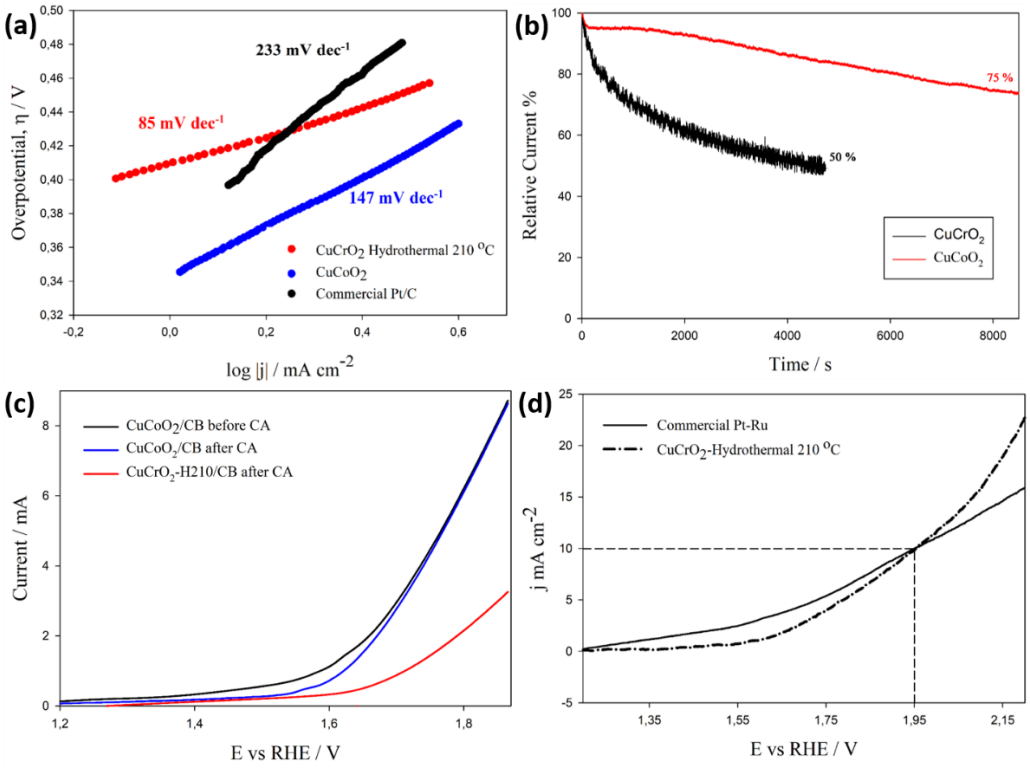

Figure 4.31 (a) Tafel plots of synthesized copper delafossites $CuCrO_2$, $CuCoO_2$ with carbon black mixture and commercial 67 wt% Pt/C; (d) Chronoamperometry curves of $CuCrO_2$, $CuCoO_2$ powders obtained at 1.7 V vs. RHE; (e) Linear sweep voltammograms of $CuCrO_2$, $CuCoO_2$ powders before and after the

chronoamperometry test; (f) Linear sweep voltammogram of $CuCrO_2$ powders and commercial Pt-Ru powders loaded on gas diffusion layer for OER range.

Nyquist plots of EIS patterns of $CuCrO_2$ and $CuCoO_2$ samples at 1.7 RHE were given in Figure 4.32(a) where the inserts show the equivalent circuits used in fitting. The circuit consists of electrolyte resistance (R1, R_{EL}), double-layer capacitance (Q1, constant phase element 1), charge transfer resistance (R2, Rct), adsorption pseudocapacitance of reaction intermediates (Q2, constant phase element 2) and resistance imposed by reaction intermediates (R3, Rads). The combination of Rct and Rads gives the faradic resistance of the catalyst. Moreover, these resistances can be attributed to the properties of more than one step in the overall reaction [133]. According to the fitting results, Rct and Rads values of $CuCrO_2$ sample were recorded as 37.2 and 58.5 Ohm, respectively. Besides, Rct and Rads values of $CuCoO_2$ sample were found as 20 and 18.7 Ohm, respectively. EIS data are coherent with the voltammogram obtained at LSV experiment. Faradic resistance of $CuCoO_2$ sample was lower than that of $CuCrO_2$ at 1.7 V RHE working electrode potential. Nyquist plots of EIS patterns of $CuCrO_2$ samples at different working potentials of 1.2, 1.6, 1.665 and 1.7 V RHE can be seen in Figure 4.32(b) that points out the dramatic decrease in the faradic resistance when overpotential is increased especially after the onset potential of OER on $CuCrO_2$ sample.

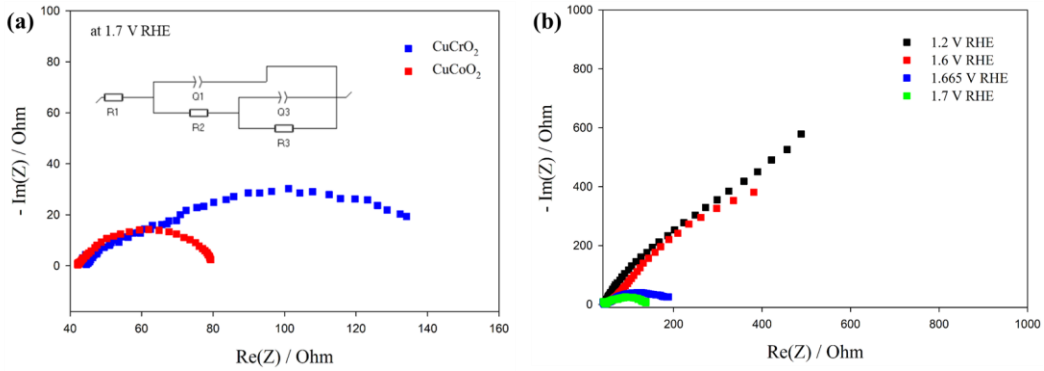

Figure 4.32 (a) EIS spectra of $CuCrO_2$ and $CuCoO_2$ samples at 1.7 RHE. Insert show the equivalent circuits used in fitting. (b) EIS spectra of $CuCrO_2$ samples at working potentials of 1.2, 1.6, 1.665 and 1.7 V RHE.

To investigate the microstructures, $CuCrO_2$ powders loaded on the gas diffusion layer was structurally characterized before and after holding at oxidizing potentials. The difference in the microstructures before and after the chronoamperometry test was investigated to see the effect of holding at oxidizing potentials, which adversely affect the acquired current density during the chronoamperometry test. However, microstructures of sprayed $CuCrO_2$ powders, after the experiment, point out that there is not a drastic change in form. The decreasing the activity of catalysts were generally ascribed to the disintegration of catalysts powder during the oxygen evolution. Besides, dissolution of some powders and/or agglomeration might be one of the reasons for decreasing activity OER range [134]. In literature, similar behavior was observed in the OER range for IrOx nanoparticles. During the stability test of these powders, agglomeration of nanoparticles and detachment of the largest ones were ascribed as the predominant degradation mechanism [134]. Identical location transmission electron microscopy (IL-TEM) was used to study the changes in form of catalysts as a result of electrochemical applications. The same method was used in another research to point out the migration of Pt particles during catalyst activity measurements [135].

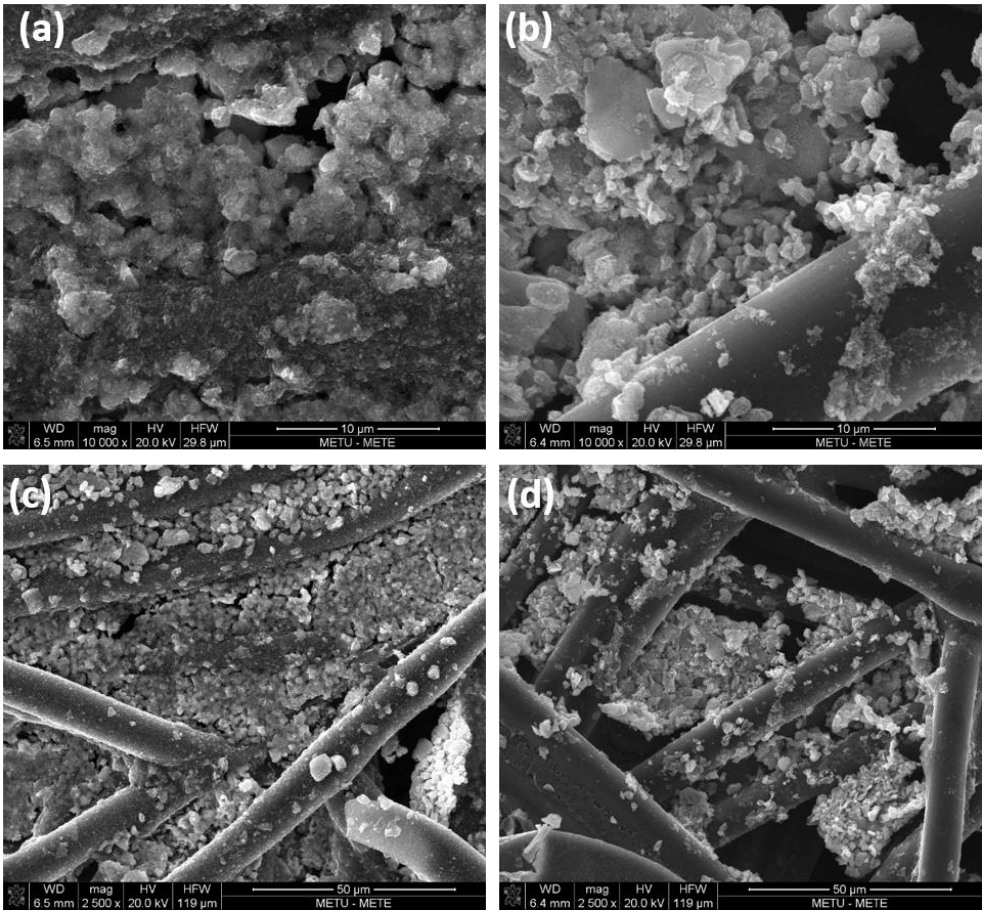

Figure 4.33 SEM micrographs of $CuCrO_2$ coated gas diffusion layer (a, c) before and (b, d) after holding at 1.7 V vs. RHE for 1.5 hours.

To investigate reactions that occurred in the OER region, XRD spectra of $CuCrO_2$ loaded carbon paper were compared before and after the chronoamperometry test (See Figure 4.34). After holding at 1.7 V RHE for 1.5 hours, broad XRD peaks of $CuCrO_2$ changed and peaks became sharper even though peak positions were the same. However, new peaks with low intensity were observed. Peaks at 48.91°, 61.73°, 66.30° and 68.20° 2Theta coincided with the peaks of CuO powder (Card no:96-101-1195). The broad peak at 43.57° 2Theta was also observed at bare carbon paper; thus, it was not searched.

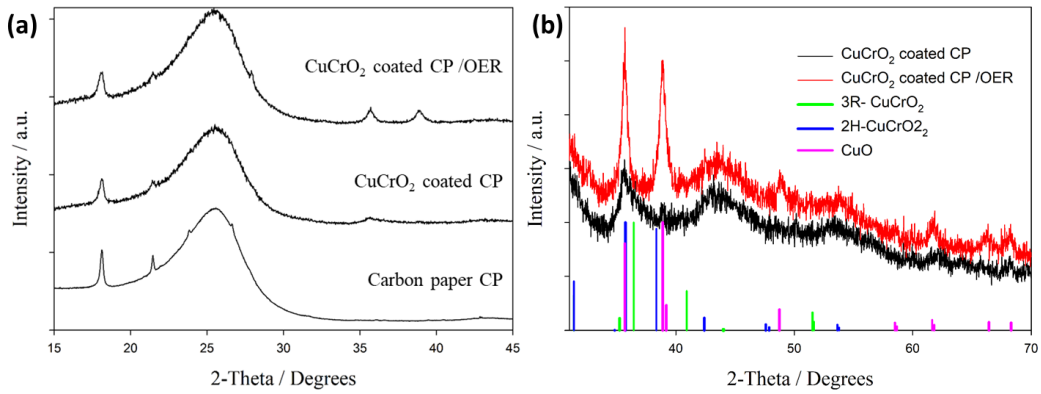

Figure 4.34 (a) The XRD spectra of carbon paper, $CuCrO_2$ loaded carbon paper, $CuCrO_2$ loaded carbon paper after holding at 1.7 V vs. RHE for 1.5 hours (b) The enlarged version of the XRD spectra of $CuCrO_2$ loaded carbon paper, $CuCrO_2$ loaded carbon paper between 30-70^o degrees. Straight lines belong to the peak positions of 3R and 2H $CuCrO_2$, and CuO.

The XRD spectra of $CuCrO_2$ powder loaded carbon paper after holding at 1.7 V vs. RHE for 2.5 hours and $CuCrO_2$ powders can be seen in Figure 4.35. Peak positions of powders on the GDL did not change, which pointed out the stability of this powder while holding at 1.7 V oxidative potential. Even though relative current density was decreased to 75 % after chronoamperometry test, formation of oxides was not observed that pointed out the resistance of $CuCoO_2$ oxides to high oxidation potential.

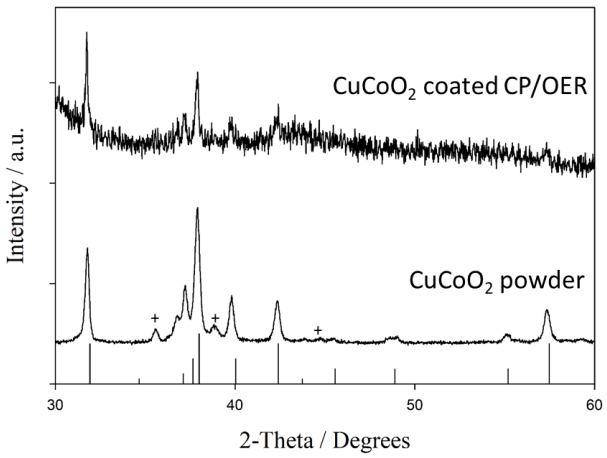

Figure 4.35 The XRD spectra of $CuCrO_2$ powder loaded carbon paper after holding at 1.7 V vs. RHE for 2.5 hours and $CuCrO_2$ powder. Straight lines belong to the peak positions of 3R $CuCoO_2$.

In brief, the results presented herein clearly revealed that the hydrothermally synthesized $CuCrO_2$ and $CuCoO_2$ have a high OER activity in the alkaline medium whereas observed voltammograms in the ORR range demonstrate that onset potential and half-wave potentials were not good to be an efficient ORR catalyst. The onset potential, Tafel slope and overpotential at 10 mA cm^{-2} current density for $CuCrO_2$ were recorded as 1.65 V RHE (η_0=420 mV), 85 mV dec^{-1} and 580 mV (η_{10}), respectively. Moreover, 125 mA mg^{-1} mass activity at 760 mV overpotential in 0.1 M KOH with a mass loading of 0.25 mg_{oxide} cm^{-2} was obtained. Even though the activity of $CuCrO_2$ was close to that of $CuCoO_2$, degradation occurred after holding at high oxidation potential for hours. Degradation was reported in literature even for the state of catalysts for OER such as IrOx [134]. Summary of the results and comparison with reported other Cu and Co-based oxides can be seen in Table 4.4.

Table 4.4 Comparison of OER descriptors for synthesized powders with commercial catalysts

Samples	Loading (mg_{cat} cm^{-2})	Onset V (RHE)	η_{10} (mV)	Tafel Slope (mV dec^{-1})	Mass activity (mA mg^{-1})	Electrolyte	Ref.
$CuCoO_2$	0.25	1.60	520	147	81 at η 670 mV	0.1 M KOH	a
$CuCrO_2$ sol-gel	0.25	1.60	530	-	42 at η 670 mV	0.1 M KOH	a
$CuCrO_2$-H230	0.25	1.65	600	-	60 at η 670 mV	0.1 M KOH	a
$CuCrO_2$-H210	0.25	1.65	580	85	88 at η 670 mV	0.1 M KOH	a
Pt/C	0.15	1.63	-	233	70 at η 670 mV	0.1 M KOH	a
Ru-Pt	1-1			-	-	6 M KOH	b
$CuCrO_2$-H210	2	1.95		-	-	6M KOH	b
RuO_2	0.4	1.45	326	60	165 at η 760 mV	0.1 M KOH	[89]
RuO_2	0.2	1.48	387	90	30.2 at η 350 mV	0.1 M KOH	[132]
IrO_2	0.4		530	146		0.1 M KOH	[136]
IrO_2	1.3	-	289	82.2	80 at η 442 mV	1 M KOH	[131]
Co_3O_4	1.3	-	368	75.5	-	1 M KOH	[131]
Co_3O_4-RDE	1	-	500	60.9	-	1 M NaOH	[137]

[a] This work was recorded on GC-RDE, [b] This work was recorded on GDL.

4.4 Results of Homemade Zinc-Air Batteries

Synthesized Ag_2WO_4, $CuCrO_2$ and $CuCoO_2$ were selected to assess long term performance in realistic operating conditions of the zinc-air cell. These powders were selected according to the promising half-cell performances in ORR and OER ranges. A homemade zinc-air battery was assembled as seen in Figure 3.5, cathodes of which was made by loading the catalyst ink on Sigracet GDL (1 mg cm^{-2}). Polarization and corresponding power density curves of Ag_2WO_4, $CuCoO_2$ and $CuCrO_2$ powders can be seen in Figure 4.36(a) that points out the similar trend in polarization in 6 M KOH during discharging. The achieved power density of these powders were approximately 50 mW cm^{-2} at 80 mA cm^{-2}. The power density of Pt/C and RuO_2 mixture was reported as 61.8 mW cm^{-2} in the literature [138]. The open-circuit potentials of the whole cells were also recorded. The measured open-circuit voltage of the Zn-air battery with $CuCrO_2$ loaded air cathode can be seen in Figure 4.36(b). In this study, galvanostatic cycling stability of Zn-air battery with Ag_2WO_4, $CuCoO_2$ and $CuCrO_2$ loaded air electrode at 5 mA cm^{-2} were also conducted. Figure 4.36(c-f) demonstrated different discharge and charge voltages. The change in performance during discharging and charging cycles can also be seen. The difference in the charge voltages points out the better OER activity of $CuCoO_2$. Even though the charging potentials of Ag_2WO_4 and $CuCoO_2$ increased slightly, discharging potential remained at the approximately same level. Besides, galvanostatic cycling stability of $CuCrO_2$ loaded powders were compared with the others. There was a huge change in charging potential especially after 2500 seconds. The change in the behavior can be ascribed to the degradation of $CuCrO_2$ powder. This result consisted with the stability test results.

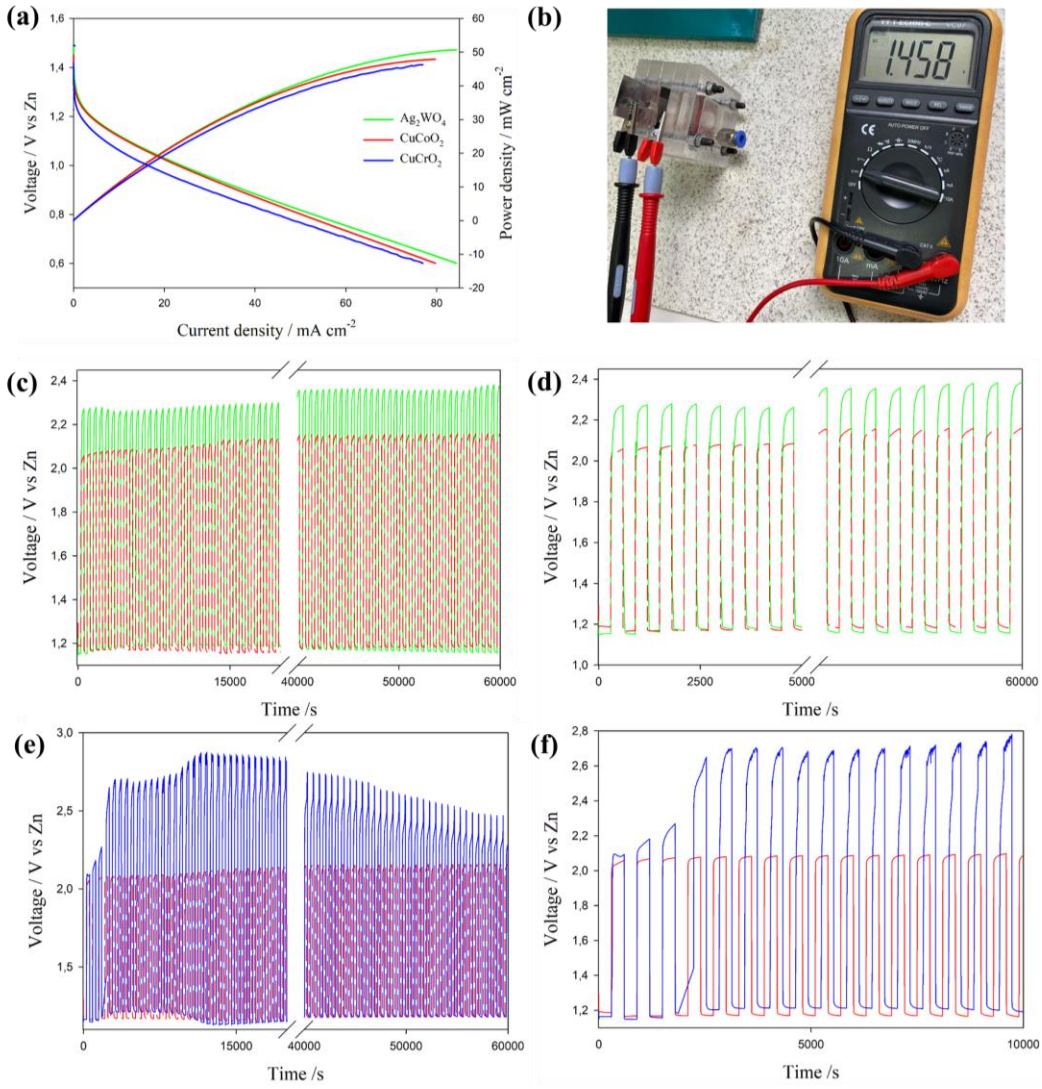

Figure 4.36 (a) Polarization and corresponding power density curves of Ag_2WO_4, $CuCoO_2$ and $CuCrO_2$ powders. (b) Measured open circuit voltage of the Zn-air battery with $CuCrO_2$ loaded air cathode. (c) Galvanostatic cycling stability of Zn-air battery with Ag_2WO_4 and $CuCoO_2$ loaded air electrode at 5 mA cm^{-2}. (d) The enlarged version of first and last cycles of (c). (e) Galvanostatic cycling stability of Zn-air battery with $CuCrO_2$ and $CuCoO_2$ loaded air electrode at 5 mA cm^{-2}. (f) The enlarged version of first cycles of (e). The discharge and charge cycle time of galvanostatic cycling stability is 10 minutes.

CHAPTER 5

CONCLUSIONS

The aim of this study is to produce and characterize a novel catalyst material to be used in the porous air cathode. In this regard, manganese and silver based oxides and copper based delafossite oxides were investigated for ORR and OER activity in the alkaline medium.

Catalyst materials will be produced by spray pyrolysis, co-precipitation, sol-gel and/or hydrothermal methods. The effect of using different oxides on the oxygen reduction and evolution reactions at the catalyst loaded cathode were investigated by electrochemical characterization techniques.

In this study, Ag_2CrO_4, Ag_2MoO_4 and Ag_2WO_4 powders were synthesized through precipitation and/or hydrothermal methods without impurities. The ORR and OER kinetics of these powders were investigated for the first time. Linear sweep voltammograms recorded to see the OER activity of these powders revealed that pre-peaks were present before the onset of oxygen evolution. Even though OER activities of these compounds were not sufficient, the ORR activities were very promising.

Produced powders were investigated by Koutecky-Levich plots, Tafel plots and linear sweep voltammograms on GDL and RDE. Mass and geometric area normalized current densities, electron transfer numbers, Tafel slopes, onset potentials, which are assumed as figures of merit for ORR, were recorded and compared with the well-known catalysts in the literature. The most promising results were obtained from Ag_2WO_4 powders. The onset potential, half-wave potential, limiting current density, Tafel slope and potential recorded at -3 mA cm^{-2} of which were 930 mV (η_0=300 mV), 710 mV, 5 mA cm_{geo}^{-2}, 47 mV dec^{-1}, 690 mV (η_3=540 mV), respectively. Moreover, the electron transfer number (n) of Ag_2WO_4 at 0.365

V was calculated by the help of the Koutecky–Levich (K–L) plots as 3.8. Moreover, Ag_2WO_4 retained 84 % of its initial current density after 20000 seconds at 0.7 V. The results reported in this study revealed that the hydrothermally synthesized Ag_2WO_4 might be a good ORR catalyst. The ORR activity of this compound is similar to the activity of catalysts reported in the literature. Reducing the surface area with different production methods can enhance the ORR kinetics to be used in demanding applications such as metal-air batteries and fuel cells.

The results of copper-based delaffossites presented herein clearly revealed that the hydrothermally synthesized $CuCrO_2$ and $CuCoO_2$ have a high OER activity in the alkaline medium whereas observed voltammograms in the ORR range demonstrate that onset potential and half-wave potentials were not sufficient to be an ORR catalyst. The onset potential, Tafel slope and overpotential at 10 mA cm^{-2} current density for $CuCrO_2$ were recorded as 1.65 V RHE (η_0=420 mV), 85 mV dec^{-1} and 580 mV (η_{10}), respectively. Moreover, 125 mA mg^{-1} mass activity at 760 mV overpotential in 0.1 M KOH with a mass loading of 0.25 mg_{oxide} cm^{-2} was obtained. Even though the activity of $CuCrO_2$ was close to that of $CuCoO_2$, degradation occurred after holding at high oxidation potential.

REFERENCES

[1] M. Prabu, P. Ramakrishnan, H. Nara, T. Momma, T. Osaka, and S. Shanmugam, "Zinc–Air Battery: Understanding the Structure and Morphology Changes of Graphene-Supported $CoMn_2O_4$ Bifunctional Catalysts Under Practical Rechargeable Conditions," *ACS Appl. Mater. Interfaces*, vol. 6, no. 19, pp. 16545–16555, Oct. 2014, doi: 10.1021/am5047476.

[2] K.-B. Wang, Q. Xun, and Q. Zhang, "Recent progress in metal-organic frameworks as active materials for supercapacitors," *EnergyChem*, vol. 2, no. 1, p. 100025, 2020, doi: 10.1016/j.enchem.2019.100025.

[3] A. A. Said, J. Xie, and Q. Zhang, "Recent Progress in Organic Electron Transport Materials in Inverted Perovskite Solar Cells," *Small*, vol. 15, no. 27, pp. 1–23, 2019, doi: 10.1002/smll.201900854.

[4] J. Xie and Q. Zhang, "Recent Progress in Multivalent Metal (Mg, Zn, Ca, and Al) and Metal-Ion Rechargeable Batteries with Organic Materials as Promising Electrodes," *Small*, vol. 15, no. 15, pp. 1–20, 2019, doi: 10.1002/smll.201805061.

[5] W. Yan, X. Cao, R. Wang, Y. Sha, P. Cui, and S. Cui, "S, N co-doped rod-like porous carbon derived from S, N organic ligand assembled Ni-MOF as an efficient electrocatalyst for oxygen reduction reaction," *J. Solid State Chem.*, vol. 275, no. January, pp. 167–173, 2019, doi: 10.1016/j.jssc.2019.04.014.

[6] L. Li, W. Xie, J. Chen, and J. Yang, "ZIF-67 derived P/Ni/Co/NC nanoparticles as highly efficient electrocatalyst for oxygen reduction reaction (ORR)," *J. Solid State Chem.*, vol. 264, no. April, pp. 1–5, 2018, doi: 10.1016/j.jssc.2018.04.035.

[7] M. Tahir *et al.*, “Electrocatalytic oxygen evolution reaction for energy conversion and storage: A comprehensive review,” *Nano Energy*, vol. 37, no. February, pp. 136–157, 2017, doi: 10.1016/j.nanoen.2017.05.022.

[8] B. Liu *et al.*, “Facile synthesis of flower-like dual-metal (Co/Zn) MOF-derived 3D porous Co@Co-NPC as reversible oxygen electrocatalyst for rechargeable zinc-air batteries,” *Ionics (Kiel).*, 2019, doi: 10.1007/s11581-019-03364-z.

[9] Z. Zhang, D. Zhou, L. Zhou, H. Yu, and B. Huang, “NiFe LDH-CoPc/CNTs as novel bifunctional electrocatalyst complex for zinc–air battery,” *Ionics (Kiel).*, vol. 24, no. 6, pp. 1709–1714, 2018, doi: 10.1007/s11581-017-2322-4.

[10] J. S. Lee *et al.*, “Metal-air batteries with high energy density: Li-air versus Zn-air,” *Advanced Energy Materials*, vol. 1, no. 1. John Wiley & Sons, Ltd, pp. 34–50, 01-Jan-2011, doi: 10.1002/aenm.201000010.

[11] A. Tan, M. V. Reddy, and S. Adams, “Synthesis and application of nanostructured MCo2O4(M=Co, Ni) for hybrid Li-air batteries,” *Ionics (Kiel).*, vol. 23, no. 10, pp. 2589–2602, 2017, doi: 10.1007/s11581-016-1913-9.

[12] R. Revel, T. Audichon, and S. Gonzalez, “Non-aqueous aluminium–air battery based on ionic liquid electrolyte,” *J. Power Sources*, vol. 272, pp. 415–421, Dec. 2014, doi: 10.1016/J.JPOWSOUR.2014.08.056.

[13] T. M. Di Palma, F. Migliardini, M. F. Gaele, and P. Corbo, “Physically cross-linked xanthan hydrogels as solid electrolytes for Al/air batteries,” *Ionics (Kiel).*, vol. 25, no. 9, pp. 4209–4217, 2019, doi: 10.1007/s11581-019-02965-y.

[14] Y. Song, J. Ma, Y. Li, G. Wang, C. Qin, and H. R. Stock, “Effects of second phases in anode materials on discharge performance of Mg-air batteries,” *Ionics (Kiel).*, vol. 25, no. 12, pp. 5899–5906, 2019, doi: 10.1007/s11581-019-

03144-9.

[15] Z. Zhou, X. Li, Q. Li, Y. Zhao, and H. Pang, “Copper-based materials as highly active electrocatalysts for the oxygen evolution reaction,” *Mater. Today Chem.*, vol. 11, pp. 169–196, 2019, doi: 10.1016/j.mtchem.2018.10.008.

[16] H. S. Kushwaha, A. Halder, and R. Vaish, “Ferroelectric electrocatalysts: a new class of materials for oxygen evolution reaction with synergistic effect of ferroelectric polarization,” *J. Mater. Sci.*, vol. 53, no. 2, pp. 1414–1423, 2018, doi: 10.1007/s10853-017-1611-7.

[17] K. Harting, U. Kunz, and T. Turek, “Zinc-air batteries: Prospects and challenges for future improvement,” *Zeitschrift fur Phys. Chemie*, vol. 226, no. 2, pp. 151–166, 2012, doi: 10.1524/zpch.2012.0152.

[18] Y. Li and H. Dai, “Recent advances in Zinc-air batteries,” *Chem. Soc. Rev.*, vol. 43, no. 15, pp. 5257–5275, 2014, doi: 10.1039/c4cs00015c.

[19] J. Zhang, Q. Zhou, Y. Tang, L. Zhang, and Y. Li, “Zinc-air batteries: Are they ready for prime time?,” *Chem. Sci.*, vol. 10, no. 39, pp. 8924–8929, 2019, doi: 10.1039/c9sc04221k.

[20] P. Pei, K. Wang, and Z. Ma, “Technologies for extending zinc-air battery’s cyclelife: A review,” *Appl. Energy*, vol. 128, pp. 315–324, 2014, doi: 10.1016/j.apenergy.2014.04.095.

[21] J. Fu *et al.*, “Recent Progress in Electrically Rechargeable Zinc–Air Batteries,” *Adv. Mater.*, vol. 31, no. 31, pp. 1–13, 2019, doi: 10.1002/adma.201805230.

[22] Z. Zhou, X. Li, Q. Li, Y. Zhao, and H. Pang, “Copper-based materials as highly active electrocatalysts for the oxygen evolution reaction,” *Mater. Today Chem.*, vol. 11, pp. 169–196, 2019, doi: 10.1016/j.mtchem.2018.10.008.

[23] C. Daniel, *Handbook of Battery Materials*. 2012.

[24] X. Wang, P. J. Sebastian, M. A. Smit, H. Yang, and S. A. Gamboa, "Studies on the oxygen reduction catalyst for zinc-air battery electrode," *J. Power Sources*, vol. 124, no. 1, pp. 278–284, 2003, doi: 10.1016/S0378-7753(03)00737-7.

[25] J. M. Lee and S. J. Hwang, "Remarkable influence of the local symmetry of substituted 3d metal ion on bifunctional electrocatalyst performance of α-MnO2 nanowire," *J. Solid State Chem.*, vol. 269, no. August 2018, pp. 354–360, 2019, doi: 10.1016/j.jssc.2018.10.009.

[26] K. An, Y. Zheng, X. Xu, and Y. Wang, "Filter paper derived three-dimensional mesoporous carbon with Co3O4 loaded on surface: An excellent binder-free air-cathode for rechargeable Zinc-air battery," *J. Solid State Chem.*, vol. 270, no. November 2018, pp. 539–546, 2019, doi: 10.1016/j.jssc.2018.12.021.

[27] F. Chen, L. Xue, Z. Shang, Z. Zhang, and D. Chen, "An enhanced non-noble perovskite-based oxygen electrocatalyst for efficient oxygen reduction and evolution reactions," *J. Solid State Chem.*, vol. 282, no. November 2019, p. 121119, 2020, doi: 10.1016/j.jssc.2019.121119.

[28] J. Park *et al.*, "Single crystalline pyrochlore nanoparticles with metallic conduction as efficient bi-functional oxygen electrocatalysts for Zn-air batteries," *Energy Environ. Sci.*, vol. 10, no. 1, pp. 129–136, 2017, doi: 10.1039/c6ee03046g.

[29] D. M. Nguyen, L. G. Bach, and Q. B. Bui, "A high-performance catalyst based on binary CuFe alloyed nanocrystals encapsulated in nitrogen-doped graphene nanosheets towards oxygen reduction reaction," *J. Solid State Chem.*, vol. 273, no. February, pp. 132–140, 2019, doi: 10.1016/j.jssc.2019.03.001.

[30] H. Erikson, A. Sarapuu, and K. Tammeveski, "Oxygen Reduction Reaction

on Silver Catalysts in Alkaline Media: a Minireview," *ChemElectroChem*, vol. 6, no. 1, pp. 73–86, 2019, doi: 10.1002/celc.201800913.

[31] E. Longo *et al.*, "Direct in situ observation of the electron-driven synthesis of Ag filaments on α-Ag2 WO4 crystals," *Sci. Rep.*, vol. 3, no. 1, p. 1676, Dec. 2013, doi: 10.1038/srep01676.

[32] L. Wang, H. Xu, J. Gao, J. Yao, and Q. Zhang, "Recent progress in metal-organic frameworks-based hydrogels and aerogels and their applications," *Coord. Chem. Rev.*, vol. 398, p. 213016, 2019, doi: 10.1016/j.ccr.2019.213016.

[33] Y. Li *et al.*, "Enhancing Oxygen Evolution Reaction through Modulating Electronic Structure of Trimetallic Electrocatalysts Derived from Metal–Organic Frameworks," *Small*, vol. 15, no. 43, pp. 1–6, 2019, doi: 10.1002/smll.201901940.

[34] Y. Li, M. Lu, Y. Wu, H. Xu, J. Gao, and J. Yao, "Trimetallic Metal–Organic Framework Derived Carbon-Based Nanoflower Electrocatalysts for Efficient Overall Water Splitting," *Adv. Mater. Interfaces*, vol. 6, no. 12, pp. 1–8, 2019, doi: 10.1002/admi.201900290.

[35] T. N. Huan *et al.*, "A Dendritic Nanostructured Copper Oxide Electrocatalyst for the Oxygen Evolution Reaction," *Angew. Chemie - Int. Ed.*, vol. 56, no. 17, pp. 4792–4796, 2017, doi: 10.1002/anie.201700388.

[36] S. K. Bikkarolla and P. Papakonstantinou, "CuCo2O4 nanoparticles on nitrogenated graphene as highly efficient oxygen evolution catalyst," *J. Power Sources*, vol. 281, pp. 243–251, 2015, doi: 10.1016/j.jpowsour.2015.01.192.

[37] M. P. Araújo, M. Nunes, I. M. Rocha, M. F. R. Pereira, and C. Freire, "Electrocatalytic activity of new Mn 3 O 4 @oxidized graphene flakes nanocomposites toward oxygen reduction reaction," *J. Mater. Sci.*, vol. 54, no. 12, pp. 8919–8940, 2019, doi: 10.1007/s10853-019-03508-6.

[38] X. Ge *et al.*, “Oxygen Reduction in Alkaline Media: From Mechanisms to Recent Advances of Catalysts,” *ACS Catal.*, vol. 5, no. 8, pp. 4643–4667, Aug. 2015, doi: 10.1021/acscatal.5b00524.

[39] X. Jia, Y. Zhang, D. Guo, L. Zhang, L. Wang, and L. Zhou, “CoNx/NiFeOx/nitrogen-doping reduced graphene oxide nanocomposite derived from layered double hydroxide precursor as an efficient bifunctional electrocatalyst for oxygen electrocatalytic reactions,” *Ionics (Kiel).*, 2020, doi: 10.1007/s11581-020-03465-0.

[40] M. A. Rahman, X. Wang, and C. Wenz, “High energy density metal-air batteries: A review,” *Journal of the Electrochemical Society*, vol. 160, no. 10. Electrochemical Society Inc., pp. A1759–A1771, 20-Aug-2013, doi: 10.1149/2.062310jes.

[41] B. B. Blizanac, P. N. Ross, and N. M. Marković, “Oxygen reduction on silver low-index single-crystal surfaces in alkaline solution: Rotating ring diskAg(hkl) studies,” *J. Phys. Chem. B*, vol. 110, no. 10, pp. 4735–4741, 2006, doi: 10.1021/jp056050d.

[42] Y. Liang *et al.*, “Co3O4 nanocrystals on graphene as a synergistic catalyst for oxygen reduction reaction,” *Nat. Mater.*, vol. 10, no. 10, pp. 780–786, Oct. 2011, doi: 10.1038/nmat3087.

[43] J. G. Kim, Y. Kim, Y. Noh, S. Lee, Y. Kim, and W. B. Kim, “Bifunctional Hybrid Catalysts with Perovskite LaCo0.8Fe0.2O3 Nanowires and Reduced Graphene Oxide Sheets for an Efficient Li-O2 Battery Cathode,” *ACS Appl. Mater. Interfaces*, vol. 10, no. 6, pp. 5429–5439, Feb. 2018, doi: 10.1021/acsami.7b14599.

[44] L. Xing, C. Song, and A. Kong, “N–S-codoped mesoporous carbons from melamine-2-thenaldehyde polymers on carbon nanotubes for oxygen reduction and Zn-air batteries,” *J. Solid State Chem.*, vol. 287, no. March, p. 121348, 2020, doi: 10.1016/j.jssc.2020.121348.

[45] A. R. Mainar *et al.*, “Manganese oxide catalysts for secondary zinc air batteries: from electrocatalytic activity to bifunctional air electrode performance,” *Electrochim. Acta*, vol. 217, pp. 80–91, 2016, doi: 10.1016/j.electacta.2016.09.052.

[46] F. Cheng and J. Chen, “Metal–air batteries: From oxygen reduction electrochemistry to cathode catalysts,” *Chem. Soc. Rev.*, vol. 41, no. 6, pp. 2172–2192, 2012, doi: 10.1039/c1cs15228a.

[47] Y. Gorlin, “Development of Manganese Oxide Based Catalysts for the Oxygen Reduction and Oxygen Evolution Reactions,” Stanford University, 2012.

[48] F. W. W. T. Goh, Z. Liu, X. Ge, Y. Zong, G. Du, and T. S. S. A. Hor, “Ag nanoparticle-modified MnO 2 nanorods catalyst for use as an air electrode in zinc-air battery,” *Electrochim. Acta*, vol. 114, pp. 598–604, Dec. 2013, doi: 10.1016/j.electacta.2013.10.116.

[49] S. A. Park, E. K. Lee, H. Song, and Y. T. Kim, “Bifunctional enhancement of oxygen reduction reaction activity on Ag catalysts due to water activation on LaMnO 3 supports in alkaline media,” *Sci. Rep.*, vol. 5, no. 1, p. 13552, Oct. 2015, doi: 10.1038/srep13552.

[50] A. Qaseem, F. Chen, X. Wu, and R. L. Johnston, “Pt-free silver nanoalloy electrocatalysts for oxygen reduction reaction in alkaline media,” *Catalysis Science and Technology*, vol. 6, no. 10. The Royal Society of Chemistry, pp. 3317–3340, 17-May-2016, doi: 10.1039/c5cy02270c.

[51] D. Xu, B. Cheng, J. Zhang, W. Wang, J. Yu, and W. Ho, “Photocatalytic activity of Ag 2 MO 4 (M = Cr, Mo, W) photocatalysts,” *J. Mater. Chem. A*, vol. 3, no. 40, pp. 20153–20166, Oct. 2015, doi: 10.1039/C5TA05248C.

[52] T. I. Draskovic and Y. Wu, “Electrocatalytic Properties of Cuprous Delafossite Oxides for the Alkaline Oxygen Reduction Reaction,” *ChemCatChem*, vol. 9, no. 20, pp. 3837–3842, Oct. 2017, doi:

10.1002/cctc.201700712.

[53] A. Serov, N. I. Andersen, A. J. Roy, I. Matanovic, K. Artyushkova, and P. Atanassov, " CuCo 2 O 4 ORR/OER Bi-Functional Catalyst: Influence of Synthetic Approach on Performance ," *J. Electrochem. Soc.*, vol. 162, no. 4, pp. F449–F454, 2015, doi: 10.1149/2.0921504jes.

[54] R. Hinogami, K. Toyoda, M. Aizawa, T. Kawasaki, and H. Gyoten, "Copper delafossite anode for water electrolysis," in *ECS Transactions*, 2013, vol. 58, no. 2, pp. 27–31, doi: 10.1149/05802.0027ecst.

[55] R. Hinogami, K. Toyoda, M. Aizawa, S. Yoshii, T. Kawasaki, and H. Gyoten, "Active copper delafossite anode for oxygen evolution reaction," *Electrochem. commun.*, vol. 35, pp. 142–145, 2013, doi: 10.1016/j.elecom.2013.08.018.

[56] S. Götzendörfer, "Synthesis of Copper-Based Transparent Conductive Oxides with Delafossite Structure via Sol-Gel Processing," Universität Würzburg, 2010.

[57] Y. Ma *et al.*, "Photoelectrochemical properties of CuCrO2: Characterization of light absorption and photocatalytic H2 production performance," *Catal. Letters*, vol. 144, no. 9, pp. 1487–1493, 2014, doi: 10.1007/s10562-014-1318-1.

[58] Z. Du *et al.*, "Investigation of the structural, optical and electrical properties of Ca2+ doped CuCoO2 nanosheets," *Dalt. Trans.*, vol. 48, no. 36, pp. 13753–13759, 2019, doi: 10.1039/c9dt02619c.

[59] E. Roduner, "Size matters: Why nanomaterials are different," *Chemical Society Reviews*, vol. 35, no. 7. The Royal Society of Chemistry, pp. 583–592, 22-Jun-2006, doi: 10.1039/b502142c.

[60] L. Zhu, D. Huang, J. Ma, D. Wu, M. Yang, and S. Komarneni, "Fabrication of AgBr/Ag 2 CrO 4 composites for enhanced visible-light photocatalytic

activity," *Ceram. Int.*, vol. 41, no. 9, pp. 12509–12513, Nov. 2015, doi: 10.1016/j.ceramint.2015.05.118.

[61] T. B. Reddy and D. Linden, *Linden's handbook of batteries*. New York: McGraw-Hill, 2011.

[62] J. S. Lee *et al.*, "Metal-air batteries with high energy density: Li-air versus Zn-air," *Advanced Energy Materials*, vol. 1, no. 1. pp. 34–50, 01-Jan-2011, doi: 10.1002/aenm.201000010.

[63] T. Khoo, P. C. Howlett, M. Tsagouria, D. R. MacFarlane, and M. Forsyth, "The potential for ionic liquid electrolytes to stabilise the magnesium interface for magnesium/air batteries," *Electrochim. Acta*, vol. 58, no. 1, pp. 583–588, Dec. 2011, doi: 10.1016/j.electacta.2011.10.006.

[64] J. Park, G. Nam, and J. Cho, "Perspective of Zn-Air Batteries," 2015. [Online]. Available: https://www.csm.ornl.gov/BLI8/presentations/J. CHO-UNIST-BYI8.pdf.

[65] J. F. Parker, C. N. Chervin, E. S. Nelson, D. R. Rolison, and J. W. Long, "Wiring zinc in three dimensions re-writes battery performance—dendrite-free cycling," *Energy Environ. Sci.*, vol. 7, no. 3, pp. 1117–1124, 2014, doi: 10.1039/C3EE43754J.

[66] S. M. Lee, Y. J. Kim, S. W. Eom, N. S. Choi, K. W. Kim, and S. B. Cho, "Improvement in self-discharge of Zn anode by applying surface modification for Zn-air batteries with high energy density," *J. Power Sources*, vol. 227, pp. 177–184, 2013, doi: 10.1016/j.jpowsour.2012.11.046.

[67] T. Keily and T. J. Sinclair, "Effect of additives on the corrosion of zinc in koh solution," *J. Power Sources*, vol. 6, no. 1, pp. 47–62, 1981, doi: https://doi.org/10.1016/0378-7753(81)80005-5.

[68] K. Wang, P. Pei, Z. Ma, H. Xu, P. Li, and X. Wang, "Morphology control of zinc regeneration for zinc-air fuel cell and battery," *J. Power Sources*, vol.

271, pp. 65–75, 2014, doi: 10.1016/j.jpowsour.2014.07.182.

[69] J. Lee, B. Hwang, M. S. Park, and K. Kim, “Improved reversibility of Zn anodes for rechargeable Zn-air batteries by using alkoxide and acetate ions,” *Electrochim. Acta*, vol. 199, pp. 164–171, 2016, doi: 10.1016/j.electacta.2016.03.148.

[70] B. B. Blizanac, P. N. Ross, and N. M. Markovic, “Oxygen electroreduction on Ag(1 1 1): The pH effect,” *Electrochim. Acta*, vol. 52, no. 6, pp. 2264–2271, 2007, doi: 10.1016/j.electacta.2006.06.047.

[71] V. Caramia and B. Bozzini, “Materials science aspects of zinc-air batteries: A review,” *Mater. Renew. Sustain. Energy*, vol. 3, no. 2, 2014, doi: 10.1007/s40243-014-0028-3.

[72] J. Drillet, F. Holzer, T. Kallis, and S. Mu, “Influence of CO2 on the stability of bifunctional oxygen electrodes for rechargeable zinc / air batteries and study of different CO2 filter materials,” pp. 8–11, 2001.

[73] R. Othman, W. J. Basirun, A. H. Yahaya, and A. K. Arof, “Hydroponics gel as a new electrolyte gelling agent for alkaline zinc–air cells,” vol. 103, pp. 34–41, 2001.

[74] J. Park, M. Park, G. Nam, J. S. Lee, and J. Cho, “All-solid-state cable-type flexible zinc-air battery,” *Adv. Mater.*, vol. 27, no. 8, pp. 1396–1401, 2015, doi: 10.1002/adma.201404639.

[75] V. Neburchilov, H. Wang, J. J. Martin, and W. Qu, “A review on air cathodes for zinc-air fuel cells,” *Journal of Power Sources*, vol. 195, no. 5. pp. 1271–1291, 01-Mar-2010, doi: 10.1016/j.jpowsour.2009.08.100.

[76] D. U. Lee, J. Y. Choi, K. Feng, H. W. Park, and Z. Chen, “Advanced extremely durable 3D bifunctional air electrodes for rechargeable zinc-air batteries,” *Adv. Energy Mater.*, vol. 4, no. 6, p. 1301389, Apr. 2014, doi: 10.1002/aenm.201301389.

[77] G. Toussaint, P. Stevens, L. Akrour, R. Rouget, and F. Fourgeot, “Development of a Rechargeable Zinc-Air Battery,” *ECS Trans.*, vol. 28, no. 32, pp. 25–34, 2019, doi: 10.1149/1.3507924.

[78] L. Feng, X. Sun, S. Yao, C. Liu, W. Xing, and J. Zhang, *Electrocatalysts and Catalyst Layers for Oxygen Reduction Reaction*. Elsevier B.V., 2014.

[79] P. A. Christensen, A. Hamnett, and D. Linares-Moya, “Oxygen reduction and fuel oxidation in alkaline solution,” *Phys. Chem. Chem. Phys.*, vol. 13, no. 12, pp. 5206–5214, 2011, doi: 10.1039/C0CP02365E.

[80] N. Ramaswamy and S. Mukerjee, “Fundamental mechanistic understanding of electrocatalysis of oxygen reduction on Pt and non-Pt surfaces: Acid versus alkaline media,” *Adv. Phys. Chem.*, vol. 2012, 2012, doi: 10.1155/2012/491604.

[81] J. Suntivich, H. A. Gasteiger, N. Yabuuchi, H. Nakanishi, J. B. Goodenough, and Y. Shao-Horn, “Design principles for oxygen-reduction activity on perovskite oxide catalysts for fuel cells and metal-air batteries,” *Nat. Chem.*, vol. 3, no. 7, pp. 546–550, 2011, doi: 10.1038/nchem.1069.

[82] C. Hu, L. Zhang, and J. Gong, “Recent progress made in the mechanism comprehension and design of electrocatalysts for alkaline water splitting,” *Energy Environ. Sci.*, vol. 12, no. 9, pp. 2620–2645, 2019, doi: 10.1039/c9ee01202h.

[83] Z. L. Wang, D. Xu, J. J. Xu, and X. B. Zhang, “Oxygen electrocatalysts in metal-air batteries: From aqueous to nonaqueous electrolytes,” *Chem. Soc. Rev.*, vol. 43, no. 22, pp. 7746–7786, 2014, doi: 10.1039/c3cs60248f.

[84] J. K. Nørskov *et al.*, “Origin of the overpotential for oxygen reduction at a fuel-cell cathode,” *J. Phys. Chem. B*, vol. 108, no. 46, pp. 17886–17892, 2004, doi: 10.1021/jp047349j.

[85] W. Chu, D. Higgins, Z. Chen, and R. Cai, “Non-precious Metal Oxides and

Metal Carbides for ORR in Alkaline-Based Fuel Cells," *Non-Noble Met. Fuel Cell Catal.*, vol. 9783527333, pp. 357–388, 2014, doi: 10.1002/9783527664900.ch10.

[86] S. Devaraj and N. Munichandraiah, "Effect of crystallographic structure of MnO2 on its electrochemical capacitance properties," *J. Phys. Chem. C*, vol. 112, no. 11, pp. 4406–4417, 2008, doi: 10.1021/jp7108785.

[87] Z. Du *et al.*, "A low temperature hydrothermal synthesis of delafossite CuCoO2 as an efficient electrocatalyst for the oxygen evolution reaction in alkaline solutions," *Inorg. Chem. Front.*, vol. 5, no. 1, pp. 183–188, Jan. 2018, doi: 10.1039/c7qi00621g.

[88] İ. C. Kaya, M. A. Sevindik, and H. Akyıldız, "Characteristics of Fe- and Mg-doped CuCrO2 nanocrystals prepared by hydrothermal synthesis," *J. Mater. Sci. Mater. Electron.*, vol. 27, no. 3, pp. 2404–2411, 2016, doi: 10.1007/s10854-015-4038-4.

[89] A. Çetin, "Synthesis of First Row Transition Metal Oxide Nanomaterials," Middle East Technical University, 2020.

[90] M. Zhou, C. Yang, and K. Y. Chan, "Structuring porous iron-nitrogen-doped carbon in a core/shell geometry for the oxygen reduction reaction," *Adv. Energy Mater.*, vol. 4, no. 18, pp. 1–5, 2014, doi: 10.1002/aenm.201400840.

[91] G. F. Li, D. Yang, and P. Y. Abel Chuang, "Defining Nafion Ionomer Roles for Enhancing Alkaline Oxygen Evolution Electrocatalysis," *ACS Catal.*, vol. 8, no. 12, pp. 11688–11698, 2018, doi: 10.1021/acscatal.8b02217.

[92] G. Li, L. Anderson, Y. Chen, M. Pan, and P. Y. Abel Chuang, "New insights into evaluating catalyst activity and stability for oxygen evolution reactions in alkaline media," *Sustain. Energy Fuels*, vol. 2, no. 1, pp. 237–251, 2018, doi: 10.1039/c7se00337d.

[93] C. Wei *et al.*, "Recommended Practices and Benchmark Activity for

Hydrogen and Oxygen Electrocatalysis in Water Splitting and Fuel Cells," *Adv. Mater.*, vol. 31, no. 31, pp. 1–24, 2019, doi: 10.1002/adma.201806296.

[94] H. Li *et al.*, "Two-in-one solution using insect wings to produce graphene-graphite films for efficient electrocatalysis," *Nano Res.*, vol. 12, no. 1, pp. 33–39, 2019, doi: 10.1007/s12274-018-2172-z.

[95] H. E. Wang, Z. Lu, D. Qian, S. Fang, and J. Zhang, "Facile synthesis and electrochemical characterization of hierarchical α-MnO2 spheres," *J. Alloys Compd.*, vol. 466, no. 1–2, pp. 250–257, 2008, doi: 10.1016/j.jallcom.2007.11.041.

[96] C. Li, Z. Yu, H. Liu, and K. Chen, "High surface area LaMnO3 nanoparticles enhancing electrochemical catalytic activity for rechargeable lithium-air batteries," *J. Phys. Chem. Solids*, vol. 113, no. August 2017, pp. 151–156, 2018, doi: 10.1016/j.jpcs.2017.10.039.

[97] L. Lutterotti, S. Matthies, and H. R. Wenk, "MAUD: a friendly Java program for Material Analysis Using Diffraction," *Int. Union Crystallogr. Newsl.*, no. 21, pp. 14–15, 1999.

[98] Y. Meng, W. Song, H. Huang, Z. Ren, S. Y. Chen, and S. L. Suib, "Structure-property relationship of bifunctional MnO2 nanostructures: Highly efficient, ultra-stable electrochemical water oxidation and oxygen reduction reaction catalysts identified in alkaline media," *J. Am. Chem. Soc.*, vol. 136, no. 32, pp. 11452–11464, 2014, doi: 10.1021/ja505186m.

[99] R. P. Putra, H. Horino, and I. I. Rzeznicka, "An Efficient Electrocatalyst for Oxygen Evolution Reaction in Alkaline Solutions Derived from a Copper Chelate Polymer via In Situ Electrochemical Transformation," 2020.

[100] L. T. Tseng *et al.*, "Magnetic properties in α-MnO2 doped with alkaline elements," *Sci. Rep.*, vol. 5, pp. 1–8, 2015, doi: 10.1038/srep09094.

[101] M. A. San-Miguel *et al.*, "In situ growth of Ag nanoparticles on α-Ag 2 WO

4 under electron irradiation: Probing the physical principles," *Nanotechnology*, vol. 27, no. 22, p. 225703, Jun. 2016, doi: 10.1088/0957-4484/27/22/225703.

[102] O. Antoine, Y. Bultel, and R. Durand, "Oxygen reduction reaction kinetics and mechanism on platinum nanoparticles inside Nafion®," *J. Electroanal. Chem.*, vol. 499, no. 1, pp. 85–94, 2001, doi: 10.1016/S0022-0728(00)00492-7.

[103] S. M. Alshehri *et al.*, "Synthesis, characterization, multifunctional electrochemical (OGR/ORR/SCs) and photodegradable activities of ZnWO4 nanobricks," *J. Sol-Gel Sci. Technol.*, vol. 87, no. 1, pp. 137–146, 2018, doi: 10.1007/s10971-018-4698-7.

[104] M. Mohamed Jaffer Sadiq, S. Mutyala, J. Mathiyarasu, and D. Krishna Bhat, "RGO/ZnWO4/Fe3O4 nanocomposite as an efficient electrocatalyst for oxygen reduction reaction," *J. Electroanal. Chem.*, vol. 799, no. January, pp. 102–110, 2017, doi: 10.1016/j.jelechem.2017.05.051.

[105] S. M. Alshehri, J. Ahmed, T. Ahamad, P. Arunachalam, T. Ahmad, and A. Khan, "Bifunctional electro-catalytic performances of CoWO4 nanocubes for water redox reactions (OER/ORR)," *RSC Adv.*, vol. 7, no. 72, pp. 45615–45623, 2017, doi: 10.1039/c7ra07256b.

[106] B. Jansi Rani *et al.*, "Bi 2 WO 6 and FeWO 4 Nanocatalysts for the Electrochemical Water Oxidation Process," *ACS Omega*, vol. 4, no. 3, pp. 5241–5253, 2019, doi: 10.1021/acsomega.8b03003.

[107] E. Fabbri, A. Habereder, K. Waltar, R. Kötz, and T. J. Schmidt, "Developments and perspectives of oxide-based catalysts for the oxygen evolution reaction," *Catalysis Science and Technology*, vol. 4, no. 11. The Royal Society of Chemistry, pp. 3800–3821, 06-Oct-2014, doi: 10.1039/c4cy00669k.

[108] Q. Wu, L. Jiang, Q. Tang, J. Liu, S. Wang, and G. Sun, "Activity and stability

of the Ni(OH) 2 MnO x /C composite for oxygen reduction reaction in alkaline solution," *Electrochim. Acta*, vol. 91, pp. 314–322, Feb. 2013, doi: 10.1016/j.electacta.2012.12.076.

[109] L.-A. Stern and X. Hu, "Enhanced oxygen evolution activity by NiO x and Ni(OH) 2 nanoparticles," *Faraday Discuss.*, vol. 176, no. 0, pp. 363–379, Mar. 2014, doi: 10.1039/C4FD00120F.

[110] A. Eftekhari, "Tuning the electrocatalysts for oxygen evolution reaction," *Mater. Today Energy*, vol. 5, pp. 37–57, Sep. 2017, doi: 10.1016/j.mtener.2017.05.002.

[111] C. Alegre *et al.*, "A combination of CoO and Co nanoparticles supported on electrospun carbon nanofibers as highly stable air electrodes," *J. Power Sources*, vol. 364, pp. 101–109, Oct. 2017, doi: 10.1016/j.jpowsour.2017.08.007.

[112] G. Karkera, T. Sarkar, M. D. Bharadwaj, and A. S. Prakash, "Design and Development of Efficient Bifunctional Catalysts by Tuning the Electronic Properties of Cobalt–Manganese Tungstate for Oxygen Reduction and Evolution Reactions," *ChemCatChem*, vol. 9, no. 19, pp. 3681–3690, 2017, doi: 10.1002/cctc.201700540.

[113] A. Habekost, "Experimental Investigations of Alkaline Silver-zinc and Copper-zinc Batteries," *World J. Chem. Educ. Vol. 4, 2016, Pages 4-12*, vol. 4, no. 1, pp. 4–12, Jan. 2016, doi: 10.3354/dao068065.

[114] S. Grushevskaya, D. Kudryashov, and A. Vvedenskii, "Anodic Formation of Ag(I) Oxide on Ag-Au Alloys," *Croat. Chem. Acta*, vol. 81, no. 3, pp. 467–475, Nov. 2008.

[115] N. Sato and Y. Shimizu, "Anodic oxide on silver in alkaline solution," *Electrochim. Acta*, vol. 18, no. 8, pp. 567–570, Aug. 1973, doi: 10.1016/0013-4686(73)85020-0.

[116] A. Ashok, A. Kumar, M. A. Matin, and F. Tarlochan, “Synthesis of Highly Efficient Bifunctional Ag/Co 3 O 4 Catalyst for Oxygen Reduction and Oxygen Evolution Reactions in Alkaline Medium,” *ACS Omega*, vol. 3, no. 7, pp. 7745–7756, Jul. 2018, doi: 10.1021/acsomega.8b00799.

[117] J. Guo, A. Hsu, D. Chu, and R. Chen, “Improving oxygen reduction reaction activities on carbon-supported Ag nanoparticles in alkaline solutions,” *J. Phys. Chem. C*, vol. 114, no. 10, pp. 4324–4330, 2010, doi: 10.1021/jp910790u.

[118] A. Sreedevi, K. P. Priyanka, K. K. Babitha, S. I. Sankararaman, and V. Thomas, “Synthesis and characterization of silver tungstate/iron phthalocyanine nanocomposite for electronic applications,” *Eur. Phys. J. B*, vol. 90, no. 6, pp. 1–10, 2017, doi: 10.1140/epjb/e2017-80149-9.

[119] N. G. Macedo *et al.*, “Surfactant-Mediated Morphology and Photocatalytic Activity of α-Ag2WO4 Material,” *J. Phys. Chem. C*, vol. 122, no. 15, pp. 8667–8679, 2018, doi: 10.1021/acs.jpcc.8b01898.

[120] V. Brunetti, H. Villullas, and M. López Teijelo, “Kinetics of the electroreduction of Ag2CrO4 salt films electrodeposited on silver,” *An. des la Asoc. Quim. Argentina*, vol. 91, pp. 97–106, 2003.

[121] D. Xiong *et al.*, “Polyvinylpyrrolidone-Assisted Hydrothermal Synthesis of CuCoO2 Nanoplates with Enhanced Oxygen Evolution Reaction Performance,” *ACS Sustain. Chem. Eng.*, vol. 7, no. 1, pp. 1493–1501, 2019, doi: 10.1021/acssuschemeng.8b05236.

[122] J. Zhang, Z. Xia, and L. Dai, “Carbon-based electrocatalysts for advanced energy conversion and storage,” *Sci. Adv.*, vol. 1, no. 7, 2015, doi: 10.1126/sciadv.1500564.

[123] W. Sheng, Z. Zhuang, M. Gao, J. Zheng, J. G. Chen, and Y. Yan, “Correlating hydrogen oxidation and evolution activity on platinum at different pH with measured hydrogen binding energy,” *Nat. Commun.*, vol. 6, pp. 6–11, 2015,

doi: 10.1038/ncomms6848.

[124] N. Mahmood, Y. Yao, J. W. Zhang, L. Pan, X. Zhang, and J. J. Zou, “Electrocatalysts for Hydrogen Evolution in Alkaline Electrolytes: Mechanisms, Challenges, and Prospective Solutions,” *Adv. Sci.*, vol. 5, no. 2, 2018, doi: 10.1002/advs.201700464.

[125] L. Xie and D. W. Kirk, “Stability Comparison of Pt and Ni as Base Metal Catalysts in Anion Exchange Membrane Fuel Cells,” *J. Electrochem. Soc.*, vol. 167, no. 6, p. 064519, 2020, doi: 10.1149/1945-7111/ab8368.

[126] K. Toyoda, R. Hinogami, N. Miyata, and M. Aizawa, “Calculated descriptors of catalytic activity for water electrolysis anode: Application to delafossite oxides,” *J. Phys. Chem. C*, vol. 119, no. 12, pp. 6495–6501, 2015, doi: 10.1021/jp5092398.

[127] L. Mao, S. Mohan, and Y. Mao, “Delafossite CuMnO2 as an efficient bifunctional oxygen and hydrogen evolution reaction electrocatalyst for water splitting,” *J. Electrochem. Soc.*, vol. 166, no. 6, pp. H233–H242, 2019, doi: 10.1149/2.1181906jes.

[128] S. P. Prakash, “Copper delafossite-based anodes for electrochemical (sea) water splitting.”

[129] J. Ahmed and Y. Mao, “Synthesis, characterization and electrocatalytic properties of delafossite CuGaO2,” *J. Solid State Chem.*, vol. 242, pp. 77–85, 2016, doi: 10.1016/j.jssc.2016.07.006.

[130] M. Chauhan, K. P. Reddy, C. S. Gopinath, and S. Deka, “Copper Cobalt Sulfide Nanosheets Realizing a Promising Electrocatalytic Oxygen Evolution Reaction,” *ACS Catal.*, vol. 7, no. 9, pp. 5871–5879, 2017, doi: 10.1021/acscatal.7b01831.

[131] K. Lankauf *et al.*, “MnxCo3-xO4 spinel oxides as efficient oxygen evolution reaction catalysts in alkaline media,” *Int. J. Hydrogen Energy*, vol. 5, 2020,

doi: 10.1016/j.ijhydene.2020.03.188.

[132] M. Gao *et al.*, “Efficient water oxidation using nanostructured α-nickel-hydroxide as an electrocatalyst,” *J. Am. Chem. Soc.*, vol. 136, no. 19, pp. 7077–7084, 2014, doi: 10.1021/ja502128j.

[133] R. L. Doyle and M. E. G. Lyons, “An electrochemical impedance study of the oxygen evolution reaction at hydrous iron oxide in base,” *Phys. Chem. Chem. Phys.*, vol. 15, no. 14, pp. 5224–5237, 2013, doi: 10.1039/c3cp43464h.

[134] F. Claudel *et al.*, “Degradation Mechanisms of Oxygen Evolution Reaction Electrocatalysts: A Combined Identical-Location Transmission Electron Microscopy and X-ray Photoelectron Spectroscopy Study,” *ACS Catal.*, vol. 9, no. 5, pp. 4688–4698, 2019, doi: 10.1021/acscatal.9b00280.

[135] R. M. Arán-Ais *et al.*, “Identical Location Transmission Electron Microscopy Imaging of Site-Selective Pt Nanocatalysts: Electrochemical Activation and Surface Disordering,” *J. Am. Chem. Soc.*, vol. 137, no. 47, pp. 14992–14998, Dec. 2015, doi: 10.1021/jacs.5b09553.

[136] R. Jiang, D. T. Tran, J. Li, and D. Chu, “ Ru@RuO 2 Core-Shell Nanorods: A Highly Active and Stable Bifunctional Catalyst for Oxygen Evolution and Hydrogen Evolution Reactions ,” *Energy Environ. Mater.*, vol. 2, no. 3, pp. 201–208, 2019, doi: 10.1002/eem2.12031.

[137] S. Jung, C. C. L. McCrory, I. M. Ferrer, J. C. Peters, and T. F. Jaramillo, “Benchmarking nanoparticulate metal oxide electrocatalysts for the alkaline water oxidation reaction,” *J. Mater. Chem. A*, vol. 4, no. 8, pp. 3068–3076, 2016, doi: 10.1039/c5ta07586f.

[138] R. Majee, Q. A. Islam, and S. Bhattacharyya, “Surface Charge Modulation of Perovskite Oxides at the Crystalline Junction with Layered Double Hydroxide for a Durable Rechargeable Zinc-Air Battery,” *ACS Appl. Mater. Interfaces*, vol. 11, no. 39, pp. 35853–35862, 2019, doi: 10.1021/acsami.9b09299.

CURRICULUM VITAE

PERSONAL INFORMATION

Surname, Name: Arslan Hamat, Burcu
Nationality: Turkish (TC)
Date and Place of Birth: 18 November 1988, Ankara
Marital Status: Married
Phone: +90 312 210 58 31
email: e155913@metu.edu.tr

EDUCATION

Degree	Institution	Year of Graduation
MS	METU Metallurgical and Material Engineering	2014
BS	METU Metallurgical and Material Engineering	2011
High School	Mehmet Emin Resulzade Anadolu High School, Ankara	2006

WORK EXPERIENCE

Year	Place	Enrollment
2017-Present	Turkish Aerospace Industries Inc.	R&D Engineer
2012-2017	METU Dept. of Metallurgical and Material Eng.	Research Assistant
2010 July	Turkish Aerospace Industries Inc.	Intern Eng. Student
2009 July	Ereğli Demir Çelik Fabrikası	Intern Eng. Student

FOREIGN LANGUAGES

Advanced English

PUBLICATIONS

1. Arslan Hamat, B. Aydınol, M. K. "Experimental investigation on the electrocatalytic behavior of Ag-based oxides, Ag_2XO_4 (X= Cr, Mo, W), for the oxygen reduction reaction in alkaline media", Journal of Solid State Chemistry, 290, 121571 (2020).